JYU DISSERTATIONS 766

Johanna Alaranta

Synthesis of Monomethine Cyanine Dyes and Gold Nanoclusters and their Applications as Fluorescent Probes

UNIVERSITY OF JYVÄSKYLÄ
FACULTY OF MATHEMATICS
AND SCIENCE

JYU DISSERTATIONS 766

Johanna Alaranta

Synthesis of Monomethine Cyanine Dyes and Gold Nanoclusters and their Applications as Fluorescent Probes

Esitetään Jyväskylän yliopiston matemaattis-luonnontieteellisen tiedekunnan suostumuksella
julkisesti tarkastettavaksi Ylistönrinteen auditoriossa Kem4
huhtikuun 19. päivänä 2024 kello 12.

Academic dissertation to be publicly discussed, by permission of
the Faculty of Mathematics and Science of the University of Jyväskylä,
in Ylistönrinne, auditorium Kem4, on April 19, 2024, at 12 o'clock.

JYVÄSKYLÄN YLIOPISTO
UNIVERSITY OF JYVÄSKYLÄ

JYVÄSKYLÄ 2024

Editors
Tanja Lahtinen
Department of Chemistry, University of Jyväskylä
Päivi Vuorio
Open Science Centre, University of Jyväskylä

ISBN 978-952-86-0101-2 (PDF)
URN:ISBN:978-952-86-0101-2
ISSN 2489-9003

Permanent link to this publication: http://urn.fi/URN:ISBN:978-952-86-0101-2

ABSTRACT

Alaranta, Johanna
Synthesis of monomethine cyanine dyes and gold nanoclusters and their applications as fluorescent probes.
Jyväskylä: University of Jyväskylä, 2024, 67 p. + original pages
(JYU Dissertations
ISSN 2489-9003; 766)
ISBN 978-952-86-0101-2 (PDF)

This thesis focuses on monomethine cyanine dyes, their synthesis and applications as fluorescent probes in nucleic acid detection. Gold nanoclusters and fluorescent probe complexes were also discussed as a possible interface of the two materials. The literature review of cyanine dyes focused on the synthetic aspects of the dyes and how it has been developed throughout the years. The interaction with nucleic acids is discussed along with the different applications it allows. Some examples of applications without nucleic acids are also included. In the experimental part, novel monomethine cyanine dyes were synthesized with a series of structural modifications aimed to improve the photophysical qualities, such as the brightness of the dyes. The characterization of the dyes was an important task to ensure the product was correct and pure for the absorption and fluorescence measurements. Mass spectrometry had a crucial role in ensuring the purity of the ionic products, as it made the first assessment of the product structure possible with only a glimpse. NMR was used to confirm the assumptions made with mass data. However, neither of these methods give information about the absolute structure and packing of the molecules in a solid state; hence, X-ray diffraction was used to obtain the single crystal structures for selected dyes. The single crystal structures also made molecular modeling possible to better understand the interactions between the studied dyes and DNA.

Gold nanoclusters were a smaller, yet important part of the thesis since new information about synthesizing gold nanocluster and fluorescent probe complexes and their behavior was gained, providing important knowledge for future applications. The literature review of gold nanoclusters focused on their synthesis and applications with fluorescent probes. Since the complex of these materials is still quite new, only a few examples of studies by other groups were found. In the experimental part, the synthesis of one gold nanocluster is discussed and the pH dependent fluorescence of the cluster-probe complex in a solution. These results are promising as the complex of cyanine dye and gold nanocluster has been discussed as a completely new type of tool to be used in biological applications.

Keywords: cyanine dye, nucleic acid, photophysics, gold nanocluster, fluorescence.

TIIVISTELMÄ (ABSTRACT IN FINNISH)

Alaranta, Johanna
Monometeeni syaniiniväriaineiden ja kultananoklustereiden synteesi ja käyttö fluoresoivina koettimina.
Jyväskylä: Jyväskylän yliopisto, 2024, 67 s. + alkuperäiset artikkelit
(JYU Dissertations
ISSN 2489-9003; 766)
ISBN 978-952-86-0101-2 (PDF)

Tämä opinnäytetyö keskittyy monometeeni syaniiniväriaineisiin, niiden synteesiin ja käyttöön fluoresoivina koettimina nukleiinihappojen kuvantamisessa. Kultananoklustereiden ja fluoresoivien koettimien komplekseja käsiteltiin myös mahdollisena rajapintana näiden kahden materiaalin välillä. Syaniiniväriaineiden kirjallisuuskatsaus keskittyi väriaineiden synteesin ja siihen, miten sitä on kehitetty vuosien varrella. Työssä käydään myös läpi värien ja nukeleiinihappojen vuorovaikutusta ja mitä sovelluksia se mahdollistaa. Lisäksi esitellään esimerkkejä käyttökohteista ilman nukleiinihappoja. Kokeellisessa osassa syntetisoitiin uusia monometeeni syaniiniväriaineita erilaisilla rakenteellisilla muutoksilla, joiden tavoitteena oli parantaa väriaineiden fotofysikaalisia ominaisuuksia, kuten kirkkautta. Syntetisoitujen väriaineiden karakterisointi oli erittäin tärkeässä roolissa koko työn läpi, koska sen avulla paitsi varmistettiin tuotteen olevan se, mitä tavoiteltiin, sekä se, että saatu väriaine oli puhdasta absorptio ja fluoresenssi mittauksiin. Etenkin massaspektrometrialla oli tärkeä rooli ionisten tuotteiden puhtauden varmistamisessa, ja se mahdollisti arvion synteesin onnistumisesta ja tuotteen puhtaudesta heti mittauksen yhteydessä. NMR:ää käytettiin vahvistamaan massaspektrometrimittausten perusteella tehty ensiarvio. Nämä edellä mainitut menetelmät eivät kuitenkaan anna tietoa molekyylin tarkasta rakenteesta ja pakkautumisesta. Siksi kiinteässä tilassa mitattavat röntgendiffraktio yksittäiskiteiden rakenteet antavat tärkeää tietoa tuotteen rakenteesta, mitä muilla menetelmillä ei voida saada. Kiderakenteet mahdollistivat myös molekyylimallinnuksen, minkä avulla voitiin entistä paremmin ymmärtää tutkittujen väriaineiden ja DNA:n välisiä vuorovaikutuksia.

Kultananoklusterit olivat työssä pienempi osa, mutta sen avulla saatiin tärkeää tietoa kultananklustereiden ja fluoresoivan väriaineen kompleksin syntetisoimisesta ja käytöstä, ja kirjallisuuskatsaus keskittyi niiden synteesiin ja sovelluksiin fluoresoivien koettimien kanssa. Koska näiden kahden edellä mainitun materiaalin kompleksi on vielä melko uusi innovaatio, esimerkkejä muiden tutkijoiden tekemistä tutkimuksista löytyi vain muutama. Kokeellisessa osassa esitellään yhden kultananoklusterin synteesi ja käydään läpi tämän kultananoklusterin ja fluoresoivan koettimien muodostaman kompleksin kykyä mitata liuoksen pH:ta. Saadut tulokset olivat varsin lupaavia, koska syaniiniväriaineen ja kultananoklusterin muodostaman kompleksin käyttäminen biologisissa sovelluksissa voisi olla täysin uudenlainen työkalu tulevaisuudessa.

Avainsanat: syaniiniväriaine, nukleiinihappo, fotofysiikka, kultananoklusteri, fluoresenssi.

Author

Johanna Alaranta
Department of Chemistry
Nanoscience Center
University of Jyväskylä
P.O Box 35
FI-40014 Jyväskylä
johanna.m.alaranta@jyu.fi

Supervisors

Docent Tanja Lahtinen
Department of Chemistry
Nanoscience Center
University of Jyväskylä
P.O Box 35
FI-40014 Jyväskylä

Professor Hannu Häkkinen
Departments of Chemistry and Physics
Nanoscience Center
University of Jyväskylä
P.O Box 35
FI-40014 Jyväskylä

Reviewers

Professor Marcus Wilhelmsson
Department of Chemistry and Biochemistry
Chalmers University of Technology
Sweden

Assistant Professor Peter Šebej
Faculty of Science
Masaryk University
Czech Republic

Opponent

Associate Professor Nonappa
Faculty of Engineering and Natural Sciences
Tampere University
Finland

PREFACE

It has been almost a decade since the first time I crossed the bridge and climbed the stairs to Ylistö and the department of chemistry. The place I first thought was just going to be an intermediate station on my way to medical school. Little did I know how much stronger my love for chemistry grew from the day one. Inspiring professors, hands-on work in the labs and burning desire to understand more thrived me on. When it was time to apply to medical school again, I noticed I was more into studying for my exams or finishing the demo exercises on my course work than practicing for the entrance exam. So, I decided to stay, which I think turned out to be the best decision of my life so far.

During my time here at the University of Jyväskylä, I have had the pleasure to meet and learn from amazing people, even across departmental boundaries at the Nanoscience center. Safe to say the greatest gratitude goes to my supervisor senior lecturer Tanja Lahtinen, who has been part of my journey since I started my bachelor's degree. Tanja has always made me feel I am the top priority and made sure I could focus on doing my thing while she worked on the background, making sure everything goes smoothly. She provided me all the tools needed to be successful but also let me learn myself how they work. I don't think words can explain how grateful I am that she saw something in me and was willing to guide me through my years in University of Jyväskylä to this day. I would also like to thank professor Hannu Häkkinen for being my second supervisor, and always being interested in hearing how my projects are going on and giving me the opportunity to work with his talented research group.

Through our collaborations I have had the privilege to work with so many talented people, professors Varpu Marjomäki, Kari Rissanen and Hannu Häkkinen and their group members, Sailee, Kati, Khai, Arto, Fransisca, Kyunglim and Sami, thank you all for the valuable knowledge I got to learn from each of you. Of course, I have to thank Dr. Ville Saarnio, who taught me everything he knows about cyanine dyes and gave me a head start on my journey with them. I am incredibly grateful for the people I have had privilege to meet and get to know while working at the Nanoscience center. Our Nanochemistry team has felt like a home to me during my time here. Henna, Elsa, Małgorzata, Efstratios, Romain, Johanna S., and others thank you for the inspiring seminars and for the joy you brought to the lab and the corridors of Nanoscience center. A special thanks goes to Tatu and Amar, who had the strongest nerves trying to teach an organic chemist the complicated world of spectroscopy. Thank you, Anniina and Elina K., for teaching me how to understand and operate the state-of-the-art mass spectrometer.

I would also like to thank professor Marcus Wilhelmsson and assistant professor Peter Šebej for reviewing my thesis and giving me valuable comments to improve my writing and of course associate professor Nonappa who kindly agreed to act as my opponent.

Lastly, I want to thank my loved ones, who had shown me unconditional love and support throughout my life. Marjo, Pauli, Joonas ja Mirja thank you for always being my number one fans, even if my study subjects may have bored you, I always felt you listened to me and were proud of my accomplishments. And of course, the rest of my amazing family, my godmothers and everyone else, I love you all dearly. I have the greatest privilege to have so many supportive people in my life and I also want to thank you who joined my journey more recently, Toivo, Nea, Marko, Tiina, Mirjam and Martti, I adore you and I am very grateful how open-mindedly you have taken me in. You have made me feel home with you from the day one. Lastly my greatest gratitude goes to my fiancé, Mikael, who has been the rock for me throughout my journey in science and all our adventures in life. You have always believed in me and my skills, never doubting me even if I was. Thank you for always listening and assuring me everything is going to work out. I would not be here without you. I can't wait to start this next chapter in our lives and explore the world with you and our little rainbow. Thank you for being you.

Dear reader, I hope you have inspiring time with my thesis.

Jyväskylä 12.3.2024
Johanna Alaranta

LIST OF INCLUDED PUBLICATIONS

I Saarnio, V. K.; Alaranta, J. M. and Lahtinen, T. M., Systematic study of SYBR green chromophore reveals major improvement with one heteroatom difference, *Journal of Materials Chemistry B*, **2021**, 9, 3484–3488.

II Alaranta J. M.; Truong, K-N.; Matus, M. F.; Malola, S. A.; Rissanen, K. T.; Shroff, S. S.; Marjomäki, V. S.; Häkkinen, H. J. and Lahtinen, T. M., Optimizing the SYBR Green Related Cyanine Dye Structure to Aim for Brighter Nucleic Acid Visualization, *Dyes and Pigments*, **2022**, 208, 110844.

III Pyo, K.; Matus, M. F.; Malola, S.; Hulkko, E.; Alaranta, J.; Lahtinen, T.; Häkkinen, H.; Pettersson, M., Tailoring the interaction between a gold nanocluster and a fluorescent dye by cluster size: creating a toolbox of range-adjustable pH sensors, *Nanoscale Advances*, **2022**, 4, 4579-4588.

IV Alaranta, J.; Valkonen, A.; Rissanen, K. ja Lahtinen, T., Modifying the terminal phenyl group of monomethine cyanine dyes as a pathway to brighter nucleic acid probes, *New Journal of Chemistry*, **2024**, 48, 4931-4935.

Author's contribution

The author was responsible for the synthesis and characterization of the new cyanine dyes in articles **I** and **II** and **IV**. Additionally, in article **II** and **IV** she had major contribution to the design of the dyes and conducted the photophysical studies of the dyes with nucleic acids. In article **III** author was responsible for the synthesis of the Au_{102}(*p*-MBA)$_{44}$ cluster and its purification.

ABBREVIATIONS

AuNC	Gold nanocluster
AuNP	Gold nanoparticle
BSA	Bovine serum albumin
DCM	Dichloromethane
DIPEA	*N,N*-Diisopropylethylamine
DMSO	Dimethylsulfoxide
DNA	Deoxyribonucleic acid
FRET	Förster resonance energy transfer
HOMO	Highest occupied molecular orbital
LUMO	Lowest unoccupied molecular orbital
PAGE	Polyacrylamide gel electrophoresis
PDT	Photodynamic therapy
p-MBA	Para-mercaptobenzoic acid
PTT	Photothermal therapy
QY	Quantum yield
RNA	Ribonucleic acid
ROS	Reactive oxygen species
TO	Thiazole orange
YO	Oxazole yellow

CONTENTS

1 INTRODUCTION

Throughout human history, people have been fascinated by colors. Since the stone age, many methods have been used to extract colors from nature, such as minerals, plants, and insects, to be used in art and day-to-day life, for example, as paints and textile colors. Since the discovery of synthetic colorants in the 1700s, the production of synthetic dyes and pigments have bloomed drastically.[1] Colorants, dyes, and pigments are more common than one might think when they first hear the name. Dyes and pigments are molecules bearing colors, meaning that they can absorb light at a visible range. Dyes are soluble in water or organic solvents, making them distinctly different from pigments, which are insoluble in the media they are used. Dyes are able to bind with materials, and in most cases, they have an affinity to specific materials, such as nucleic acids. While pigments do not have the same affinity towards the material, they have strong interactions within themselves, preventing the solvation. Pigments are common in paints and cosmetics, while dyes are more common in the textile and food industry.[2] Cyanine dyes are a class of organic dyes with various applications, ranging from the textile and photographic industries to optical recording media to anti-cancer agents and fluorescent probes for a range of biological targets, such as DNA and RNA.[3]

Gold has a long history, as it has been used as decorations, jewelry, idols, and money for over 6,000 years. The beauty of this rare metal has intrigued people and even caused some violence.[4] Beyond its beauty, gold has unique properties as a metal; it is easy to shape, it does not easily react with most metals or chemicals,[5] and it has also been used as medicine.[6] Unsurprisingly, gold has been vigorously studied by researchers throughout history. From certain industries to nanotechnology, gold has a key role in a wide range of applications.[7]

This thesis includes a study in the heart of nanoscience. It brings together chemistry, biology, and physics to vigilantly research the structural differences in cyanine dyes and the effects of these structural modifications on the photophysical qualities and biological activity. Including gold nanoclusters and combining them with fluorescent probes is a new and exciting application with countless possibilities. In the future, the complex of gold nanocluster and cyanine

dye could be synthesized to be used as a multifunctional tool in biological applications.

1.1 Cyanine dyes

Cyanine dyes are a very well-known class of the wide field of fluorescent probes. Fluorescent probes are molecules or complexes capable of emitting a fluorescent light in desired applications, such as binding with DNA or changing the pH. Fluorescent probes can be organic dyes, ultrasmall gold nanoclusters, or bigger clusters paired with an organic dye. Since the structure of organic dyes is based on a conjugated system, organic dyes are all different yet similar in some ways.[8] Many have aromatic rings, which are known to have delocalized π electrons. These electrons are able to absorb light at a visible range, enabling the fluorescence to occur. Cyanine dyes are known for their high molar abosrptivities, suitable quantum yields, and range of applications.[9]

Cyanine dye was first synthesized by C. Greville Williams in 1856 when he heated a quinoline compound with amyl iodide in an ammonia solution. As a result, he obtained the compound known as Quinoline Blue, which was a bright blue compound as its name suggests. From the original blue color also comes the name cyanine derived from the ancient Greek word kyanos, which stands for blue.[10] Almost 170 years after Williams's first reported cyanine dye, there are thousands of synthesized cyanine dyes today; many are also commercially available, such as the SYBR green dyes.[11,12] The colors of the dyes vary greatly in the visible region[9,13] and some even stretch to the near infrared region (NIR).[14–16] For instance, Mujumdar *et al.*[17] reported a series of dyes, which are analogs of commercially available Cy3, Cy5, and Cy7, with emission maxima between 565 nm and 789 nm, giving a great example of the variability seen in the cyanine dyes with absorption bands in various regions ranging from the visible to the NIR.

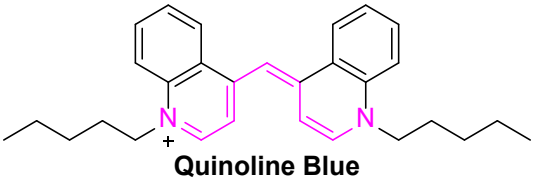

FIGURE 1. Structure of Quinoline Blue.

Quinoline Blue is an example of a monomethine dye, as it has only one carbon in the bridge connecting the two heterocycles. The core seen in all cyanine dyes is highlighted in FIGURE 1 with magenta. This chromophore is the conjugated system between two nitrogen atoms which are usually part of some heterocycles, here in quinolines. Other classes are trimethine, pentamethine and heptamethine, which contain 3, 5, and 7 methine groups in the bridges, respectively (FIGURE 2).

Cyanine dyes can be also unsymmetric, meaning that the two heterocycles containing the nitrogen atoms are different. Besides quinoline, other common heterocycles cyanine dyes can have are benzoxazole, benzothiazole, and indole.[11,12]

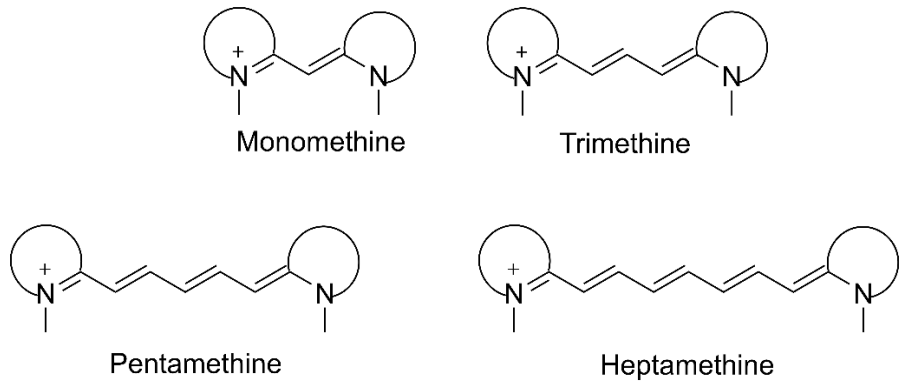

FIGURE 2. Basic structures of different types of cyanine dyes.

Monomethine cyanine dyes have two well-known commercially available brands of dyes, the SYBR Green dyes and TO and YO monomers and their analogs, TOTO and YOYO dimers.[18] The SYBR Green related dyes (FIGURE 3) are the main interest of this thesis. These dyes have been extremely popular, especially for imaging nucleic acids in gels[19] and in many other applications, such as determing virus counts[20] or bacteria[21] from marine samples and diagnosing SARS-CoV-2.[22] Since its initial release in the early 90s, several variations of SYBR Green I have been developed.[23] The SYBR Green dyes have been especially popular as a replacement for ethidium bromide, which is also a nucleic acid stain. However, ethidium bromide has been notoriously known for its mutagenicity and relatively low fluoresence enhancement when bound with DNA; hence, safer and brighter SYBR Green dyes have gained popularity in imaging nucleic acids instead of ethidium bromide in PCR for instance.[24]

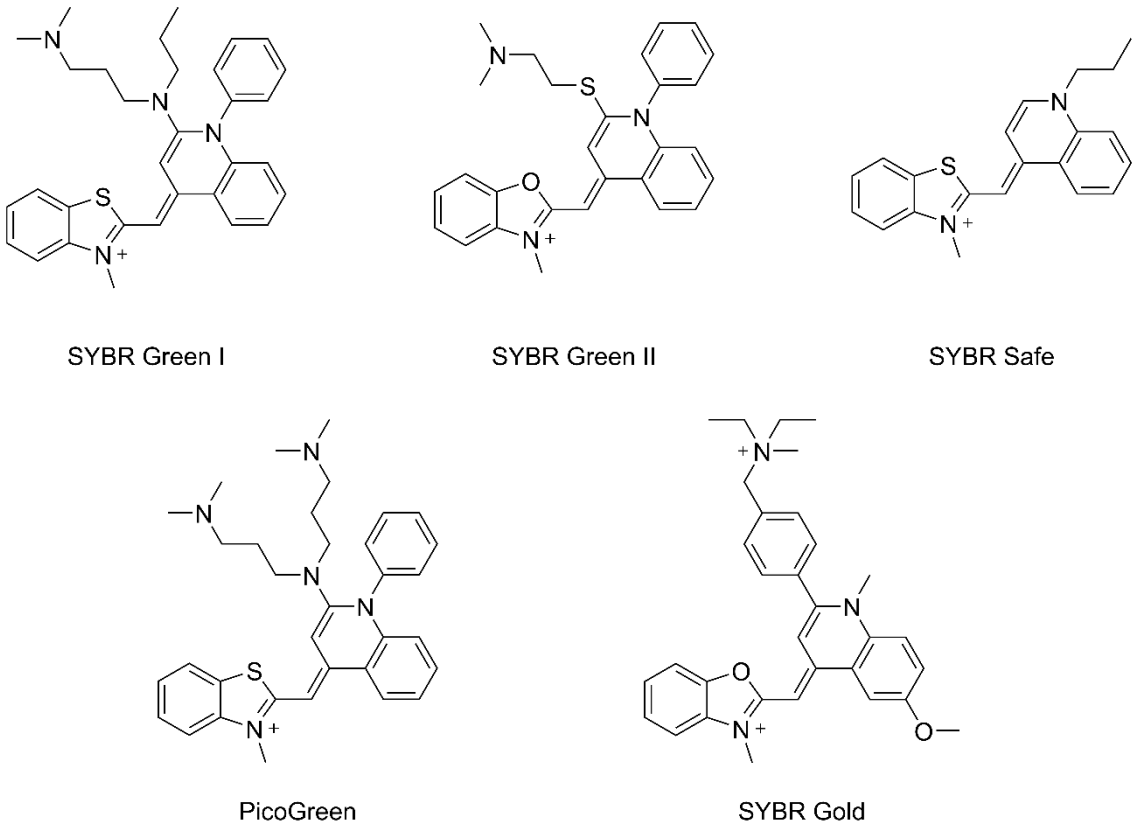

FIGURE 3. SYBR Green related commercially available dyes.[25–29]

Thiazole Orange (TO) and Oxazole Yellow (YO) (FIGURE 4) have been vigorously studied after they were first introduced by Lee *et al.*[30] in the late 80s. Since then, many new analogs of TO and YO dyes have been synthesized and are also commercially available.[18] The dimers TOTO-1 and YOYO-1 have especially become well-known fluoresent probes due to their greater turn-on type of fluoresence in the presence of nucleic acids compared to ethidium bromide with low background emission, as well as high molar abosrptivities of over 100,000 M^{-1} cm^{-1} .[31,32] While the SYBR Green dyes became popular for staining nucleic acids in gels,[23,33,34] the TO and YO dyes and their dimers first gained popularity in cytometry.[30,35,36]

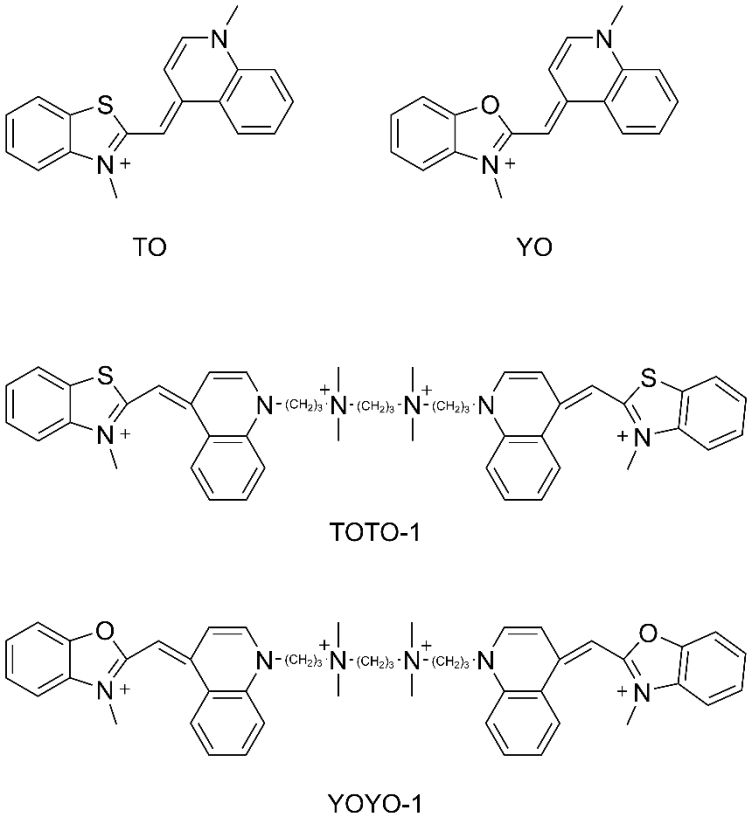

FIGURE 4. Structures of Thiazole Orange (TO) and Oxazole Yellow (YO) and their dimers. TOTO-1 and YOYO-1.[32]

The most well-known polymethine cyanine dyes are Cy3, Cy5, and Cy7 and their analogs Cy3.5, Cy5.5, and Cy7.5 (FIGURE 5), which are symmetrical tri-, penta- and heptamethine dyes, respectively, bearing 3-dimethylindole moieties.[37] These dyes are considered one of the most used fluoresent probes today, with many other variations available commercially as well.[38] The photophysical qualities and the usages of the Cy related dyes have been vigorously studied in new applications thanks to their tunable structures. For example, the detection of reactive oxygen species (ROS),[39] tumor imaging and drug delivery,[40] as well as improving their photostability for prolonged studies,[41] have been studied over the past few years. While the monomethine cyanine dyes are popular in imaging nucleic acids, polymethine dyes have also been a great interest among scientists in medical fields. Their tunable structure and emission maxima in the NIR make PDT therapy possible to treat cancer,[14] in addition to advanced bioimaging and navigation surgeries, along with disease diagnostics.[42]

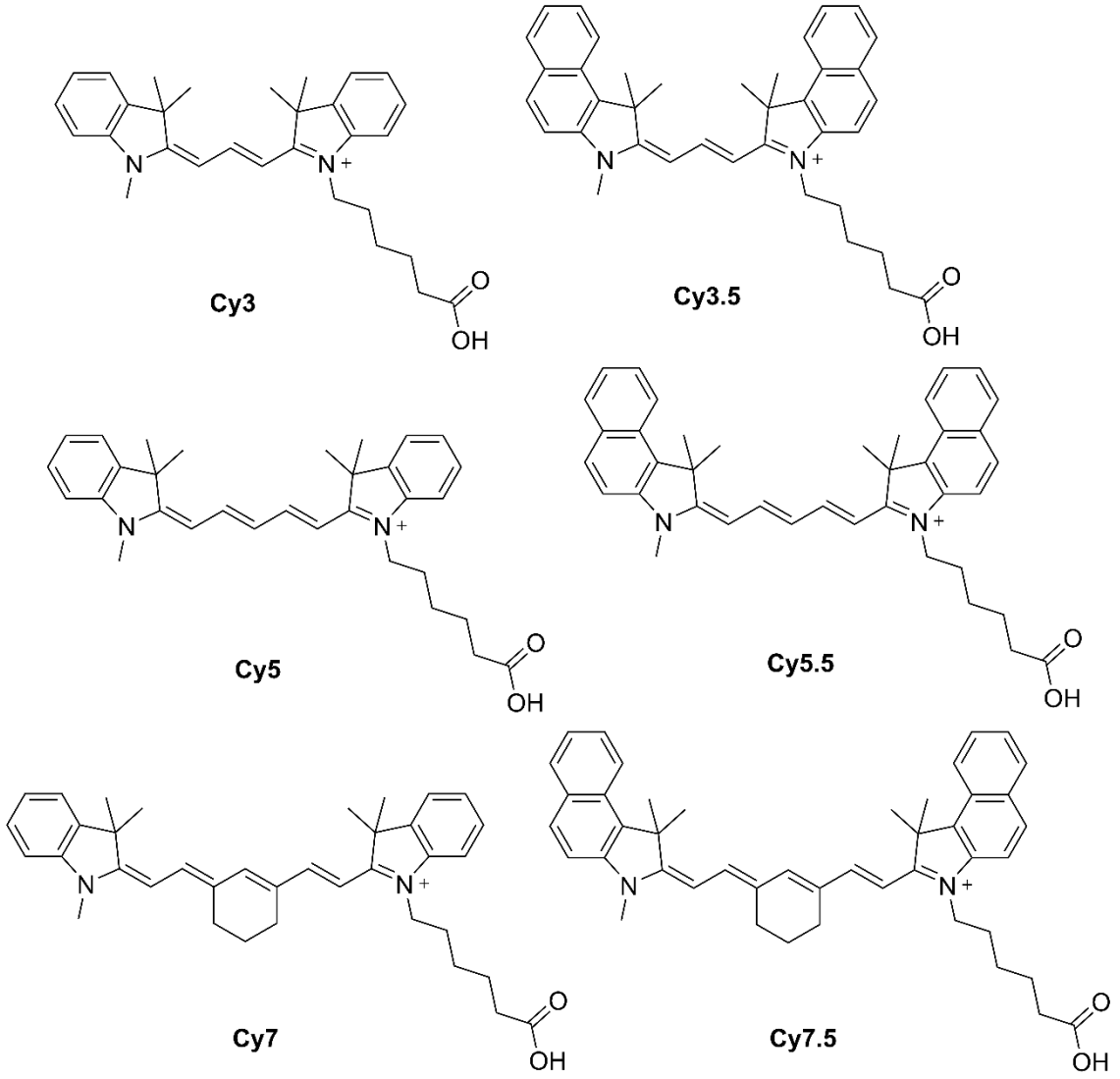

FIGURE 5. Structures of commercially available polymethine cyanine dyes from Lumiprobe.[38]

All the classes of cyanine dyes share some of their qualities. Generally, cyanine dyes can have very high molar abosrptivities, moderate or high quantum yields, sharp absorption peaks, and rather small Stoke's shifts, usually around 20-30 nm. Most importantly, these dyes are capable of binding with high affinities with nucleic acids, proteins or other biomolecules, making them extremely important for life science applications. The most distinctive difference between the classes is the absorption maxima. Monomethine and trimethine dyes both absorb at a visible range; monomethine dyes usually absorb around 450-550 nm, and trimethine dyes generally have maxima around 600-700 nm. Adding another methine group in the bridge shifts the absorption maxima by approximately 100 nm; hence, pentamethine dyes have absorption maxima in the NIR region, around 700-800 nm. And finally, the most redshifted are heptamethine dyes with absorption deep in the infra-red, maxima around 800-900 nm. However, the absorption maxima can be shifted past 1000 nm with additional substituents.[43] This bathochromic shift to longer wavelengths can be explained by the HOMO-

LUMO (highest occupied molecular orbital and lowest unoccupied molecular orbital) energy gap, which gets lower as the polymethine chain gets longer.[44]

1.2 Fluorescent probes in biological applications

When a molecule absorbs light as a photon, the electrons of the molecule are excited from their ground state (S_0) to their excitation state (S_n). Since the electrons need energy to do this jump from the ground state to the excitation state, the absorption will only happen at a certain wavelength in which the energy of the photon is exactly the needed energy for the jump between the states (FIGURE 6).[45]

The excited state is not energetically stable, and electrons need to return to the ground stage. Molecules can relax in several ways. There is always some energy lost as the heat, motion, and vibration of the molecule. Sometimes all the energy is lost in a vibrational relaxation, in which the energy is lost as kinetic energy to the surroundings of the molecule. The vibrational relaxation is also called a non-radiative pathway. There can be also radiationless transitions between the excited states. First, internal conversion can occur between two excited states with the same spin multiplicity, for instance from S_2 to S_1. The second possibility is intersystem crossing, where the transition happens between states with different spin multiplicity, e.g. from singlet to more stable triplet (T_1) state. Some molecules can relax in a radiative pathway known as luminescence. On this pathway, energy is transformed back into a photon, which is then emitted by the molecule in emission. The energy difference between the absorption and emission is called Stoke's shift. There are two ways the emission can happen. In fluorescence, the relaxation in vast majority of cases happens by emission of the photon in the S_1 state. To get to the S_1 stage, an internal conversion can occur before fluorescence. The phosphorescence happens after the intersystem crossing from the triplet state. The notable difference between these two mechanisms is the spin multiplicity. When fluorescence occurs, the spin stays the same, but with phosphorescence also the spin multiplicity changes when the intersystem crossing occurs. Due to the change in the spin multiplicity, phosphorescence takes longer to occur than fluorescence and can be observable in some cases even hours after excitation.[45]

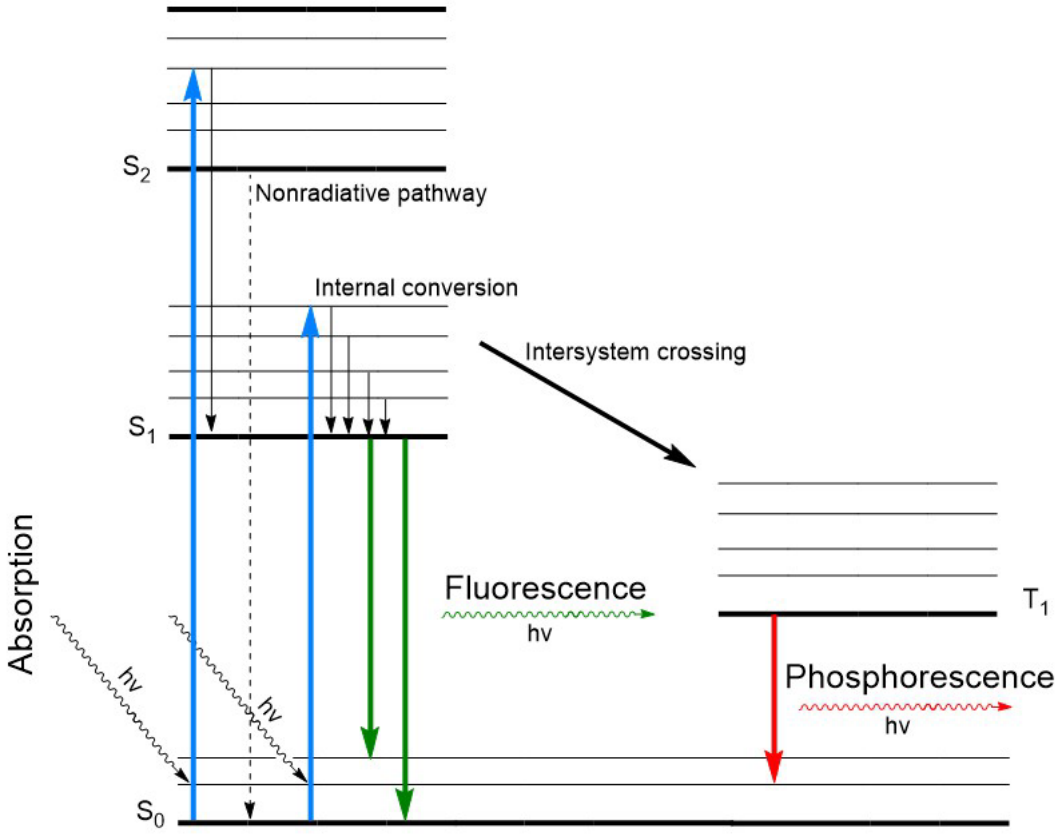

FIGURE 6. Jablonski diagram redrawn using Gomes *et al.*[46] and Klán and Wirz[45] as a reference.

A chromophore as a term has risen from the dye industry to define the part of the molecule, which is responsible for the color of the dye. A chromophore is a group of atoms within a molecule, which is capable of absorbing light in the visible region, hence producing a color of the molecule.[47] There are some functional groups that are commonly found in chromophores. Ketones, carbon-carbon double bonds, conjugated carbon bonds, or conjugated enones are common groups along with aromatic rings.[48]

Photophysical properties of many types of molecules are exploited in biological applications; for example, lanthanide metal organic frameworks (Ln-MOFs) can be used to image anticancer drugs[49] and small organic fluorescent probes, such as ATTO655 or PicoGreen to image biomolecules and cellular structures with super-resolution microscopy.[50] Cyanine dyes are one class of the fluorescent probes utilized, but there are several other classes of molecules with different abilities and advantages. Imaging is the most utilized one, including fluorescent probes to image nucleic acids, e.g., in PCR,[26,33,51,52] as well as imaging biomolecules in cells[53–55] and using nanoparticles[56,57] or gold nanoclusters[58,59] to detect tumors. Monomethine cyanine dyes are widely known for their ability to bind with high affinities with nucleic acids. Hence, they are commonly utilized to image nucleic acids in more and more ambitious studies. One of these

examples is the utilization of the so-called flow virometry to characterize viruses. This is an adaptation of flow cytometry and fluorescence-activated cell sorting, which have been used routinely in the purification and analysis of cells for decades. These methods, however, were not sensitive enough for viruses. With more powerful devices and brighter fluorescent probes, such as SYBR Green I, it is now possible to study viruses more precisely than ever before.[60]

Other common applications are therapeutic tools, which take advantage of photophysics to treat diseases. For instance, photothermal therapy (PTT) is a widely studied mechanism to treat cancer tumors. PTT uses the probe's ability to absorb light and convert it to thermal energy to increase the temperature within the tumors in hopes of killing the infected cells. PTT may be potentially used alongside with photodynamic therapy (PDT). PDT is also a selective method to treat cancer cells by activating the used probe with light to release reactive oxygen species, which could kill the cancer cells.[59,61]

One of the most ambitious goals is to use fluorescent probes to detect reactive oxygen species (ROS) in our bodies. Although ROS are a normal part of the oxygen metabolism, high amounts of ROS have been linked to several diseases, such as cancer, cardiovascular disease, and Alzheimer's. The most common ROS forms are singlet oxygen (O_2), hydroxyl radical, hydrogen peroxide, and superoxide anion (O_2^{*-}). As one might expect, their detection is difficult due to their short half-life and low concentrations.[62] One example of such probes was presented by Albers *et al.*[63] In their studies, they presented a synthesis route for a probe consisting of coumarin donor and fluorescein acceptor protected with boronate linked together with a spacer. Their method is based on the Förster resonance energy transfer (FRET), which means that the donor chromophore is able to transfer energy to the acceptor when excited through a nonradiative pathway. In this case, coumarin can donate energy to fluorescein, but without its reaction with hydrogen peroxide, fluorescein remains in a form unable to emit photons; hence, only emission from the coumarin donor is observed. When the protective groups of fluorescein react with the hydrogen peroxides, the conformation opens up, emitting a strong green fluorescence distinctive from the blue from the donor. This probe was also proven to be selective towards the hydrogen peroxide over other ROS species, and it can detect the hydrogen peroxide produced by the mitochondria.

In some cases, the use of fluorescent probes cannot be categorized only to the imaging, therapeutic or diagnostic purposes since these qualities can be combined. Watanabe *et al.*[64] presented a series of benzothiazolium-based probes. In the solution, these probes exhibited poor fluorescence intensity but when in the presence of β-amyloid or α-synuclein, which are linked to Alzheimer's disease and Parkinson's disease, they exhibit a turn-on type of fluorescence. As proven by the in-vivo and in-vitro testing, one of the presented probes showed promising affinity towards these hallmarks and was able to clearly stain senile plaques and Lewy bodies in brain sections with Alzheimer's or Parkinson's disease. Hence, these probes could be used to selectively image the desired biomolecules and diagnose the disease.[64]

1.3 Noble metal nanoclusters

Atomically precise noble metal nanoclusters are a very unique class of materials and naming them has also been controversial. They have been called nanoparticles, nanoclusters, quantum dots, clusters, quantum clusters, monolayer protected clusters, nanomolecules, artificial atoms, superatoms, and faradaurates, to name a few. It is evident that their extraordinary qualities, including the quantized energy levels, set them apart as a distinct class of materials, differentiating them from nanoparticles. The distinctive feature separating nanoclusters from nanoparticles is their size, which is also the facture determining the molecule-like qualities of nanoclusters. Nanoclusters are often referred to as small or ultra-small; and most commonly, their size is less than 3 nm, and the ultra-small nanoclusters can even be subnanoscale.[65] Nanoclusters are typically defined to be smaller than 10 nm, at which point they are considered to be nanoparticles up until 100 nm (FIGURE 7).[66] The most accurate way to describe these materials is noble metal nanoclusters. However, it is not only the size that makes the nanoclusters stand out from the nanoparticles. In many cases, the exact conformation of the noble metal nanoclusters is known, whereas for the nanoparticles, only the estimated size in nanometers is often known.[67]

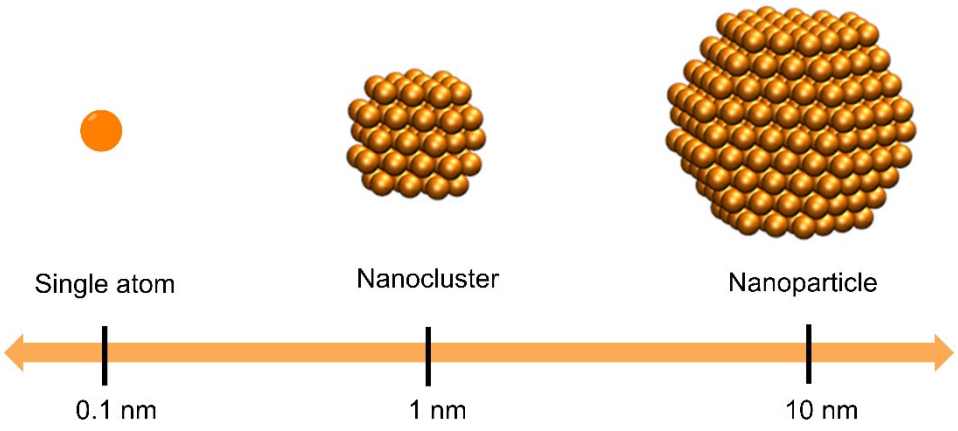

FIGURE 7. The size evolution from a single atom to nanoparticles. Redrawn using Liu and Corma as a reference.[68]

Noble metals are known to be ''tough'' materials, as they do not oxidize in atmospheric conditions. These metals include ruthenium, rhodium, osmium, iridium, palladium, platinum, silver and gold, all of which are also rather expensive due to their scarcity in earth. Most samples of noble metal nanoclusters are either gold or silver since they have been popular in many applications throughout human history, even as a form of medicine.[69]

In this thesis, we will focus primarily on the gold nano**clusters** (Au**NC**s). The discovery of the atomically precise AuNCs is still quite new, as the first example was published in 1981 by Schmid *et al.*[70] and more studies started to emerge in the 1990s,[71–73] when many examples of the improved synthesis

methods arose. The gold nano**particles** (Au**NP**s) have been studied since 1857 when Michael Faraday first introduced his so-called fine particles.[74] Since then, a few breakthroughs in the gold nanoparticle field have changed the industry radically. In 1951, Turkevich *et al*.[75] reported the citrate method to synthesize gold nanoparticles, and in 1973, Frens[76] further improved the method by controlling the ratio of the reducing agent and the cold precursor. To this day, the citrate method is the most used synthetic pathway to get colloidal gold nanoparticles from $HAuCl_4$. However, other reducing agents besides sodium citrate are also used, such as ascorbic acid, sodium boron hydride, or block-copolymers.[77] The mechanism behind the citrate method have been proposed to consist of four steps. First, the Au (III) starts to reduce and form the nuclei. The second step is the aggregation of these formed nuclei. In the third step, the reduction of the gold continues, and particles start to slowly grow. The fourth and last step is the rapid growing step, where all Au (III) is reduced to Au (0) to form the gold core.[77] But because there are so many gold nanoparticles with different shapes, sizes, and ligand variations, the synthesis methods can also vary from the classical citrate method; for example, single crystal seeds can be used as a starting point to grow nanorods,[78] whereas the AuNCs are synthesized by first forming the complex between the gold and the ligand, and this complex is then reduced to self-assembling the nanocluster together.[72] Or by etching bigger AuNPs, with selected ligands to its desired size.[58,79]
The synthesis of AuNCs will be covered in a more detailed manner later on.

Gold nano**clusters** consist of a gold core comprising Au(0) and a protective ligand layer with Au(I) covalently linked with various ligands.[72] Gold nano**particles** are similar in regard to the core and the Au(I) protective layer, but the surrounding ligands are not covalently linked to the particle, and they stay together through ion-dipole bonds.[80]

2 MONOMETHINE CYANINE DYES

Monomethine cyanine dyes are most known for their usage as fluorescent probes to image nucleic acids in different applications. These dyes usually have high absorption coefficients, great turn-on-type fluorescent response to nucleic acids with low background emission and high binding affinities.[9,81] Some drawbacks of the monomethine cyanine dyes include poor photostability and cytotoxicity. However, SYBR Green II and SYBR Gold were proven to be less cytotoxic than ethidium bromide, which is another popular DNA stain.[24] SYBR Gold is the most sensitive SYBR dye; it can detect as little as 34 pg of dsDNA, making it currently the most accurate dye for imaging nucleic acids in gels, which is also the most known application for the SYBR green related cyanine dyes.[34]

2.1 Synthesis

Monomethine cyanine dyes are commonly synthesized with a condensation reaction between two quaternary amine salts in the presence of a base, such as triethylamine or pyridine. The drawbacks of this common route can be low yields, hard purification, and long reaction times.[43] However, the mechanism of this widely used method has not been studied that much, as only some proposals have been made.[3,82] As seen in the mechanism proposed by Fu *et al.*[82] (FIGURE 8), the reaction is started by the base deprotonating the methyl group, which is stabilized by the resonance structure with the positively charged nitrogen. Next, the formed carbanion acts as nucleophile in an S_N1 reaction with the quinoline containing a leaving group. Nitrogen in the quinoline moiety stabilizes the formed intermediate by accepting a lone electron pair. Lastly, the base deprotonates the formed methine bridge and the leaving group is removed to obtain the final cyanine dye structure.

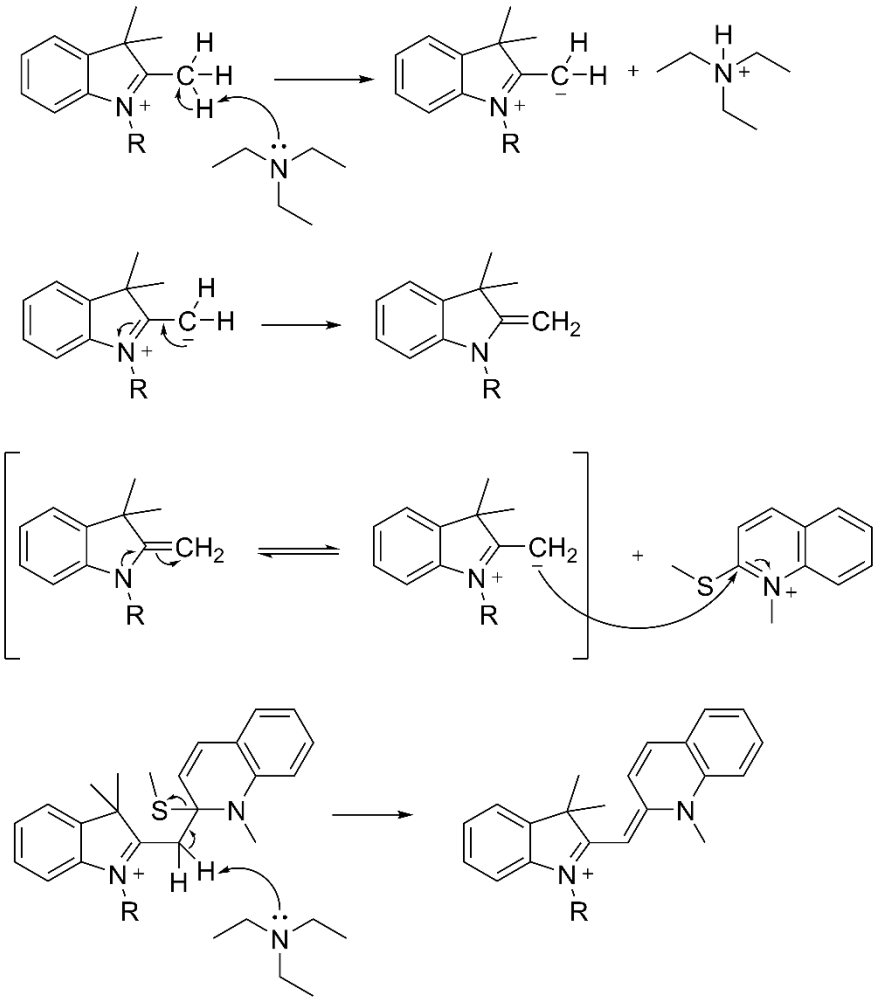

FIGURE 8. Proposed synthesis mechanism by Fu *et al.*[82]

The synthesis of SYBR green related cyanine dyes have been patented since the early 90s.[83,84] This synthesis also consists of two main precursors – the quinoline salt and either benzothiazolium or benzoxazolium salt (FIGURE 9). The first part of the synthesis starts from quinolone, which is treated with a strong chlorinating agent; $POCl_3$ to chlorinate the carbonyl in the presence of a catalytic amount of DMF dissolved in DCM. This reaction yields the quaternary amine salt after 24 hours of refluxing suitable for the cyanine condensation reaction. Next, the prepared chlorinated quinoline is mixed with the benzothiazolium or benzoxazolium salt in the presence of triethylamine after six hours of mixing. Purification with column chromatography results into the chloride substituted intermediate, which is favorable for the substitution reaction for additional functional groups. If desired, the substitution of the chloride may also be done before the cyanine condensation reaction.[83,84]

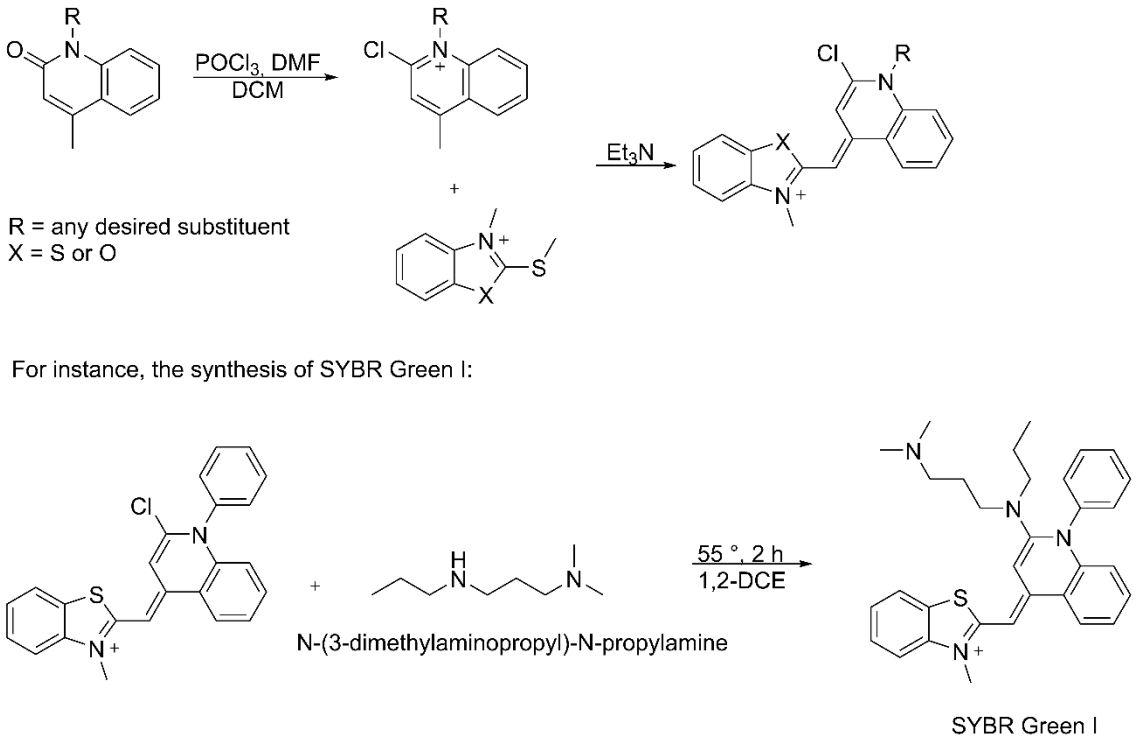

FIGURE 9. The synthesis route for SYBR Green related cyanine dyes.[83,84]

Deligeorgiev has done several studies on the cyanine dye synthesis with various peers in the 1990s.[81,85–88] In addition to improving the overall cyanine condensation reaction in wet chemistry methods,[81,87–89] environmentally friendly synthesis routes with high yields have also been developed.[85,86] Deligeorgiev's take on the green chemistry aspect not only reduces the usage of solvents in the synthesis, but also lowers the reaction times by doing the synthesis simply by melting the starting materials and letting them react from minutes to an hour.[85,86] Moreover, their synthesis method reduces the chances of forming pollutant and toxic methylthiol gas as a side product.[86]

Since scientists share a common goal to reduce pollution and slow global warming, the cyanine dye synthesis has had other examples of green chemistry methods as well. Eissa and Hameed[90] reported a solvent-free synthesis route to various novel monomethine cyanine dyes by using a mortar and pestle. They mixed the two starting materials in the mortar and grinded the salts in the presence of piperidine as a base, resulting in a fast and high conversion to the desired dyes with over 90% yields for each synthesis.

Microwave-assisted synthesis methods have been popular as well; not only do they reduce the need for solvents, but they also typically reduce the reaction times. The Zhang group has reported two methods for the microwave synthesis of monomethine dyes with high yields and fast reaction times, under 20 minutes in solvent-free conditions.[82,91] A similar study was conducted by Hussein *et al.*[92] as they took the challenge to improve the synthesis of the thiazole orange family of dyes. They too applied solvent-free conditions and were able to synthesize products with good yields and short reaction times. The good yields in solvent-

free conditions with fast reaction times also reduces the need for purification steps after the condensation reaction. Purification with classical wet chemistry synthesis procedures can be time consuming and challenging since multiple products may also form, leading to low yields.[85]

Some research outside the classical synthesis route has been also conducted. One-pot synthesis between 1-methyl-2-quinolinethione, quaternary amine salt, and methyl *p*-toluenesulfonate in the presence of triethylamine was reported with reasonable yields and fast reaction times. While this route has only one amine salt, it is very close to the classical method as it also includes the base catalyst. This method also included the purification step by recrystallization and Soxhlet extraction, reducing the cost efficiency of the synthesis even further.[93]

Apart from trying to improve the synthesis, some efforts regarding the functionalization of the dye molecules have been attempted. For example, improving water solubility has been studied by adding another charge bearing functional group. Improving the water solubility is especially important for fluorescent probes that are intended to be used in biological applications to increase the dye's ability to penetrate through the plasma membrane to enhance the dye DNA interaction.[94] Adding another charge to the molecule can also enhance the quantum yields of the dyes, as demonstrated by Deligeorgiev *et al*.[95] and Timtcheva *et al*.[96] Rastede *et al*.[97] reported how adding either an electron withdrawing group (EWG) or electron donating group (EDG) to the benzothiazolium moiety of the TO dye can be used to finetune the spectral properties of the dye. Adding an EWG to the TO dye in this position resulted in blue-shifted spectra, whereas the addition of an EDG resulted in red-shifted spectra. On the other hand, by including the same substituents in the quinoline moiety of the TO dye, these spectral changes were the opposite; EWG resulted in red-shifted spectra and EDG resulted in blue-shifted spectra.

2.2 Applications

2.2.1 Detecting nucleic acids

In 1986, the biological activities of monomethine cyanine dyes were discovered by Lee et al.[30] They used a new monomethine cyanine dye, thiazole orange, in fluorescence cell cytometry to image the reticulocytes, which are immature red blood cells containing RNA that eventually will mature into red blood cells. Since this discovery, the field of cyanine dyes has risen exponentially. Today, there are several modified versions of thiazole orange and other families, such as SYBR dyes, that are commercially available.

Using the cyanine dyes to image nucleic acids is dependent on their ability to interact with them. When the cyanine dye is in an aqueous solution without any nucleic acids, very low background emission is typically detected. But when bound with nucleic acids, the fluorescence lights up. This has been explained by the core of the dye fixing to the binding site, so that the backbone of the dye

molecule becomes rigid, and the relaxation cannot happen via twisting and turning anymore. Because of this, it makes many imaging applications with these dyes very easy since there are no blue or red shifts or a certain increase in the intensity – when there are nucleic acids, the fluorescence becomes visible; otherwise, there is no fluorescence. There are few explanations how this phenomenon occurs. The Geddes group[25,28] has extensively researched the interactions of SYBR Green I and PicoGreen and how they bind with double stranded DNA. Their studies show that these dyes intercalate between the base pairs of the double helix, while the positive charge provides additional electrostatic interactions; to finalize the tight binding, the long side chains can interact along the helix, providing another weak interaction as a support. The other possibility is groove binding. Karlsson *et al.*[98–100] reported several asymmetric monomethine cyanine dyes that bind with the minor groove of the dsDNA with weak interactions (FIGURE 10).

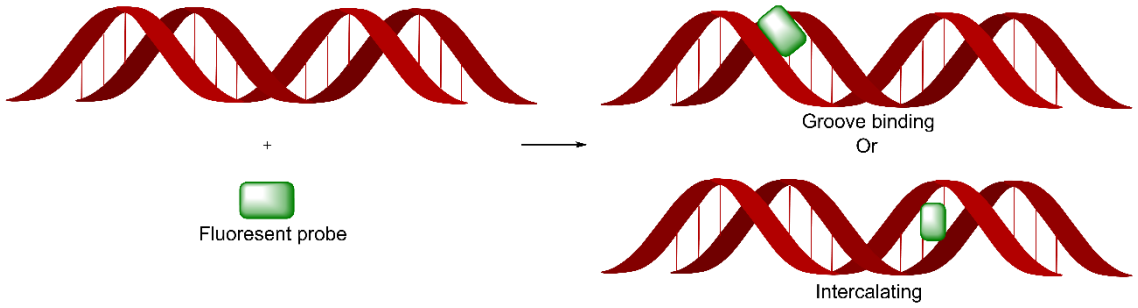

FIGURE 10. Simplified binding modes of fluorescent probes with double stranded nucleic acids.[28,100]

One of the most known applications of monomethine cyanine dyes is the polymerase chain reaction (PCR),[22,98,101–103] which is used to reproduce DNA segments.[104] Another widely used technique is the melting curve analysis, which can be used to further analyze the DNA amplified with PCR.[105–107] It is also common to image nucleic acids in gel electrophoresis with monomethine cyanine dyes.[33,108,109]

PicoGreen, which is also part of the SYBR Green family, can be used in a super-resolution (SR) microscope imaging tool. A more advanced method of SR is direct stochastic optical reconstruction microscopy (dSTORM), which is capable of imaging proteins in living cells. Using PicoGreen as fluorescent probe for imaging cellular DNA in living cells with dSTORM has been successful, even over a long period of time. This method may be a potential way to study how the DNA organizes over time and how that affects the gene expression in different regions of the DNA.[110]

The interest towards RNA and its applications and functions, such as RNA vaccines and RNA-based drugs, has risen drastically over the last few years.[111] Also, the ambition to design a RNA-specific dye is at an all-time high. Few

attempts to make an RNA-selective dye has been made in the monomethine cyanine dye field. One of the most known examples is SYBR Green II, although it is not fully RNA-selective. It can be also used to image DNA, but it has higher affinity towards RNA.[112] Other example of commercial dyes is SYTO RNA select which is one of the few RNA-targeting dyes available, but its structure is not known. Hence, it cannot be further developed to be used in new applications. However, Lu *et al*.[113] were able to combine the RNA-specific features of styryl dye and monomethine cyanine dyes. Their molecule has a monomethine cyanine dye core combined with a p-(methylthio)styryl unit. This dye, Styryl-TO, showed higher affinity towards RNA compared to DNA, along with a 152-fold increase in fluorescence intensity when bound with RNA and an increase in the quantum yield when bound (35-fold). It was also proven to be quite photostable, making the studies possible even with prolonged exposure to light. The quantum yield and light-up are on the lower side compared to conventional cyanine dyes, such as SYBR Green I, but this study is an important indication that RNA-specific monomethine dyes are plausible.

Another attempt to provide RNA-specific monomethine cyanine dye was made by Aristova *et al*.[114] They designed several unsymmetric dyes with benzothiazolium or –oxazolium moieties combined with quinoline or pyridine moiety as a core. With various substituents, they screened the possible RNA activity and their best dyes, Sl-2000 and Sl-2598, both show over a 400-fold increase in emission intensity when bound with RNA. The Sl-2000 dye has a unique composition; its structure has negatively charged oxygen in the quinoline core, and it has positively charged triethylamine substituent connected to the positively charged nitrogen in the quinoline core. Even though these dyes were proven to have affinity towards RNA and have great turn-on fluorescence when they bind with RNA, they still show some affinity towards DNA as well. Hence, if only RNA imaging is the desired goal, even these dyes are not yet fully capable.

An interesting new application of using commercially available monomethine cyanine dyes, such as SYBR Green I and TOTO-3, with a laser confocal microscope has also been studied. A laser confocal microscope can be used to locate cell components in cellular environments. With different types of dyes, it would be possible to selectively dye different parts of the cells, such as using DNA-targeting dye and dye for active filaments. SYBR Green I showed great affinity towards DNA in this study. As it did not dye the majority of the cytoplasmic RNA, SYBR Green I could be used to image DNA without a RNAse treatment, which is required for dyes that have higher affinity towards RNA. TOTO-3 did the opposite, as it had a higher affinity towards the RNA in this experiment. Both these dyes, as well as the other TOTO family dyes that were studied, could be used to stain DNA in laser confocal microscope studies.[115] A similar notion was made by Henneberger *et al*.[116] They used a confocal laser microscopy to image microbial cells in soil samples with great results. TOTO-3 and TO-PRO-3 showed low background emission, and they were able to image the cells from the measured samples without any harsh pretreatments.

Using fluorescent probes to target specific sites in cells has been an interest in the field of cyanine dyes for some scientists. Atanas *et al.*[87] reported five new monomethine cyanine dyes carrying two positive charges. These dyes were investigated with dsDNA and RNA. According to their studies, their dyes intercalate with the DNA and when binding RNA, the dyes form aggregates that are able to bind with the RNA. When utilizing the dyes *in vivo* with a HeLa cell, they noticed that the dyes tend to accumulate into the mitochondria of the cells. Hence, these dyes may have some potential usages targeting the mitochondria.[87]

When bound to nucleic acids, the great turn-on type of fluorescence of cyanine dyes makes many applications possible; from the classic applications of PCR, melting curve analysis, and gel electrophoresis for imaging DNA under the microscope (dSTROM) to a RNA-specific dye for selectively imaging RNA, even in the presence of DNA.

2.2.2 Other applications

Since the imaging nucleic acids is by far the most studied application of the monomethine cyanine dyes, there are only a few examples of other applications. Some interesting examples of other usages of monomethine cyanine dyes are listed below.

Biological applications of monomethine cyanine dyes do not stop with detecting nucleic acids. Ten novel monomethine cyanine dyes were synthesized, and their antimicrobial activities were studied by Abd El-Aal *et al.*[117] The results of their study indicated that three dyes showed great antimicrobial activity towards gram positive bacteria. While the study did not show whether the effect was inhibitory or lethal, its great effect was observed.[117]

Few studies have been conducted on using monomethine cyanine dyes to image proteins. An example of protein imagining dyes was published by Yarmoluk *et al.*[118] They presented a total of 11 novel monomethine cyanine dyes, which were proven to have a turn-on type of fluorescence in the presence of albumins, bovin serum albumin (BSA), and human sera albumin (HSA). Their study did however show that these dyes also had the characteristic turn-on type of fluorescence with DNA and RNA, hence the proteins could not be selectively imaged.

Abdelbar *et al.*[119] presented a quantum dot combined with monomethine cyanine dye as a method to improve the performance of solar cells. In their applications, they introduced the ionic cyanine dyes on top of the solar cell using an ethanol solution and small voltage to aggregate the cyanine dyes on top of the titanium dioxide film. On this thin film, the quantum dots were casted to improve the overall absorbance of the solar cell.

A study by Vus *et al.*[120] compared the possibility of different types of cyanine dyes inhibiting the insulin fibrillization. Amyloid fibrils are aggregated proteins. The formation of the amyloid fibrils can be linked to many illnesses, such as Alzheimer's and Parkinson's diseases. In this study, it was evident that the length of the methine bridge did have an effect on the inhibitor ability, as the tri- and pentamethine dyes inhibited the formulation of the fibrils completely.

The chosen monomethine dyes did not perform the best as inhibitors, but they too had an inhibitor effect; hence, they may be also used at this application with further modifications to improve the inhibitor effect.

Detecting the amyloid fibrillar has been also studied, using several monomethine cyanine dyes and with some polymethine dyes. The probe that was previously used to image the amyloid fibrillar Thioflavin T has some drawbacks that this study was set to overcome. The quantitative analysis of the fibrillization degree is an important aspect and can be achieved with selective probes. Similar to the above-mentioned study by Vus *et al.*,[120] the polymethine dyes performed better than the monomethine dyes, but the enhancement of fluorescence was also observed in monomethine dyes with the fibrils compared to their free form. This study also gives great insight into new applications for monomethine cyanine dyes with the correct modifications.[121]

Some studies on using cyanine dyes as optical record media like DVDs have been made. Both polymethine and monomethine cyanine dyes have been investigated by several groups with different stabilizing agents, such as transition metals, to improve the photostability. The dyes are used in this application as a thin layer of film on top of the disk, enabling the media recording.[122–124]

Using monomethine cyanine dyes in other applications beyond imaging nucleic acids is a less popular field, but it does provide some interesting possibilities. Detecting the amyloid fibrillar to aid with the disease diagnosis, and imaging proteins and bacteria, as well as producing quantum dots or DVD data storage, are very interesting applications and prove the versatility of the monomethine cyanine dyes and the likelihood that there are many undiscovered applications for them.

3 GOLD NANOCLUSTERS

In the last few years, ultra small gold nanoclusters and atomically precise gold nanoclusters have been a great interest of many researchers. Ultra small gold nanoclusters are also fluorescent with the right ligands. Hence, they have been studied vigorously to be used as fluorescent probes in life science applications due to their excellent qualities, great biocompatibility, bright emissions, large Stoke's shifts, and good photostability.[125] Since AuNCs have these great qualities on their own, the interest of making new types of materials with AuNCs – even combining them with organic dyes – has significantly grown over the years.[126]

3.1 Synthesis of water-soluble gold nanoclusters

The synthesis of atomically precise gold nanoclusters is as challenging as it sounds. Hence, after the extensive studies, the Brust-Schiffrin route[72] is still the most used method to synthesize the nanoclusters. The original method consists of a two-phase liquid comprising water and toluene in which the clusters are grown from gold chloride salt ($HAuCl_4$), and using the phase transferer to bring the two starting materials into the same phase, and with suitable reducing agents, the self-assembly of the gold nanocluster is achieved. Since then, a modified version of the Brust-Schiffrin method in a one-phase manner has been introduced and widely utilized. In this version, water and another miscible solvent, often methanol, are combined.[71]

The so-called magic number is something that comes up when studying the challenging world of gold nanocluster synthesis. The magic number can be described as follows:

$$N = \frac{(2n+1)(5n^2+5n+3)}{3}. \quad (1)$$

Where n is any positive whole number. This N then describes the number of the gold atoms leading to a completely filled electronic shell, which is preferred for

the final core.[127] The core needs to be stabilized to obtain the final nanocluster product. This can be achieved with different types of thiol ligands,[128–135] DNA[136,137], proteins,[138,139] or peptides,[140–143] for instance.

The basic principle of the bottom-up style Brust-Schriffin synthesis method is the controlled growing of the gold nanoclusters. First, the Au(III) starting material forms a complex with the chosen organic ligand (-SR), Au(I)-SR. Then by adding a strong reducing agent, such as $NaBH_4$, a reduction of Au(I) to Au(0) is achieved, and the formation of the cluster itself can begin (FIGURE 11).[72]

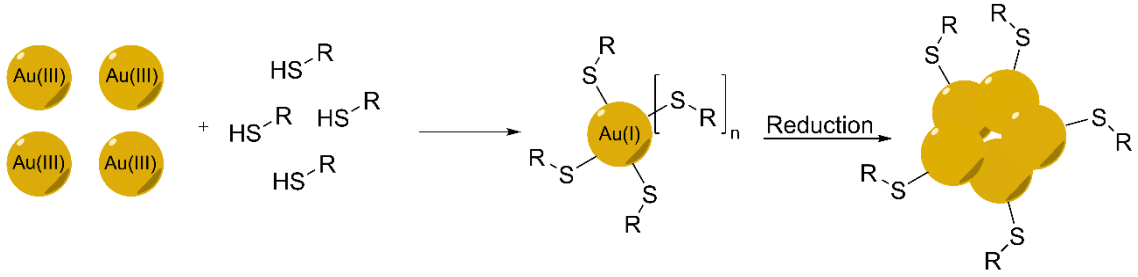

FIGURE 11. General route for the Brust-Schriffin method to synthesize gold nanoclusters from HAuCl4 (Au(III)) protected with a thiol.[72]

Another way to synthesize gold nanoclusters is by etching bigger gold nanoparticles to the desired size, which is typically done by carefully selecting the ligands, usually thiols. As the Brust-Schriffin method is called bottom-up, logically, this method is referred to as the top-down method.[79,144]

Life science applications of gold nanoclusters require water-soluble clusters. Water solubility can be achieved with certain ligands, such as glutathione, as Katla *et al.*[145] reported with their atomically precise Au_{25} protected with glutathione. A similar, very well-known example of water-soluble gold nanoclusters was reported by Tsukuda *et al.*[140] with glutathione or homo-glutathione ligands. Additionally, Shang *et al.*[146] reported fluorescent D-penicillamin (DPA) protected gold nanoclusters for imaging cells. Two of the very common thiol ligands to produce water-soluble nanoclusters are 3-MBA[128–131] and *p*-MBA.[132–134,147] The *p*-MBA protected Au_{102} cluster has been studied in more detail regarding its water solubility. Au_{102}(*p*-MBA)$_{44}$ is water-soluble when the ligand layer is partially or fully deprotonated, and soluble in short chain alcohols when fully protonated. The state of protonation can be tuned with acids and bases without damaging the cluster, thus making the solubility tunable.[148] Similar to water-soluble dyes, some applications can benefit from organosoluable nanoclusters. This can be achieved with ligands. Qian *et al.*[135] reported a thiol-protected $Au_{144}SR_{60}$ cluster with phenylethylthiol as a ligand. Another ligand that has demonstrated to produce a library of different-sized organosoluable nanoclusters is *n*-dodecanethiolate.[149]

To overcome the challenges of controlling the size of the nanoclusters, different types of templates have been studied. For example, single-stranded DNA can be used as a template,[136,137] as well as proteins.[138,143] The DNA used in these examples are single-stranded and it wraps around the gold core to form the

protective layer as the other ligands do.[136,137] And since proteins are close relatives of DNA, they behave as templates similarly, wrapping around the gold core to form the protective layer.[138,143]

Over the 30 years of developing a novel synthesis of atomically precise gold nanoclusters, a few examples of important aspects have been discovered. These include the pH of the solution,[150] the molar ratios of the gold salt and the used ligands,[140,145,150] and the temperature of the reaction.[140,145]

3.2 Applications of gold nanoclusters with fluorescent probes

Combining fluorescent probes with gold nanoclusters is still a quite recent innovation and only a few examples exist. Ultrasmall gold nanoclusters are fluorescent on their own and they have been utilized in many applications, such as detecting Hg^{2+}[151] or glutathione.[142] However, using non-fluorescent bigger nanoclusters and covalently linking them with fluorescent probes could be a way to create multifunctional tools.

Pyo *et al.*[126] described an Au22 gold nanocluster linked with fluorescein as a pH meter for cells. This cluster produced an increase in the photoluminescence intensity along with a higher pH (ranged from 4.3 to 7.8). This probe was also proven to be photostable under prolonged irradiation and biocompatible with low cytotoxicity. These clusters could also be linked, e.g., with drugs or target agents to gain the multifunctional tool for desired applications.

In 2016, Wu *et al.*[152] reported bovin serum albumin (BSA)-stabilized gold nanocluster covalently linked with fluorescein-5-isothiocyanate (FITC). Their Au25 BSA cluster is fluorescent on its own and when combined with also fluorescent FITC, they were able to simultaneously observe changes in the pH with the fluorescein, and the BSA-protected gold nanocluster responded to changes in the temperature. This cluster was also very photostable and biocompatible, as they were able to observe the changes in the temperature and pH of HeLa cells. In this case, the fluorescein emission intensity gets stronger when the pH rises, and the increasing temperature will quench the emission intensity arising from the BSA protected cluster. Hence, this approach takes advantage of the self-fluorescence of the BSA-protected cluster and combines it with the known ability of FITC to respond to the pH changes.

The advantages of the modifiable ligand layer of gold nanoclusters do not end with pure imaging tools. Li *et al.*[153] combined a small gold nanocluster with a targeting ligand for pancreatic cancer cells, cathepsin E (CTSE)-sensitive PDT therapy prodrug, and a CTSE-sensitive imaging agent, cyanine dye Cy5.5. CTSE is an aspartic proteolytic enzyme, which is overly expressed in many forms of cancer, including pancreatic cancer. With these tools combined (FIGURE 12), they were able to see a turn-on type of fluorescence when the gold nanocluster reached the target as the fluorescent Cy5.5 ligand released from the ligand layer. The confocal laser endomicroscopy can then be used precisely where the tumor was, inducing the PDT/PTT therapy to kill the tumor cells. This method was

further studied with mice, and it was proven to shrink the tumors significantly and keep the mice alive. The gold nanocluster probe had low cytotoxicity without laser irradiation and effectively killed the tumor cells with PDT/PTT therapy.

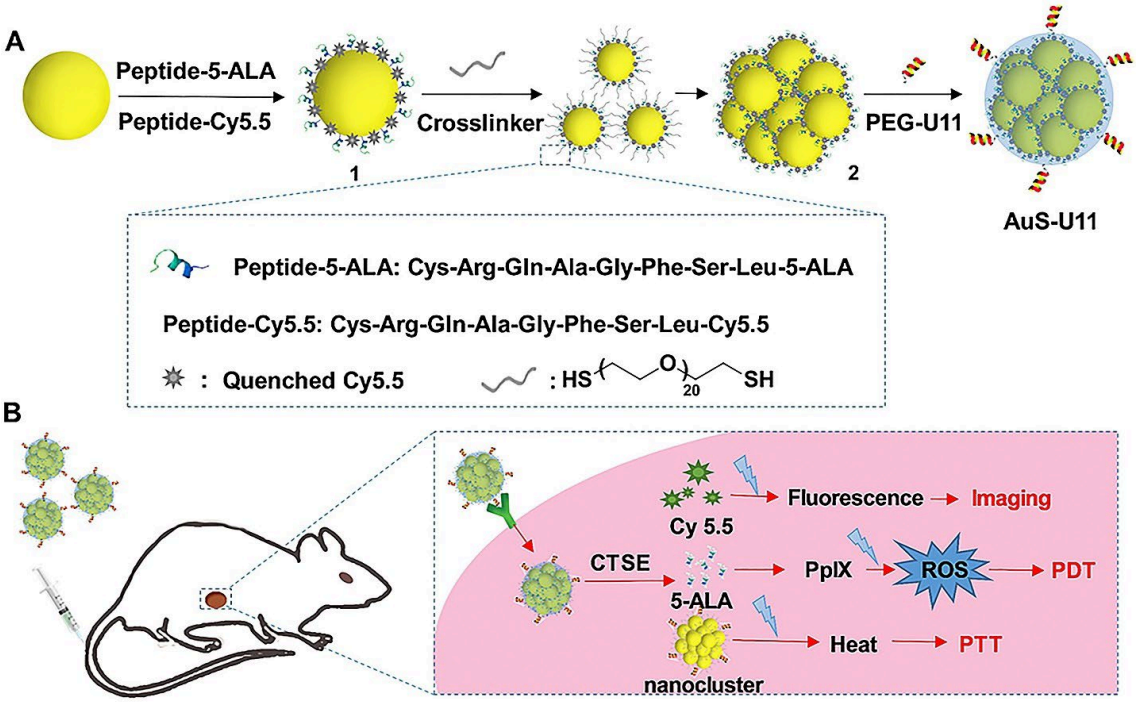

FIGURE 12. Schematic illustration of the synthesis and operating mechanism of the gold nanocluster probe AuS-U11. Reproduced from ref. [153] with kind permission from Elsevier.

Thus far, the examples of fluorescent probes and gold nanocluster complexes have been used to detect the pH[126,152] or temperature,[152] as well as a part of the multifunctional tool for cancer treatments.[153]

4 EXPERIMENTAL METHODS

4.1 Photophysical measurements

Throughout the research, photophysical measurements were carried out, as they are one of the most important parts of the study to investigate the structural differences and their effect on the dyes' photophysical qualities. It was of high interest to understand the different instruments and determine which available instrument would be the best for our needs. Similar measurements have been carried out in the research group, and they have been previously included in a thesis as well.[154]

For absorption, three devices were used for the measurements. First, the studies were carried out with a Varian Cary 100 spectrophotometer. The studies were continued with a Perkin Elmer 650 UV-vis spectrometer or an Agilent Technologies Cary 8454 UV-vis spectrometer. All the devices have the same operating mechanisms. They have a single cuvette sample chamber where light comes through a monochromator to the sample and finally to the detector. Cross-checking was conducted to ensure that the devices produced reliable data complimentary to each other.

Varian Cary Eclipse was used for measuring the fluorescence. Similar to Uv-vis spectrometers, fluorometers also operate on the same basic principle regardless of the instrument of choice. The excitation light is directed to the sample through a monochromator, which will emit photons that are detected with a photodetector. A photomultiplier is used to strengthen the observed intensity from the sample.

Molar absorptivity (ε_{max}), is one of the values one would expect to find when reading a study about fluorescent probes. According to the Beer-Lambert law:

$$A = \varepsilon c l, \tag{2}$$

where A is absorbance, ε is the molar absorptivity, c is concentration and l is pathlength (1 cm in regularly used 10x10 mm cuvette). Hence, molar absorptivity can be described as the relationship of absorption and the concentration of the sample. It gives a more comprehensive number that can be used to compare how well the studied samples absorb light regardless of the sample concentration.[155]

Along with molar absorptivity, quantum yield is one of the basic values you need to evaluate fluorescent probes. Quantum yield can be determined using known standards, as presented in the following equation (3):

$$\Phi_{sample} = \Phi_{std} \frac{A_{std} F_{sample} n_{sample}^2}{A_{sample} F_{std} n_{std}^2}, \quad (3)$$

where, Φ is the quantum yield, A is absorbance, F is integrated emission and n is refractive index. In practice, to make the error smaller, a plot can be drawn as a function of integrated fluorescence against absorbance. The slope of this plot can be described as:

$$Grad_{std} = \frac{F_{std}}{A_{std}}. \quad (4)$$

Similarly, the gradient can be described for the sample:

$$Grad_{sample} = \frac{F_{sample}}{A_{sample}}. \quad (5)$$

And hence, equation (3) can be written as:

$$\Phi_{sample} = \Phi_{std} \frac{Grad_{sample} n_{sample}^2}{Grad_{std} n_{std}^2}. \quad (6)$$

Now, by plotting the integrated emission against absorption at the excitation wavelength, the gradients can be used to determine the quantum yield with equation (6) using a known standard, such as fluorescein.

To gain insight on how the cyanine dyes interact with DNA, a model designed by McGhee and von Hippel can be used to estimate the binding constant and binding site size for the dyes or other ligands as well. They described the DNA strand as a lattice with reoccurring binding sites fit for one ligand each for the guests. They described the binding of the ligands with an equilibrium reaction.[156]

$$\frac{[Bound\ ligand]}{[Free\ ligand]} = K \times [Free\ binding\ sites], \quad (7)$$

Here, K is the association constant for the ligand binding. The ligands considered in this model can bind into the same lattice, but the position of the second binding

ligands depends on the first bound ligand. This means that the binding sites with the bound ligands are unavailable for other ligands to bind, but the space between them can be unavailable if there is not enough space for another ligand. Hence, the authors of this model the probabilities for available (P_{free}) and unavailable (P_{bound}) binding sites as:

$$P_{free} = \frac{1 - nv}{1 - (n-1)v} \tag{8a}$$

and

$$P_{bound} = \frac{v}{1 - (n-1)v}, \tag{8b}$$

where v is the binding density of the bound ligands in the DNA and n is the binding site size in the lattice taken by a single ligand. This model does not consider interactions between the ligands. If there would be some attraction, e.g, between two ligands, it would need to be taken into account. However, this is a model commonly used for cyanine dyes, so the ligand interaction model is not presented here. Without getting into the mathematical details, combining equations (7) and (8) gives the following model:

$$\frac{v}{L} = K_a \frac{(1 - nv)^n}{(1 - nv + v)^{n-1}} \tag{9}$$

where L is the number of unbound ligands and K_a is the association constant when ligands bind with DNA. Hence, the model estimates the ratio of bound and free ligands as a function of the association constant and the ratio of the binding site size and bound dye molecules. To use the model with experimental data, the number of bound and free dye molecules needs to be known. Luckily, with monomethine cyanine dyes, this can be done with fluorescence since the dyes exhibit a turn-on type of fluorescence, which can be used to estimate the amount of bound and free ligands. Hence, the ratio of bound and free ligands can be estimated as:

$$\theta = \frac{F}{F_b}, \tag{10}$$

where F is fluorescence observed from the sample with a restricted amount of binding sites and F_b is the estimated fluorescence of 100% bound dye at the same dye concentration. F_b is estimated by measuring fluorescence in high excess at binding sites and hence, all the used dye should be bound with the DNA. This data is fitted to a linear fit, and the gradient is used to calculate the F_b at the concentrations used to record F. Hence, the amount of the free dye can be described as:

$$L = (1 - \theta)c. \tag{11}$$

And since the v is the binding density of the ligands in the DNA strand, it can now be presented as:

$$v = \theta \frac{c}{c_{DNA}}, \tag{12}$$

where c is the concentration of the dye in the sample and c_{DNA} is the concentration of DNA in the sample. To get the binding parameters from the experimental data, v/L is plotted as a function of v. This exploration gives a nonlinear fit and estimated values for binding constant (K_a) and binding site size (n) in base pairs.

4.2 Characterization methods

The characterization of the dyes was mainly done with mass spectroscopy and confirmed with NMR. Photophysical studies were used to study the behavior of the dyes with and without DNA. X-ray crystal structures were used to confirm the structures of the dyes by our collaborators.

MD simulations were done by our collaborators to investigate the relationship between the dyes and DNA in solution form. These results produced important information about the weak interactions and the conformations of the dyes when bound with DNA.

4.2.1 Mass spectrometry

In Mass spectrometry (MS), ions are produced from the analyte with a selected method suitable for the sample. After ionization, the formed ions are separated according to their mass-to-charge ratio (m/z), and finally, these ions are detected quantitatively and quantitatively based on their abundance (FIGURE 13).[157]

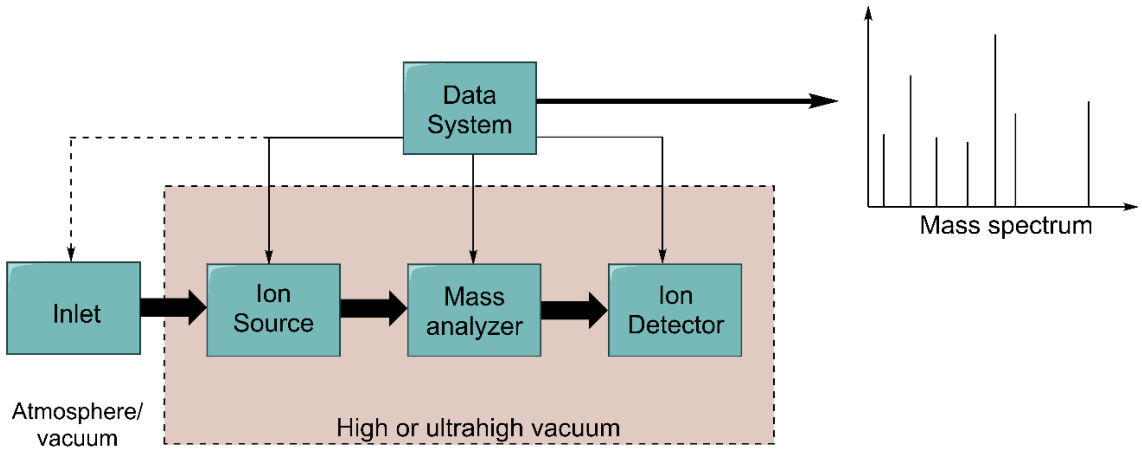

FIGURE 13. Simplified setup for MS. Redrawn from the book by Gross.[157]

During the research, two mass spectrometers were used: Micromass LCT ESI-TOF and Agilent 6560 LC-IMMS-TOF. The Micromass spectrometer was used for standard checkups to see if the synthesis had worked, and to make sure the product was pure before moving on to the Agilent spectrometer. The Agilent spectrometer is a state-of-the-art instrument that is also capable of UHPLC studies and ion mobilization (IM) studies besides the MS measurements. In our case, the device was only used to measure accurate mass of the synthesized products.

ESI stands for electrospray ionization, which is the so-called soft ionization method, meaning that in most cases, the analyte does not fragment. In ESI, the analyte is dissolved in a volatile solvent, methanol for instance, in low concentrations. Starting from the atmospheric pressure, the sample is driven through a high voltage electric field and then ejected to a capillary to form charged droplets. These droplets enter the spray chamber where heated gas, such as nitrogen, starts to evaporate the solvent, making the droplets smaller. Eventually, only the analyte ion is left as a gas phase ion. These ions can then be directed to the mass analyzer, such as a time-of-flight (TOF) analyzer.[157] Agilent has introduced their improved take on ESI, called an Agilent Jet Stream (AJS). This ionization method is similar to the standard ESI method, but it uses superheated nitrogen to improve the desolvation and ion generation, making AJS more sensitive compared to ESI.[158]

Both instruments used a time-of-flight (TOF) analyzer. This means that the formed ions were separated by time – smaller ions take less time to travel through the drift tube to the detector than bigger ions. TOF provides fast detection, high sensitivity, and accuracy, and in theory, there is no m/z limit that can be detected.[157]

4.2.2 NMR spectroscopy

To confirm the molecular formula of the synthesized products, NMR spectroscopy was used along with MS studies. Due to the ionic nature of the dyes, MS was the chosen method when synthesizing products to confirm that the synthesized material matched the desired product. MS was fast and provided information about the purity of the sample. The MS peaks corresponded to the molecular weight of the samples, making it possible to characterize the samples on the spot without needing to interpret the data further. However, MS data alone is not sufficient evidence that the product is what we think it is since the same molecular weight can have very different molecular formulas. Two NMR spectrometers were used during the studies: a Bruker Avance III HD 300 MHz spectrometer was used for routine checkups to confirm the sample purity before measuring the publication quality data, and 2D measurements with a Bruker Avance III 500 MHz NMR spectrometer. With NMR measurements and the MS data, we were able to – with great certainty – say that the synthesized molecules matched the synthesis plan.

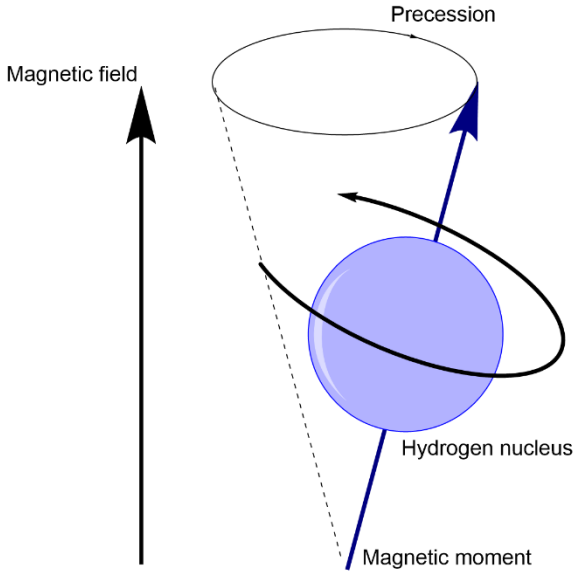

FIGURE 14. Basic principle of NMR. Picture redrawn using Günther[159] as a reference.

Nuclear Magnetic Resonance (NMR) spectroscopy is based on the magnetic properties of a nuclei. When the sample is placed on the NMR device, it exposes the nuclei of the sample to the strong external magnetic field (B_0). Each nucleus in the sample has a magnetic moment, or a spin, which will be aligned according to the external field – and it will spin like a spinning top, called precession FIGURE 14). When a pulse of radio frequency is used, the nucleus can absorb the pulse if it matches the precession frequency. After the excitation, spins return to the ground state, inducing a resonance signal, which is recorded as the function of time. Hence, NMR requires that the nuclei have non-zero magnetic movement,

meaning that ^{12}C with even mass and atomic number does not respond to the external magnetic field. Hence, only the ^{13}C isotope can be detected with NMR along with ^{1}H and ^{19}F for instance. After the Fourier transform, the NMR spectra shows chemical shifts for each different proton. The chemical environment makes the protons have different chemical shifts; for example, the proton near the oxygen atom is more shielded compared to a proton that only has carbon or other protons near it. Because less shielded protons feel the external magnetic field more strongly, their spinning frequency is also higher, creating a more downfielded chemical shift.[159]

4.2.3 X-ray crystallography

Since MS and NMR can be only used to verify the molecular formula and rough estimate of the actual structure with the 2D NMR experiments, X-ray crystallography was used to determine the actual conformations of some of the dyes. Suitable crystals were measured by our collaborators with a Rigaku XtaLAB Synergy-R diffractometer equipped with a HyPix-Arc100 detector and an Oxford Cryostream 800 cooling system using mirror-monochromated Cu-K_α radiation (λ = 1.54184 Å), or a dual-source Rigaku SuperNova diffractometer equipped with an Atlas detector and an Oxford Cryostream cooling system using mirror-monochromated Cu-Kα radiation (λ = 1.54184 Å). Data was collected with *CrysAlisPro*[160] and the structures were solved with *SHELXT*[161] and *SHELXT*-2019[162] or *SHELXL*-2015.[163]

4.2.4 Calculations

Molecular docking calculations were performed by our collaborators with small sections of dsDNA with AutoDock 4.2[164] software. Gaussian09[165] was used to optimize the 3D structures of dyes **PyrN**, **OxN,** and **MeS**. The DNA was kept rigid during the docking, while the dyes were able to rotate around the flexible bonds. A more detailed explanation of this procedure can be found in Publication II. From these evaluations, the most energetically favorable conformations were chosen to be used in molecular dynamics (MD) simulations to gain insight on the turn-on type of fluorescence, which is widely accepted to arise from the rigidity of the dye molecule when bound with nucleic acids. The GROMACS 2020[166] and AMBER force[167] field were used for the docking calculations of the free dye and DNA-dye complexes. The fully-detailed description of the calculations can be found in Publication II.

5 RESULTS AND DISCUSSION

5.1 Aim of the work

The main goal of this work was to design and synthesize novel SYBR Green related cyanine dyes and study the structural characteristics, which changed the photophysical qualities of the dyes for better or worse. Understanding the structural key points could be a pathway to designing a specific dye for a desired application, such as selective RNA sensing. The increase in viral studies – as well as the desire to image biomolecules, for instance – has created a need for brighter and brighter probes. The gold nanocluster synthesis was a small part of the study, but we wanted to demonstrate that the non-covalent bound complex of AuNC and KU dye can act as a pH sensor. And since this complex works, by adding targeting ligands, drugs or adding another fluorescent probe, such as one of our cyanine dyes, we may have a multifunctional tool for new applications, such as advanced viral studies.

The following chapter will describe the main results of the original papers **I-IV** published by our group and coworkers. Articles **I, II** and **IV** focus on studying the monomethine cyanine dyes and their structure. By doing systematical alterations to the core structures, from as small as one heteroatom change to altering the aromatic systems and additional substituents, we studied the photophysical qualities related to these structural changes of SYBR Green related monomethine cyanine dyes. By doing so, we strived to find the key alterations that make the dyes brighter, have tighter binding, or show affinity towards a certain nucleic acid. The study from Paper **III** describes the synthesis of one of the gold nanoclusters included in the study and mechanism behind the pH sensing activity.

5.2 SYBR Green related cyanine dyes

5.2.1 Synthesis of cyanine dyes

The precursors for the cyanine dyes' synthesis were synthesized according to the published protocols. The quinoline synthesis was firstly followed by a patent of Ying.[168] Methylcarbostyril was mixed with 4-iodobenzene to allow the Ullman coupling (FIGURE 15) to happen between the two. Later on, the same synthesis route was used to synthesize the quinolines with substituents and the pyridine equivalent. The benzoxazolium used was synthesized from store-bought benzoxazole with amine methylation using methyl *p*-toluene sulfonate.[169] The same step was used to synthesize the thiazolium derivates without a benzene ring. Benzothiazolium was synthesized from 4-chloroaniline and potassium ethyl xanthate; after the initial reaction, sulfur was methylated with iodomethane, and the final step was *N*-methylation as described above.

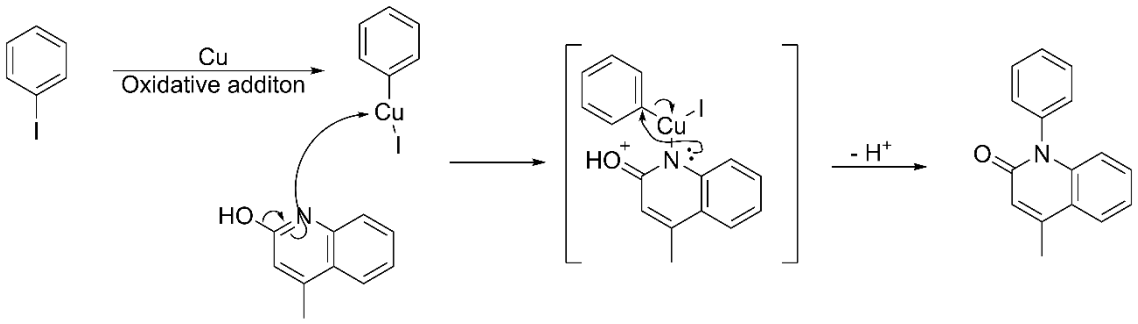

FIGURE 15. Ullman coupling reaction mechanism.[170]

With the precursors synthesized, the dye synthesis was done according to the classical method of combining two quaternary amine salts. The first step was to chlorinate the synthesized quinoline to form the amine salt. Then, the quinoline salt and either thizolium derivates or benzoxazolium were combined for the cyanine condensation reaction. This reaction yielded the chlorinated dye and either trace amounts of methanethiol dye or around 5% yield. Lastly, a substitution of the chloride with dimethylamine was performed. The same synthesis route was applied to all derivates with and without substituents (FIGURE 16). Yields of the synthesis varied from 3.1% to 35.1%.

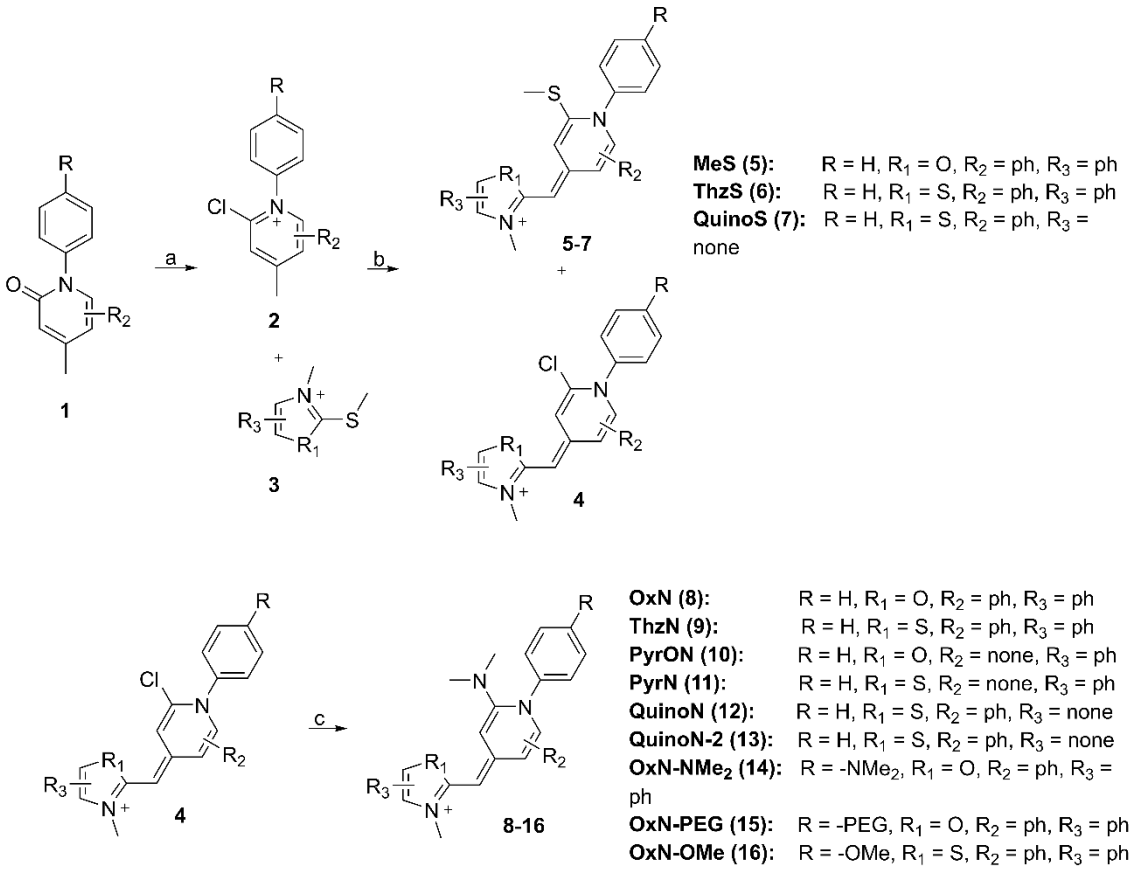

FIGURE 16. Synthesis route, which was used to synthesize all dyes covered in Articles I, II and IV, where a) is 1,2-DCE and $POCl_3$, b) is DCM and Et_3N and c) $HNMe_2$ and ACN.

The PEGylation of the phenol for the PEG dye was done according to the method by Nguyen *et al.*[171] Triethylene glycol monomethyl ether was used in this study and will be referred as PEG. First, the PEG needed to be tosylated so that the PEGylation of 4-iodophenol was possible. After PEGylation, the quinoline synthesis was performed as described above.

Even though the synthesis procedure was proven to be quite versatile, and we were able to synthesize over 10 novel dyes using the procedure, it did not work for all planned dyes. For Article IV, we had several other dyes planned, apart from dyes **14-16** (FIGURE 16), but their synthesis was not successful.

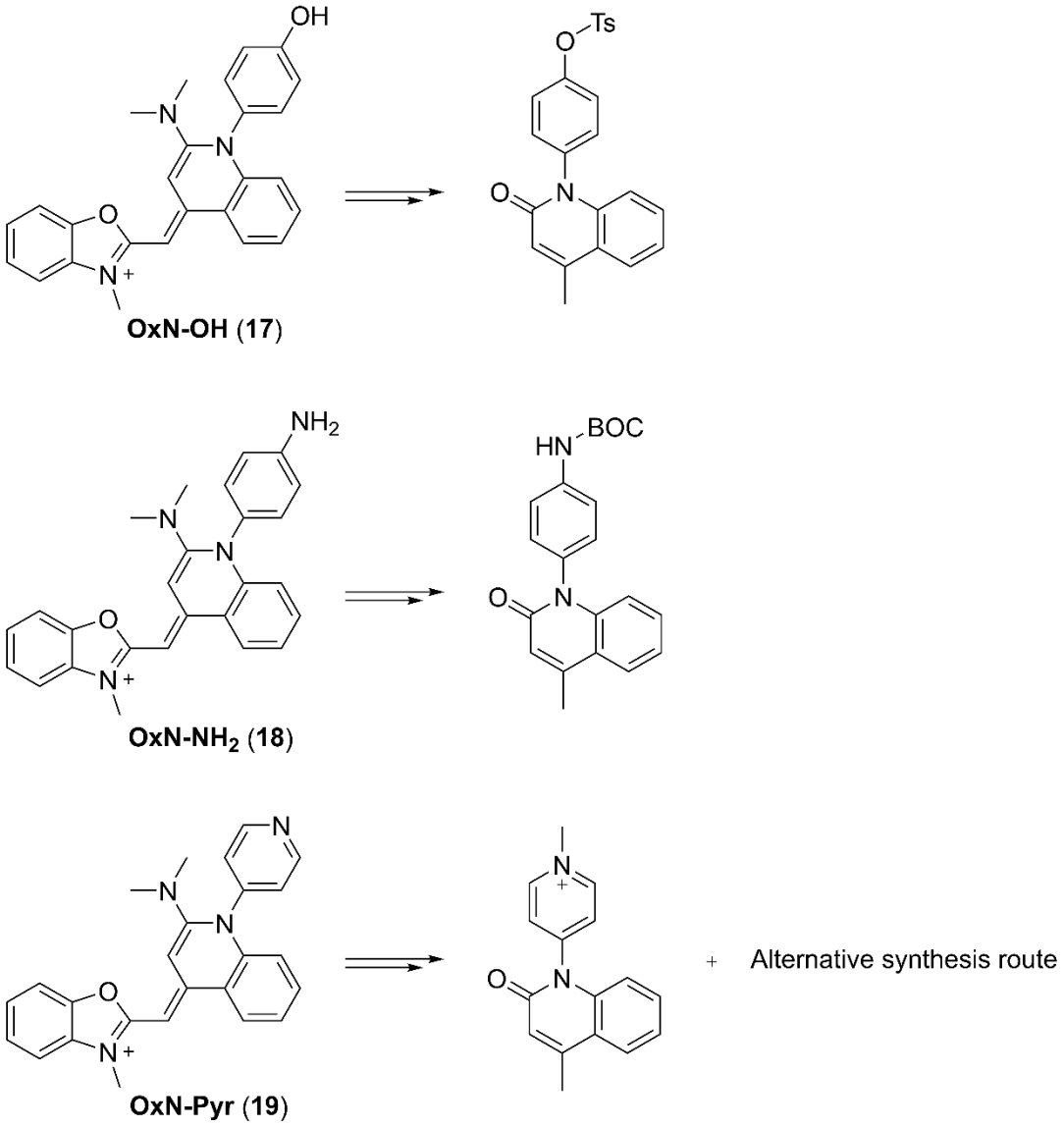

FIGURE 17. Structures of attempted cyanine dye derivates.

To synthesize the dyes presented in FIGURE 17, the general synthesis route was tried first. When the attempts failed, protecting groups were taken into to the synthesis. For both the tosylate and BOC, the protecting groups were added to the prepared quinoline intermediate. Since that did not seem to work, they were added as the first step of the synthesis when preparing the quinolines. Unfortunately, the synthesis still did not work and even with the protecting groups and several attempts, dyes **17** and **18** were not detected in MS studies, not even in trace amounts. For the pyridine dye **19,** it seemed reasonable to try protection with a methyl group since it would give the dye an additional charge, which had been previously proven to improve the quantum yield of monomethine dyes.[95] But the additional charge also prevented the synthesis, and no product was observed. The alternative synthesis route was tried as a last resort.

This protocol did not use $POCl_3$, which was suspected to cause the problems in the synthesis of these substituted dyes since it is reactive towards primary amines[172] and alcohols.[173] In this route, quinoline and the benzoxazolium were mixed in the first step. Adding DIPEA and trimethylsilyl trifluoromethyl sulfonate in inert conditions at 0 °C started the synthesis. After short refluxing at 40 °C, the mixture was cooled with ice and water was added dropwise. After extraction, the desired product should be collectable from the organic layer, but the synthesis did not work with the pyridine substituent.[174]

Growing the crystals and the single crystal X-ray diffraction (SCXRD) analysis were performed by our collaborators. From the start, obtaining suitable crystals was ruled to be quite hard. The amount of dyes available for this was very low, and at least in some cases, even with careful purification, impurities distracted the process. Therefore, an additional washing step was used. The water solution of $NaBH_4$ was used to perform the extraction step in hopes of purifying the sample and changing the counter ion from chloride to a bigger ion to help the crystal form. Although the ion exchange did not happen, it did purify the samples and some of the dyes formed crystals after this treatment. It did not work for all, however. Crystals were grown from a mixture of organic solvents via the slow evaporation method.

5.2.2 Molecular modeling

With the structural modifications and analyzing the photophysical data (below), the interaction between the dyes and DNA cannot be fully understood. The main forces of how the binding happens is not known from the steady state data. Hence, molecular modeling studies were conducted by our collaborators to gain more knowledge on the phenomena underlying the observable photophysics. Dyes with known X-ray crystal structures were chosen for this study due to their confirmed conformations. In the MD simulations, dyes are seen to explore the different regions of the DNA double helix, but the preferred binding site is the minor groove (FIGURE 18). This was a very interesting result since it was commonly accepted that the SYBR Green related dyes are intercalators.[25,28] However, our study showed no intercalation in any conditions. Furthermore, we were able to confirm that the great turn-on type of fluorescence arises from the rigidity of the dye molecule when bound with DNA. The main interactions with the dyes and the DNA were π-lone pair, π-sulfur bonds, and hydrogen bonding. These molecular modeling studies were extremely important, as we were able to better understand how the supramolecular relationship between the dyes and DNA happens and what kind of interactions are present. This enabled further studies with the intention to improve the binding properties to see if tighter

binding would enhance the rigidity of the dye, as well as the brightness of the complex.

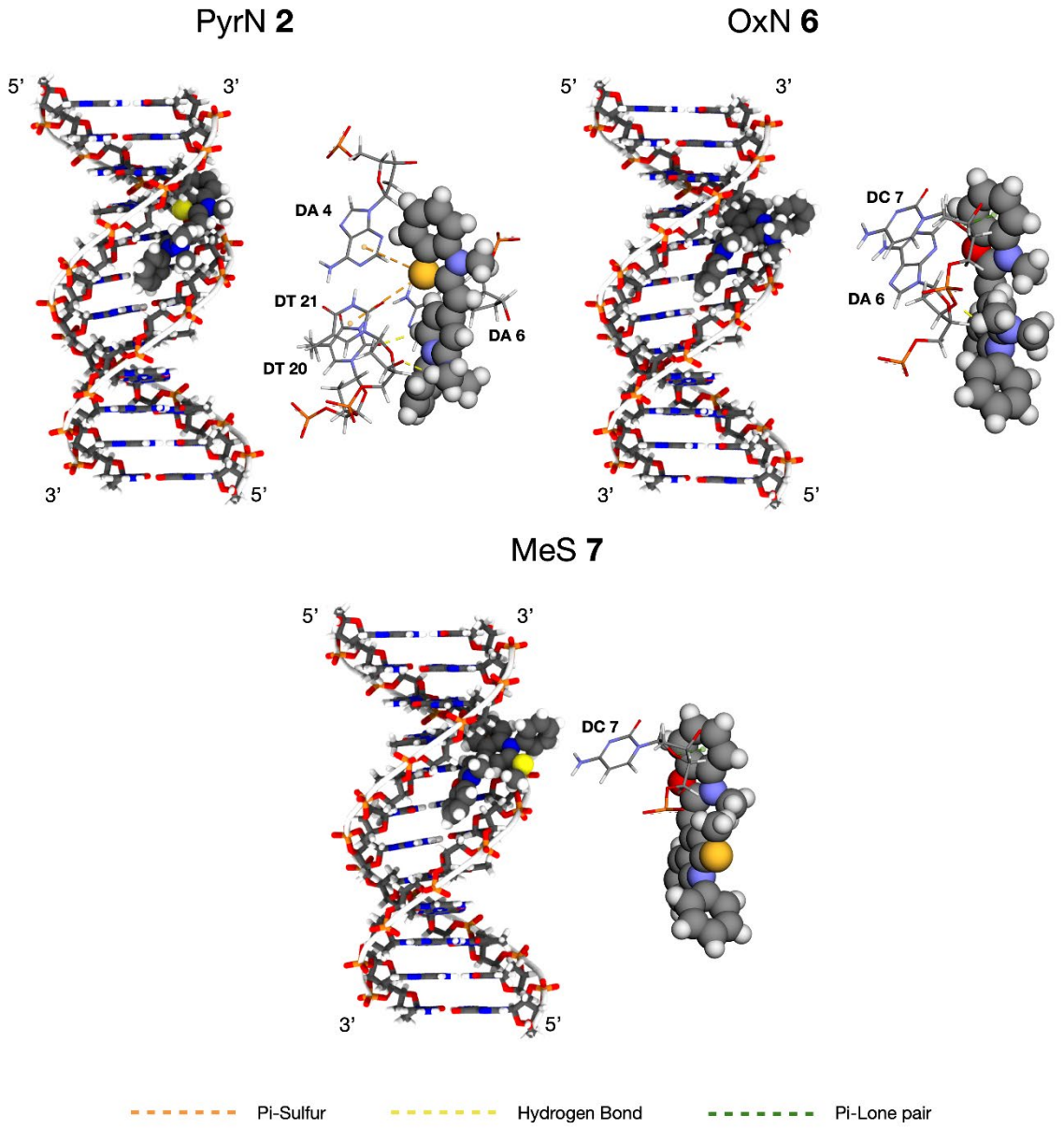

FIGURE 18. Molecular modeling studies showed the main weak interactions between the dyes and DNA in the minor groove. Reproduced from Article II with permission from Elsevier.

5.2.3 Fluorescence and Uv-Vis spectroscopy

To investigate the synthesized products and compare the structural changes in mind of the actual purpose of the dyes, a series of photophysical studies was conducted. To ease the comparison, the stock solutions of each dye were made with the same concentration, 19.6 mM in DMSO.

A series of titrations was performed for dyes in the UV-Vis setup. First, the stock was diluted in 1:1000 in either ethanol, TE buffer, or DNA in TE buffer solution, depending on which titration was to be performed. Usually, 2000 µl of the chosen

solvent (EtOH, TE buffer or DNA-TE buffer) was used as the blank, and then the concentration of the dye was gradually increased to obtain at least six data points. When measuring the fluorescence in DNA solutions, the concentration of DNA was kept constant and in high excess to ensure all dye molecules could bind the DNA. From this data, both the basic absorption spectra and molar absorptivities were plotted. Basic absorption plots were drawn directly from the data set, absorbance plotted against the wavelength or normalized by dividing all absorbance values with the maxima, respectively (FIGURE 19). To get the molar absorptivities, the absorption maxima of each six data points were plotted against the dye concentration of the relevant data point. From this, according to the Beer-Lambert law (1), the molar absorption coefficient can be extrapolated as the slope of the plot. This was conducted in the same manner for each solvent used to investigate the effect of solubility of the dyes.

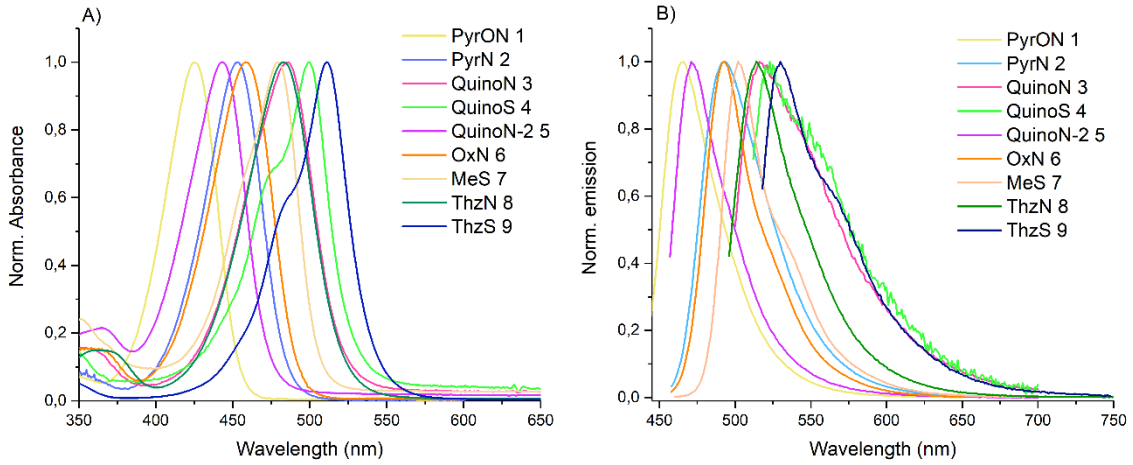

FIGURE 19. Example of normalized steady-state data from Article II, A) absorption and B) emission. Reproduced from Article II with permission from Elsevier.

Titrations were also performed with a fluorometer. Similar to the UV-vis titrations, one titration was made with 2000 µL high excess of the DNA solution and adding dye to this solution, gradually exciting the fluorescence emission with unique maxima for each dye and vice versa to measure the excitation. From this data, the basic spectra either normalized or with relative intensity was drawn. Plotting the emission intensity against the concentrations was done to ensure that the internal effects did not affect the emission intensity drastically when moving on to the following titrations. This data was also used in the Scatchard plot estimation (FIGURE 20b).

Next, to investigate the binding according to the McGhee von Hippel model[156] (functions (6) to (11)), DNA concentration was restricted to 0.52 µM and increasing the dye concentration gradually resulted in saturation points, where all the available DNA binding spaces are occupied with dye molecules. This data with the excess DNA data were used to draw the Scatchard plots according to

the model to gain estimates of the DNA binding site size and the binding affinity (FIGURE 20).

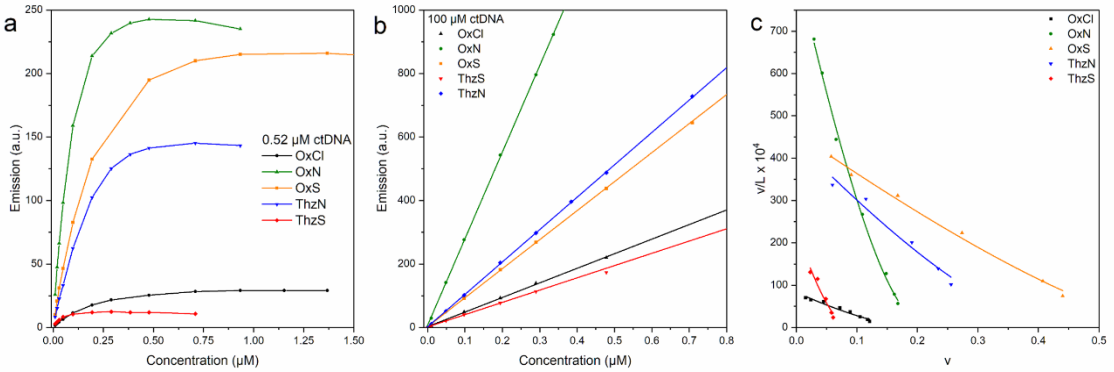

FIGURE 20. a) Emission of the dyes with limited DNA available for binding. b) Emission of the dyes with excess DNA. c) Example of Scatchard plots after processing the data from plots a) and b) according to the McGhee von Hippel model. Reproduced from Article I with permission from Royal Society of Chemistry.

Finally, to determine the quantum yields (QY), both the UV-Vis and fluorescence spectroscopy were combined. Again, titrations with excess DNA and increasing dye concentrations were performed, but this time, a specific excitation wavelength was used for both the sample and the standard (fluorescein) so that the values would be comparable. From the same sample, both absorbance and the emission were recorded. According to the functions (2) to (5), integrated emission was plotted against the absorbance at the excitation wavelength. The slopes of these plots were then used to calculate the quantum yields with the function (5). With the quantum yields and the molar absorption coefficients, brightness can be calculated. Brightness describes in a single number the ability of the dye to absorb and eventually emit the photons; hence, it can be used to compare the dyes with just one number.

Table 1. Photophysical data of the five best novel dyes and commercial dye SYBR Green I.

Dye	**OxN-OMe**	**OxN**	**PyrON**	**ThzN**	**OxN-PEG**	**SYBR Green I**
λ_{exc} (nm)	464	464	436	488	463	497
λ_{emi} (nm)	492	492	465	515	493	520
Stoke's Shift (nm)	28	28	29	27	30	23
ε_{max} (Ethanol) M^{-1} cm^{-1}	77900 ± 300	73600 ± 600	68410 ± 500	56900 ± 300	26900 ± 150	43 300
ε_{max} (ctDNA) M^{-1} cm^{-1}	49800 ± 500	47300 ± 200	36100 ± 740	36500 ± 300	20300 ± 200	29 500
Φ_f (%)	~100 %	~100 %	~100 %	68.1 %	~100 %	80 %[108]
Brightness (M^{-1} cm^{-1})	**49800**	**47300**	**36100**	**24900**	**20300**	**23600**

With all this data, from over 10 novel monomethine cyanine dyes, some trends could be seen. Firstly, the heteroatoms play a key role when it comes to the photophysical qualities of these dyes. We systematically studied the chromophores of SYBR Green I and II. One main difference in the chromophores is that SYBR green I has benzoxazolium moiety and SYBR Green II has benzothiazolium moiety, respectively. The only difference in these two are the change from oxygen (benzoxazolium) to sulfur (benzothiazolium) (FIGURE 21). Our dyes also had shorter versions of the so-called arms from the SYBR dyes, dimethylamine from SYBR Green I and methanethiol from the SYBR Green II. Combining these, we designed four new dyes[I], which we could compare with as small as one heteroatom change. Oxygen compared to sulfur, (oxazolium vs. thiazolium), gave a much better response with DNA in terms of the emission intensity and binding properties. Oxygen in this position enhanced the photophysical qualities drastically, as seen in Table 1, **OxN** compared to **ThzN**. Changing sulfur (**ThzN**) to oxygen (**OxN**) greatly improved the quantum yield and therefore the overall brightness of the dye. Similarly in the arm position in the quinoline moiety, nitrogen was a better option than sulfur, respectively.

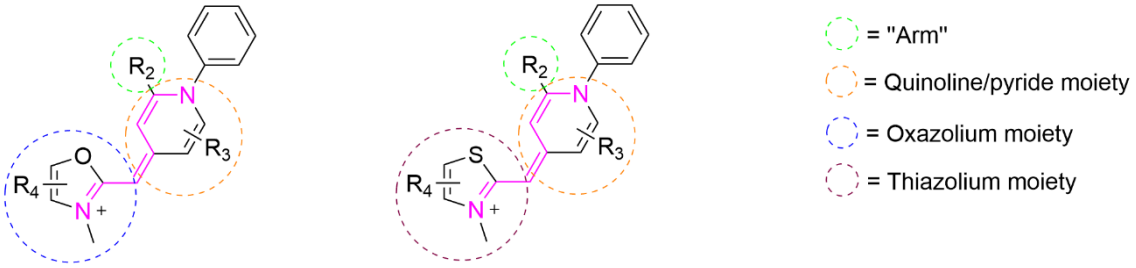

FIGURE 21. General structure of the dyes with different moieties highlighted. Reproduced from Article II with kind permission from Elsevier.

In our next study, we changed the size of the chromophore to see if smaller dyes would have tighter binding since they would need smaller spaces in already tight binding sites of DNA. Thiazolium derivates without the phenyl ring (dyes **QuinoS**, **QuinoN** and **QuinoN-2**) and dyes with pyridine moiety instead of quinoline (dyes **PyrON** and **PyrN**) were designed and synthesized. We were able to further confirm that the benzoxazolium enhances the photophysical qualities, such as quantum yield and with that the emission intensity, compared to the thiazolium derivates. In fact, removing the phenyl ring from the thiazolium moiety almost completely shut down the emission intensity. Removing the benzene ring from the quinoline moiety also lowered the intensities, but not as drastically. For the pyridine derivates, the quantum yields and brightnesses were still high, making these dyes suitable for further studies.

After the MD simulations, the goal was to improve the binding properties of the dyes, as well as the water solubility of the dyes. The water solubility aspect was found to be important since previously,[I,II] it had been shown that the dyes give the highest molar abosrptivities in organic solvents, whereas in water solutions, a significant drop is seen. This hints that some aggregation or

participation may happen, preventing the full potential of the dye usage. Aggregation is a well-known phenomena with cyanine dyes, and it can cause spectral shifts and fluorescence quenching. With ionic dyes, the aggregation can happen due to the hydroscopic interactions.[175] Since the main interactions with the dyes and DNA were determined to be hydrogen bonding and π-lone pair bonds, reaching these two goals simultaneously seemed like an intriguing goal. However, the enhancement of water solubility was not observed, but additional oxygen containing groups, methoxy and PEG, did enhance the binding properties. Tighter binding did not automatically mean higher brightness. The **OxN-PEG** had significantly tighter binding affinity compared to every other dye, but it did not have the greatest brightness even though the additional functional group did not alter the quantum yield at all. The short methoxy also improved the binding affinity along with absorption, and since it was able to absorb light more efficiently, it is also the brightest of our dyes thus far. Including new substituents in the terminal phenyl group does not work with all substituents. While the oxygen containing groups performed well throughout the study, amine (**OxN-NMe$_2$**) in this position shut down the emission almost completely even when the molar abosrptivities were at an all-time high for our dyes. Lastly, we also wanted to study the RNA activity of the dyes.

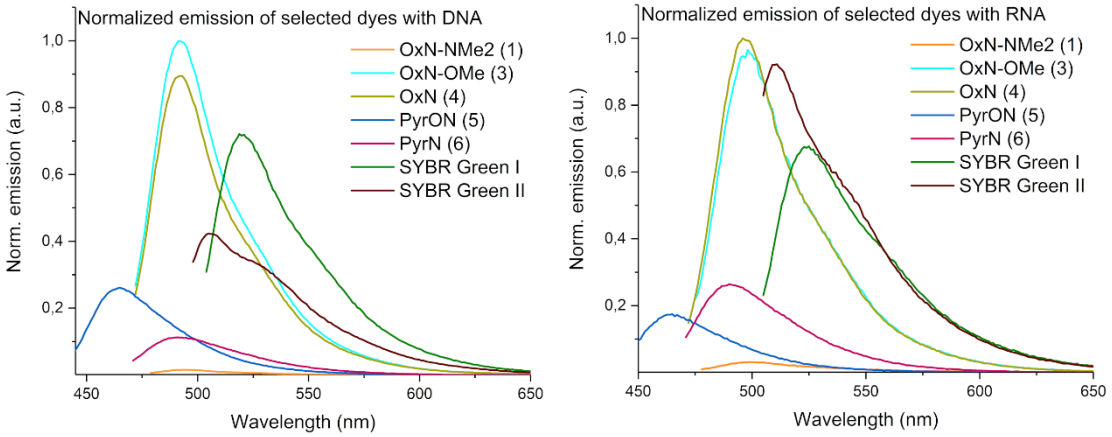

FIGURE 22. Normalized emissions of selected dyes with DNA and RNA. Normalization has been done for all dyes with the emission of the dye with the highest intensity (**OxN-OMe** with DNA and **OxN** with RNA, respectively) to investigate if any trends can be observed. Reproduced from Article IV.

Similar to studies with DNA, our two best dyes, **OxN** and **OxN-OMe,** performed the best with RNA as well. **OxN-OMe** shows a bit higher intensity with DNA compared to **OxN**, as the brightness studies suggested. **OxN** has a bit higher intensity with RNA, respectively. Both these novel dyes outperform the commercial dyes, SYBR Green I and II, with both DNA and RNA. SYBR Green II exhibits great affinity towards RNA and the intensity with RNA is almost as high as our dyes. Also, the same thiazolium moiety containing the novel dye **PyrN**, shows higher intensity with RNA compared to DNA. Meanwhile, the same dye but with oxazolium moiety, **PyrON** (change from sulfur to oxygen), shows

higher intensity with DNA. This clearly shows how small changes can shift the behavior of the dyes completely. This result also indicates that it could be possible to identify the RNA-specific sites in the dyes with long-term structural studies. Here, dyes with sulfur in their structures show affinity towards RNA. A similar notion was made by Lu *et al.*,[113] who reported a RNA-specific monomethine dye with thiazolium moiety and an additional styryl group that also contained sulfur.

5.3 Range adjustable pH sensing with gold nanoclusters

In this study,[III] we investigated, together with our collaborators, the complex of fluorescent dyes and different-sized gold nanoclusters and how the pH alters the fluorescence of it. I prepared the $Au_{102}(P\text{-}MBA)_{44}$ cluster for the study. It is an ongoing study to make a complex of a gold nanocluster and cyanine dye to be used in virus studies; hence, this research provided great background knowledge regarding the behavior of gold nanoclusters with a fluorescent probe.

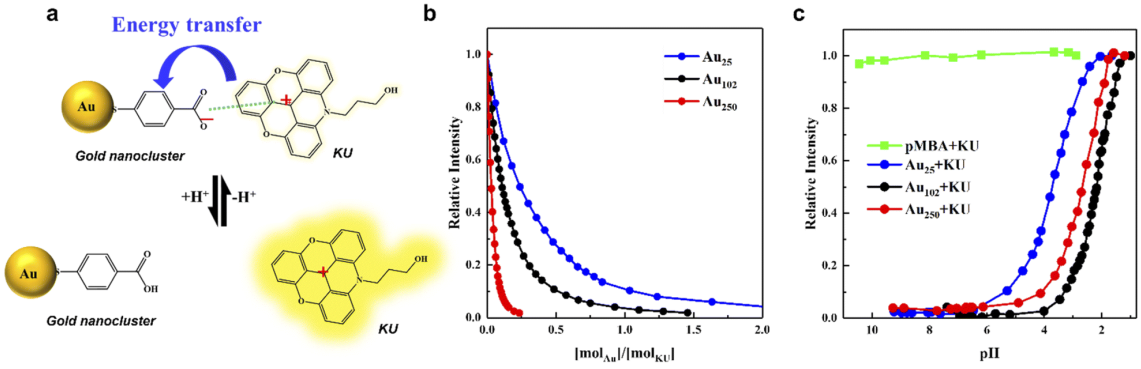

FIGURE 23. a) Illustration of the electrostatic interaction between the gold nanocluster and the KU dye in a different pH. b) Relative intensity of the emission in pH 10 against the molar ratio of Au to KU. c) Relative intensity of the emission of the complex as the function of pH in molar ratio Au/Ku = 2. Reproduced from Article III with kind permission from Royal Society of Chemistry.

The gold nanoclusters and KU dye form a complex through electrostatic interactions (FIGURE 23a.). When the pH changes, this interaction also changes since the gold nanocluster can protonate and lose the negative charge, subsequently breaking the complex and enhancing the emission intensity when KU dye is freed from the complex.

5.3.1 Synthesis of gold nanoclusters

$Au_{102}(p\text{-}MBA)_{44}$ was synthesized with the modified Brust-Schiffrin[72] method as previously described.[176,177] Water solutions of Gold (III) chloride and *p*-MBA were prepared with Elga water, and a small amount of 10 mM NaOH was added to the p-MBA solution. Water, methanol, and some of the water solutions

prepared were added to a plastic bottle. This solution was mixed at room temperature for exactly 20 hours. Then $NaBH_4$ was added, and the mixture was stirred for an additional five hours. Methanol was added until the volume of the mixture was 800 ml. To this solution, a 5 M NH_4OAc-solution was added, and the mixture was stirred vigorously. For the work-up, the resulting mixture was divided into 50 mL centrifuge tubes and the tubes were centrifuged at 3500 rpm for five minutes. The solution was decanted, and the resulting participates were allowed to dry in air. Each participate was dissolved in a small amount of Elga water and combined to four tubes. For each tube, a 5 M NH_4OAc solution was added, following the addition of methanol until the volume reached 45 mL, and these tubes were again centrifuged at 3500 rpm for 10 minutes. The solution was decanted and participates were allowed to dry. The participates were dissolved in a small amount of Elga water and combined. To this solution, some 5 M NH_4OAc was added, following the addition of methanol. The resulting mixture was centrifuged at 3500 rpm for 12 minutes. The solution was decanted to a new tube, and methanol was added until the volume reached 45 mL. The tube was centrifuged at 3500 rpm for 15 minutes. The solution was discarded, and the resulting black solid was allowed to air dry.

The purity of the product was evaluated with polyacrylamide gel electrophoresis (PAGE) by comparing a known sample of Au_{102} to the synthesized clusters. To further confirm that the product was $Au_{102}(p\text{-MBA})_{44}$, the absorption spectra of the sample was compared to a known spectrum of Au_{102} gold nanocluster.

The synthesis also had an additional purification step of the *p*-MBA with column chromatography, using 10% MeOH/DCM as an eluent due to the purchased starting material being only 90% pure and the synthesis did not work with the impurities. This highlights the difficulty of the gold nanocluster synthesis – the procedure may seem simple, but if it is not followed exactly, it will not produce atomically precise gold nanoclusters. Hence, the mixing times, purity, pH and the ratio of the materials are crucial to acknowledge in the procedures. Improved and further developed fractional precipitation was used to purify the gold compounds.[176,177]

6 CONCLUSIONS

The background of this study originated from the collaboration that aimed to produce fluorescent probes capable of detecting viral RNA when the virus releases the RNA to an infected cell. For this reason, the brightness of the dye molecules was a key interest throughout the research since the amount of the viral RNA among other nucleic acid materials in the system is relatively low. Also, for that reason, the interest towards RNA specificity grew towards the end of the study presented here. Commercial dyes targeted for RNA, such as SYBR Green II and SYTO RNAselect, are not fully selective towards RNA and their sensitivity in complex studies can be an issue. However, it is not only RNA selectivity we were interested in. Selectivity towards either DNA or RNA would be a breakthrough in the field. To gain knowledge of how the dyes interact with the nucleic acids and how it changes the photophysical qualities, studies with double stranded DNA were mostly used to get comparable results. These studies could then help to pinpoint the important factors to be considered when trying to design the selective probe. Hence, more studies regarding the RNA selectivity of monomethine cyanine dyes are still needed.

A comprehensive study of the structural characteristics of the SYBR Green related monomethine cyanine dyes were conducted. Several variations to the structures of basic cores were made, as little as one heteroatom change, to removing whole aromatic rings. We noted that changing the heteroatom at the thiazolium moiety from sulfur to oxygen (oxazolium) had the most drastic effect on the brightness with DNA. Oxygen in this position enhanced not only the brightness, but also the quantum yield and the binding properties of the dye. Also, changing the so-called arm from methylthiol to dimethyl amine, from sulfur to nitrogen, had the same effect.

To continue, we were interested to see if the size of the molecule had any effect on the photophysical qualities. Hence, we made the dyes smaller by removing the phenyl ring from the thiazolium moiety or the quinoline moiety. Again, similar trends with the heteroatoms were observed with the smaller dyes. Interestingly, removing the phenyl ring from the quinoline moiety did not alter the photophysical qualities as drastically as removing it from the thiazolium

moiety. The pyridine dyes performed still quite well, even though the brightness lowered a bit. The dyes without a phenyl ring at the thiazolium moiety were almost completely shut down. The quantum yields of these dyes were below 10% and the intensities were barely detectable even in high concentrations. During this study, the molecular modeling also suggested that our dyes bind with the minor groove of the DNA with hydrogen bonds, π-lone pair bonds, and π-sulfur bonds. It was also evident in the calculations that the rigidity of the molecule plays a crucial role in the brightness of the probe.

From the previous results, we modified the terminal phenyl group aiming to improve the water solubility and the binding rigidity of the dyes. Also, in this study, one heteroatom change was capable of completely shutting down the fluorescence of the probe. Simply changing the methoxy group to dimethylamine at the terminal phenyl group led to almost completely shutting down the emission of the dyes. While both groups enhanced the absorption, only the methoxy group also enhanced the emission. Even with the additional possible water solubility enhancing groups, including PEG, no evidence regarding the improvement of the water solubility was seen. The additional methoxy or PEG did enhance the binding affinity towards DNA.

Lastly, the study of combining a commercial dye with gold nanoclusters to the pH of the probe is an important new aspect to consider, as we are moving towards multifunctional probes. This study also gave great background on the characteristics of the gold nanocluster synthesis and how challenging it can be. In this study, the fluorescence of the dye and cluster complex changes according to the pH of the solution. The complex is formed by the electrostatic interactions of negatively-charged gold nanoclusters and positively-charged KU dye. The fluorescence of the dye is quenched when the complex is intact, but changing the pH releases the dye from the gold nanocluster surface, enabling the fluorescence to occur. Combining the gold nanocluster with cyanine dye is also something to consider in the future after the promising results of the pH active complex.

To summarize, a diligent study regarding the structural alteration of monomethine cyanine dyes and the effect of these changes to the photophysical and binding properties of these dyes with nucleic acids was conducted. New information about the important aspects within the dyes around the fixed core was gained. In the future, this information could be used in further developments of SYBR Green related monomethine cyanine dyes, and perhaps for other types of fluorescent probes to answer the new arising challenges and provide more advantageous probes. Investigating the gold nanocluster and fluorescent dye complex gave valuable insight about the possibilities that these new fluorescent probe complexes possess. Bringing together gold nanoclusters and cyanine dyes and or other ligands could provide completely new multifunctional tools to be used in biological applications.

REFERENCES

1. Ardila-Leal, L. D., Poutou-Piñales, R. A., Pedroza-Rodríguez, A. M. & Quevedo-Hidalgo, B. E. A brief history of colour, the environmental impact of synthetic dyes and removal by using laccases. *Molecules* **26**, (2021).
2. Christie, R. M. *Colour Chemistry*. (The Royal Society of Chemistry, Cambridge, 2015).
3. Shindy, H. A. Fundamentals in the chemistry of cyanine dyes: A review. *Dyes and Pigments* **145**, 505–513 (2017).
4. Bernstein, P. L. *The Power of Gold: The History of an Obsession*. (John Wiley & Sons, 2012).
5. Hammer, B. & Norskov, J. K. Why gold is the noblest of all the metals. *Nature* **376**, 238–240 (1995).
6. Fricker, S. P. Medical Uses of Gold Compounds: Past, Present and Future. *Gold Bull* **29**, 53–60 (1996).
7. Corti, C. W. & Holliday, R. J. Commercial Aspects of Gold Applications: From Materials Science to Chemical Science. *Gold Bull* **37**, 20–26 (2004).
8. Carreón-Valencia, T. *et al. IARC Monographs on the Evaluation of Carcinogenic Risks to Humans. Volume 99: Some Aromatic Amines, Organic Dyes, and Related Exposures*. (2010).
9. Ilina, K. & Henary, M. Cyanine Dyes Containing Quinoline Moieties: History, Synthesis, Optical Properties, and Applications. *Chemistry - A European Journal* **27**, 4230–4248 (2021).
10. Williams, G. XXVI. -Reseaches on Chinoline and its Homologues. *Transactions of the Royal Society of Edinburgh* **21**, 377–401 (1857).
11. Armitage, B. A. Cyanine dye-DNA interactions: Intercalation, groove binding, and aggregation. *Top Curr Chem* **253**, 55–76 (2005).
12. Armitage, B. A. Cyanine Dye–Nucleic Acid Interactions. in *Topics in Heterocyclic Chemistry* vol. 14 11–29 (2008).
13. Henary, M. & Levitz, A. Synthesis and applications of unsymmetrical carbocyanine dyes. *Dyes and Pigments* **99**, 1107–1116 (2013).
14. Du, Y., Liu, X. & Zhu, S. Near-Infrared-II Cyanine/Polymethine Dyes, Current State and Perspective. *Front Chem* **9**, (2021).
15. Shershov, V. E. *et al.* Near-infrared heptamethine cyanine dyes. Synthesis, spectroscopic characterization, thermal properties and photostability. *Dyes and Pigments* **97**, 353–360 (2013).
16. Samanta, A., Vendrell, M., Das, R. & Chang, Y. T. Development of photostable near-infrared cyanine dyes. *Chemical Communications* **46**, 7406–7408 (2010).
17. Mujumdar, R. B., Ernst, L. A., Mujumdar, S. R., Lewis, C. J. & Waggoner, A. S. Cyanine Dye Labeling Reagents: Sulfoindocyanine Succinimidyl Esters. *Bioconjug Chem* **4**, 105–111 (1993).
18. Invitrogen. Nucleic Acid Detection and Analysis. in *Molecular Probes ™ Handbook* 307–324 (Thermo Fisher Scientific, 2010).

19. Nucleic Acid Detection and Analysis. in *Molecular Probes ™ Handbook - A Guide to Fluorescent Probes and Labeling Technologies* vol. 11 (2010).
20. Noble, R. T. & Fuhrman, J. A. Use of SYBR Green I for rapid epifluorescence counts of marine viruses and bacteria. *Aquatic Microbial Ecology* **14**, 113–118 (1998).
21. Marie, D., Partensky, F., Jacquet, S. & Vaulot, D. Enumeration and Cell Cycle Analysis of Natural Populations of Marine Picoplankton by Flow Cytometry Using the Nucleic Acid Stain SYBR Green I. *Appl Environ Microbiol* **63**, 186–193 (1997).
22. Marinowic, D. R. *et al.* A new SYBR Green real-time PCR to detect SARS-CoV-2. *Sci Rep* **11**, (2021).
23. Karlsen, F., Steen, H. B. & Nesland, J. M. SYBR Green I DNA staining increases the detection sensitivity of viruses by polymerase chain reaction. *Journal of ViroIogicaI Methods* **55**, 153–156 (1995).
24. Kirsanov, K. I., Lesovaya, E. A., Yakubovskaya, M. G. & Belitsky, G. A. SYBR Gold and SYBR Green II are not mutagenic in the Ames test. *Mutat Res Genet Toxicol Environ Mutagen* **699**, 1–4 (2010).
25. Dragan, A. I. *et al.* SYBR Green I: Fluorescence properties and interaction with DNA. *J Fluoresc* **22**, 1189–1199 (2012).
26. Saarnio, V. K. *et al.* Development of functionalized SYBR green II related cyanine dyes for viral RNA detection. *Dyes and Pigments* **177**, 108282 (2020).
27. Evenson, W. E., Boden, L. M., Muzikar, K. A. & Oleary, D. J. 1H and 13C NMR assignments for the cyanine dyes SYBR safe and thiazole orange. *Journal of Organic Chemistry* **77**, 10967–10971 (2012).
28. Dragan, A. I. *et al.* Characterization of PicoGreen Interaction with dsDNA and the Origin of Its Fluorescence Enhancement upon Binding. *Biophys J* **99**, 3010–3019 (2010).
29. Kolbeck, P. J. *et al.* Molecular structure, DNA binding mode, photophysical properties and recommendations for use of SYBR Gold. *Nucleic Acids Res* **49**, 5143–5158 (2021).
30. Lee, L. G., Chen, C. -H & Chiu, L. A. Thiazole orange: A new dye for reticulocyte analysis. *Cytometry* **7**, 508–517 (1986).
31. Glazer, A. N. & Rye, H. S. Stable dye-DNA intercalation complexes as reagents for high-sensitivity fluorescence detection. *Nature* **359**, 859–861 (1992).
32. Rye, H. S. *et al.* Stable fluorescent complexes of double-stranded DNA with bis-intercalating asymmetric cyanine dyes: Properties and applications. *Nucleic Acids Res* **20**, 2803–2812 (1992).
33. Kiltie, A. E. & Ryan, A. J. SYBR Green I staining of pulsed field agarose gels is a sensitive and inexpensive way of quantitating DNA double-strand breaks in mammalian cells. *Nucleic Acids Res* **25**, 2945–2946 (1997).
34. Tuma, R. S. *et al.* Characterization of SYBR Gold Nucleic Acid Gel Stain: A Dye Optimized for Use with 300-nm Ultraviolet Transilluminators. *Anal Biochem* **268**, 278–288 (1999).

35. Hirons, G. T., Fawcett, J. J. & Crissman, H. A. TOTO and YOYO: New very bright fluorochromes for DNA content analyses by flow cytometry. *Cytometry* **15**, 129–140 (1994).
36. Guindulain, T., Comas, J. & Vives-Rego, J. Use of Nucleic Acid Dyes SYTO-13, TOTO-1, and YOYO-1 in the Study of Escherichia coli and Marine Prokaryotic Populations by Flow Cytometry. *Appl Environ Microbiol* **63**, 4608–4611 (1997).
37. Ernst, L. A., Gupta, R. K., Mujumdar, R. B. & Waggoner, A. S. Cyanine dye labeling reagents for sulfhydryl groups. *Cytometry* **10**, 3–10 (1989).
38. Lumiprobe. Cyanine dyes. https://www.lumiprobe.com/tech/cyanine-dyes.
39. Kundu, K. *et al.* Hydrocyanines: A class of fluorescent sensors that can image reactive oxygen species in cell culture, tissue, and in vivo. *Angewandte Chemie - International Edition* **48**, 299–303 (2009).
40. Gorka, A. P., Nani, R. R. & Schnermann, M. J. Harnessing Cyanine Reactivity for Optical Imaging and Drug Delivery. *Acc Chem Res* **51**, 3226–3235 (2018).
41. Altman, R. B. *et al.* Cyanine fluorophore derivatives with enhanced photostability. *Nat Methods* **9**, 68–71 (2012).
42. Dereje, D. M., Pontremoli, C., Moran Plata, M. J., Visentin, S. & Barbero, N. Polymethine dyes for PDT: recent advances and perspectives to drive future applications. *Photochemical and Photobiological Sciences* **21**, 397–419 (2022).
43. Mojzych, M. & Henary, M. Synthesis of Cyanine Dyes. in *Heterocyclic Polymethine Dyes* 1–9 (Springer Berlin Heidelberg, 2008). doi:10.1007/7081_2008_119.
44. Dar, N. & Ankari, R. Theoretical Models, Preparation, Characterization and Applications of Cyanine J-Aggregates: A Minireview. *ChemistryOpen* **11**, (2022).
45. Klán, P. & Wirz, J. *Photochemistry of Organic Compounds: From Concepts to Practice*. (Wiley, 2009).
46. Gomes, A. J., Lunardi, C. N., Rocha, F. S. & Patience, G. S. Experimental methods in chemical engineering: Fluorescence emission spectroscopy. *Canadian Journal of Chemical Engineering* vol. 97 2168–2175 Preprint at https://doi.org/10.1002/cjce.23506 (2019).
47. chromophore. in *The IUPAC Compendium of Chemical Terminology* vol. 3rd (International Union of Pure and Applied Chemistry (IUPAC), 2006).
48. Turro, N. J., Ramamurthy, V. & Scaiano, J. C. *Principles of Molecular Photochemistry*. (University Science Books, 2009).
49. Zhang, Y., Xu, X. & Yan, B. A multicolor-switchable fluorescent lanthanide MOFs triggered by anti-cancer drugs: multifunctional platform for anti-cancer drug sensing and information anticounterfeiting. *J Mater Chem C Mater* **10**, 3576–3584 (2022).

50. Wang, L., Frei, M. S., Salim, A. & Johnsson, K. Small-Molecule Fluorescent Probes for Live-Cell Super-Resolution Microscopy. *J Am Chem Soc* **141**, 2770–2781 (2019).
51. Sato, Y., Igarashi, Y., Suzuki, M., Higuchi, K. & Nishizawa, S. Deep-red fluorogenic cyanine dyes carrying an amino group-terminated side chain for improved RNA detection and nucleolar RNA imaging. *RSC Adv* **11**, 35436–35439 (2021).
52. He, M., Sato, Y. & Nishizawa, S. Classical thiazole orange and its regioisomer as fluorogenic probes for nucleolar RNA imaging in living cells. *Analyst* **148**, 636–642 (2022).
53. Hess, S. T., Gould, T. J., Gunewardene, M., Bewersdorf, J. & Mason, M. D. Ultrahigh resolution imaging of biomolecules by fluorescence photoactivation localization microscopy. *Methods Mol Biol* **544**, 483–522 (2009).
54. Lord, S. J., Lee, H. L. D. & Moerner, W. E. Single-molecule spectroscopy and imaging of biomolecules in living cells. *Anal Chem* **82**, 2192–2203 (2010).
55. Vázquez, M. E., Blanco, J. B. & Imperiali, B. Photophysics and biological applications of the environment-sensitive fluorophore 6-N,N-dimethylamino-2,3-naphthalimide. *J Am Chem Soc* **127**, 1300–1306 (2005).
56. Yu, M. & Zheng, J. Clearance Pathways and Tumor Targeting of Imaging Nanoparticles. *ACS Nano* **9**, 6655–6674 (2015).
57. Chapman, S. *et al.* Nanoparticles for cancer imaging: The good, the bad, and the promise. *Nano Today* **8**, 454–460 (2013).
58. Chen, L. Y., Wang, C. W., Yuan, Z. & Chang, H. T. Fluorescent gold nanoclusters: Recent advances in sensing and imaging. *Anal Chem* **87**, 216–229 (2015).
59. van de Looij, S. M. *et al.* Gold Nanoclusters: Imaging, Therapy, and Theranostic Roles in Biomedical Applications. *Bioconjug Chem* **33**, 4–23 (2022).
60. Lippé, R. Flow Virometry: a Powerful Tool To Functionally Characterize Viruses. *J Virol* **92**, (2018).
61. Liu, P. *et al.* Concurrent photothermal therapy and photodynamic therapy for cutaneous squamous cell carcinoma by gold nanoclusters under a single NIR laser irradiation. *J Mater Chem B* **7**, 6924–6933 (2019).
62. Dou, W. T. *et al.* Fluorescent probes for the detection of disease-associated biomarkers. *Sci Bull (Beijing)* **67**, 853–878 (2022).
63. Albers, A. E., Okreglak, V. S. & Chang, C. J. A FRET-based approach to ratiometric fluorescence detection of hydrogen peroxide. *J Am Chem Soc* **128**, 9640–9641 (2006).
64. Watanabe, H., Ono, M., Ariyoshi, T., Katayanagi, R. & Saji, H. Novel Benzothiazole Derivatives as Fluorescent Probes for Detection of β-Amyloid and α-Synuclein Aggregates. *ACS Chem Neurosci* **8**, 1656–1662 (2017).
65. Jin, R. Atomically precise metal nanoclusters: Stable sizes and optical properties. *Nanoscale* **7**, 1549–1565 (2015).

66. Lee, B. K., Yun, Y. H. & Park, K. Smart nanoparticles for drug delivery: Boundaries and opportunities. *Chem Eng Sci* **125**, 158–164 (2015).
67. Jin, R., Zeng, C., Zhou, M. & Chen, Y. Atomically Precise Colloidal Metal Nanoclusters and Nanoparticles: Fundamentals and Opportunities. *Chem Rev* **116**, 10346–10413 (2016).
68. Liu, L. & Corma, A. Metal Catalysts for Heterogeneous Catalysis: From Single Atoms to Nanoclusters and Nanoparticles. *Chem Rev* **118**, 4981–5079 (2018).
69. Chakraborty, I. & Pradeep, T. Atomically Precise Clusters of Noble Metals: Emerging Link between Atoms and Nanoparticles. *Chem Rev* **117**, 8208–8271 (2017).
70. Schmid, G. *et al.* Au55[P(C6H5)3]12Cl6 - ein Goldcluster ungewöhnlicher Gröfie. *Chem. Ber.* **114**, 3634–3642 (1981).
71. Brust, M., Fink, J., Bethella, D., Schiffrina, D. J. & Kielyb, C. Synthesis and Reactions of Functionalised Gold Nanoparticles. *J. Chem. Soc., Chem. Commun.* 1655–1656 (1995).
72. Brust, M., Walker, M., Bethell, D., Schiffrin, D. J. & Whyman, R. Synthesis of Thiol-derivatised Gold Nanoparticles in a Two-phase Liquid-Liquid System. *J. Chem. Soc., Chem. Commun.* **0**, 801–802 (1994).
73. Whetten, R. L. *et al.* Nanocrystal gold molecules. *Advanced Materials* **8**, 428–433 (1996).
74. Faraday, M. Experimental Relations of Gold (and other Metals) to Light. *Philos Trans R Soc Lond* **147**, 145–181 (1857).
75. Turkevich, J., Stevenson, P. C. & Hillier, J. A Study of the Nucleation and Growth Processes in the Synthesis of Colloidal Gold. *Discuss Faraday Soc* **11**, 55–75 (1951).
76. Frens, G. Controlled Nucleation for the Regulation of the Particle Size in Monodisperse Gold Suspensions. *Nature Physical Science* **241**, 20–22 (1973).
77. Polte, J. *et al.* Mechanism of gold nanoparticle formation in the classical citrate synthesis method derived from coupled in situ XANES and SAXS evaluation. *J Am Chem Soc* **132**, 1296–1301 (2010).
78. Dreaden, E. C., Alkilany, A. M., Huang, X., Murphy, C. J. & El-Sayed, M. A. The golden age: Gold nanoparticles for biomedicine. *Chem Soc Rev* **41**, 2740–2779 (2012).
79. Zhang, L. & Wang, E. Metal nanoclusters: New fluorescent probes for sensors and bioimaging. *Nano Today* **9**, 132–157 (2014).
80. Zhao, P., Li, N. & Astruc, D. State of the art in gold nanoparticle synthesis. *Coord Chem Rev* **257**, 638–665 (2013).
81. Deligeorgiev, T. G., Zaneva, D. A., Hong Kim, S. & Sabnis, R. W. Preparation of Monomethine Cyanine Dyes for Nucleic Acid Detection. *Dyes and Pigments* **37**, 205–211 (1998).
82. Fu, Y. Le *et al.* Monomethine cyanine dyes with an indole nucleus: Microwave-assisted solvent-free synthesis, spectral properties and theoretical studies. *Dyes and Pigments* **82**, 409–415 (2009).

83. Haugland, R. P., Yue, S. T., Millard, P. J. & Roth, B. L. Cyclic-substituted Unsymmetrical Cyanine Dyes. (1995).
84. Yue, S. T. *et al.* Substituted Unsymmetrical Cyanine Dyes With Selected Permeability. vol. 890 (1997).
85. Deligeorgiev, T. G., Zaneva, D. A., Katerinopoulos, H. E. & Kolev, V. N. A novel method for the preparation of monomethine cyanine dyes. *Dyes and Pigments* **41**, 49–54 (1999).
86. Deligeorgiev, T. G., Gadjev, N. I., Drexhage, K.-H. & Sabnis, R. W. Preparation of Intercalating Dye Thiazole Orange and Derivatives. *Dyes and Pigments* **29**, 315 (1995).
87. Atanas, K. *et al.* New series of non-toxic DNA intercalators, mitochondria targeting fluorescent dyes. *Dyes and Pigments* **148**, 452–459 (2017).
88. Deligeorgiev, T. G. *et al.* Synthesis and properties of novel asymmetric monomethine cyanine dyes as non-covalent labels for nucleic acids. *Dyes and Pigments* **75**, 466–473 (2007).
89. Fürstenberg, A. *et al.* Ultrafast excited-state dynamics of DNA fluorescent intercalators: New insight into the fluorescence enhancement mechanism. *J Am Chem Soc* **128**, 7661–7669 (2006).
90. Eissa, F. M. & Abdel Hameed, R. S. Efficient green synthesis of monomethine cyanines via grinding under solvent-free conditions. *Green Processing and Synthesis* **5**, 283–288 (2016).
91. Zhang, X.-H., Wang, L.-Y., Nan, Z.-X., Tan, S.-H. & Zhang, Z.-X. Microwave-assisted solvent-free synthesis and spectral properties of some dimethine cyanine dyes as fluorescent dyes for DNA detection. *Dyes and Pigments* **79**, 205–209 (2008).
92. Alganzory, H. H., Arief, M. M. H., Amine, M. S. & Ebeid, E.-Z. Microwave-assisted Solvent-free Synthesis and Fluorescence Spectral Characteristics of some Monomethine Cyanine Dyes. *J Chem Pharm Res* **6**, 143–161 (2014).
93. Fu, Y. L., Zhang, B. R., Wang, V., Gao, X. X. & Wang, L. Y. Efficient one-pot three-component synthesis of monomethine cyanine dyes with quinoline nucleus and their spectral properties. *Bull Korean Chem Soc* **34**, 489–494 (2013).
94. Kurutos, A. *et al.* Bright green-emitting ds-DNA labeling employed by dicationic monomethine cyanine dyes: Apoptosis assay and fluorescent bio-imaging. *Dyes and Pigments* **157**, 267–277 (2018).
95. Deligeorgiev, T., Timtcheva, I., Maximova, V., Gadjev, N. & Drexhage, K.-H. Fluorescence Characteristics of Variously Charged Asymmetric Monomethine Cyanine Dyes in the Presence of Nucleic Acids. *J Fluoresc* **12**, (2002).
96. Timtcheva, I. *et al.* Homodimeric monomethine cyanine dyes as fluorescent probes of biopolymers. *J Photochem Photobiol* **58**, 130–135 (2000).
97. Rastede, E. E. *et al.* Spectral fine tuning of cyanine dyes: Electron donor-acceptor substituted analogues of thiazole orange. *Photochemical and Photobiological Sciences* **14**, 1703–1712 (2015).

98. Bengtsson, M., Karlsson, H. J., Westman, G. & Kubista, M. A new minor groove binding asymmetric cyanine reporter dye for real-time PCR. *Nucleic Acids Res* **31**, (2003).
99. Karlsson, H. J., Bergqvist, M. H., Lincoln, P. & Westman, G. Syntheses and DNA-binding studies of a series of unsymmetrical cyanine dyes: structural influence on the degree of minor groove binding to natural DNA. *Bioorg Med Chem* **12**, 2369–2384 (2004).
100. Karlsson, H. J., Eriksson, M., Perzon, E., Kerman, A. Ê. & Westman, G. Groove-binding unsymmetrical cyanine dyes for staining of DNA: syntheses and characterization of the DNA-binding. *Nucleic Acids Res* **31**, 6227–6234 (2003).
101. Ponchel, F. *et al.* Real-time PCR based on SYBR-Green I fluorescence: An alternative to the TaqMan assay for a relative quantification of gene rearrangements, gene amplifications and micro gene deletions. *BMC Biotechnol* **3**, (2003).
102. Marmiroli, N. & Maestri, E. Polymerase chain reaction (PCR). in *Food Toxicants Analysis* vol. Chapter 6 147–187 (Elsevier, 2007).
103. Cao, H. & Shockey, J. M. Comparison of TaqMan and SYBR green qPCR methods for quantitative gene expression in tung tree tissues. *J Agric Food Chem* **60**, 12296–12303 (2012).
104. Smith, M. Polymerase Chain Reaction (PCR). *National Human Genome Research Institute* https://www.genome.gov/genetics-glossary/Polymerase-Chain-Reaction (2023).
105. Farrar, J. S. & Wittwer, C. T. *High-Resolution Melting Curve Analysis for Molecular Diagnostics*. *Molecular Diagnostics* (Elsevier, 2017).
106. Ririe, K. M., Rasmussen, R. P. & Wittwer, C. T. Product Differentiation by Analysis of DNA Melting Curves during the Polymerase Chain Reaction. *Anal Biochem* **245**, 154–160 (1997).
107. Varga, A. & James, D. Real-time RT-PCR and SYBR Green I melting curve analysis for the identification of Plum pox virus strains C, EA, and W: Effect of amplicon size, melt rate, and dye translocation. *J Virol Methods* **132**, 146–153 (2006).
108. Invitrogen. SYBR ® green I nucleic acid gel stain product information sheet, vols. 1–5; 2006. *Invitrogen. SYBR ® green I nucleic acid gel stain product information sheet, vols. 1–5* (2006).
109. Haines, A. M., Tobe, S. S., Kobus, H. J. & Linacre, A. Properties of nucleic acid staining dyes used in gel electrophoresis. *Electrophoresis* **36**, 941–944 (2015).
110. Benke, A. & Manley, S. Live-Cell dSTORM of Cellular DNA Based on Direct DNA Labeling. *ChemBioChem* **13**, 298–301 (2012).
111. Kim, Y. K. RNA therapy: rich history, various applications and unlimited future prospects. *Exp Mol Med* **54**, 455–465 (2022).
112. *SYBR® Green II RNA Gel Stain*. *Molecular Probes* (Molecular Probes, 2001).
113. Lu, Y. J. *et al.* A molecular fluorescent dye for specific staining and imaging of RNA in live cells: A novel ligand integration from classical thiazole

orange and styryl compounds. *Chemical Communications* **51**, 15241–15244 (2015).
114. Aristova, D. *et al.* Monomethine cyanine probes for visualization of cellular RNA by fluorescence microscopy. *Methods Appl Fluoresc* **9**, (2021).
115. Suzuki, T., Fujikura, K., Higashiyama, T. & Takata, K. DNA Staining for Fluorescence and Laser Confocal Microscopy. *The Journal of Histochemistry & Cytochemistry* **45**, 49–53 (1997).
116. Henneberger, R., Birch, D., Bergquist, P., Walter, M. & Anitori, R. P. The fluorescent dyes TO-PRO-3 and TOTO-3 iodide allow detection of microbial cells in soil samples without interference from background fluorescence. *Biotechniques* **51**, 190–192 (2011).
117. Abd El-Aal, R. M. & Younis, M. Synthesis and antimicrobial activity of certain novel monomethine cyanine dyes. *Dyes and Pigments* **60**, 205–214 (2004).
118. Yarmoluk, S. M., Kryvorotenko, D. V, Balanda, A. O., Losytskyy, Y. & Kovalska, V. B. Proteins and cyanine dyes. Part III. Synthesis and spectroscopic studies of benzothiazolo-4-[1,2,6-trimethylpyridinium] monomethine cyanine dyes for fluorescent detection of bovine serum albumin in solutions. *Dyes and Pigments* **51**, 41–49 (2001).
119. Abdelbar, M. F. *et al.* Hybrid organic and inorganic solar cell based on a cyanine dye and quantum dots. *J Photochem Photobiol A Chem* **375**, 166–174 (2019).
120. Vus, K. *et al.* Cyanine dyes derived inhibition of insulin fibrillization. *J Mol Liq* **276**, 541–552 (2019).
121. Volkova, K. D. *et al.* Specific fluorescent detection of fibrillar α-synuclein using mono- and trimethine cyanine dyes. *Bioorg Med Chem* **16**, 1452–1459 (2008).
122. Liao, W.-Y. *et al.* Preparation of cyanine dye for high density optical recording disk. *Us. Pat.* US5958087 (1999).
123. Namba, K. *et al.* Photo-stabilized cyanine dyes and optical recording media. *Us. Pat.* US6071672A (2000).
124. Fanshun, M., Jianhua, S., Songjie, Y., He, T. & Kongchang. Chen. Preparation of asymmetric cyanine dyes for DVD-R CD. CN1148368C (2004).
125. Shang, L., Dong, S. & Nienhaus, G. U. Ultra-small fluorescent metal nanoclusters: Synthesis and biological applications. *Nano Today* **6**, 401–418 (2011).
126. Pyo, K. *et al.* Unique Energy Transfer in Fluorescein-Conjugated Au22 Nanoclusters Leading to 160-Fold pH-Contrasting Photoluminescence. *Journal of Physical Chemistry Letters* **9**, 5303–5310 (2018).
127. Martin, T. P., Bergmann, T., Gdhlich, H. & Lange, T. Shell Structure of Clusters. *J. Phys. Chem* **95**, 6421–6429 (1991).
128. Azubel, M. & Kornberg, R. D. Synthesis of Water-Soluble, Thiolate-Protected Gold Nanoparticles Uniform in Size. *Nano Lett* **16**, 3348–3351 (2016).

129. Azubel, M., Koh, A. L., Koyasu, K., Tsukuda, T. & Kornberg, R. D. Structure Determination of a Water-Soluble 144-Gold Atom Particle at Atomic Resolution by Aberration-Corrected Electron Microscopy. *ACS Nano* **11**, 11866–11871 (2017).
130. Azubel, M. *et al.* Electron microscopy of gold nanoparticles at atomic resolution. *Science (1979)* **345**, 909–912 (2014).
131. Tero, T. R. *et al.* Dynamic Stabilization of the Ligand-Metal Interface in Atomically Precise Gold Nanoclusters Au68 and Au144 Protected by meta-Mercaptobenzoic Acid. *ACS Nano* **11**, 11872–11879 (2017).
132. Tvedte, L. M. & Ackerson, C. J. Size-Focusing Synthesis of Gold Nanoclusters with p -Mercaptobenzoic Acid. *Journal of Physical Chemistry A* **118**, 8124–8128 (2014).
133. Ackerson, C. J., Jadzinsky, P. D., Sexton, J. Z., Bushnell, D. A. & Kornberg, R. D. Synthesis and bioconjugation of 2 and 3 nm-diameter gold nanoparticles. *Bioconjug Chem* **21**, 214–218 (2010).
134. Wong, O. A., Compel, W. S. & Ackerson, C. J. Combinatorial discovery of cosolvent systems for production of narrow dispersion thiolate-protected gold nanoparticles. *ACS Comb Sci* **17**, 11–18 (2015).
135. Qian, H. & Jin, R. Ambient synthesis of Au144(SR)60 nanoclusters in methanol. *Chemistry of Materials* **23**, 2209–2217 (2011).
136. Liu, G. *et al.* Synthesis of DNA-templated fluorescent gold nanoclusters. *Gold Bull* **45**, 69–74 (2012).
137. Chakraborty, S. *et al.* A Hybrid DNA-Templated Gold Nanocluster for Enhanced Enzymatic Reduction of Oxygen. *J Am Chem Soc* **137**, 11678–11687 (2015).
138. Guo, Y. *et al.* Natural protein-templated fluorescent gold nanoclusters: Syntheses and applications. *Food Chem* **335**, (2020).
139. Soleilhac, A., Bertorelle, F. & Antoine, R. Sizing protein-templated gold nanoclusters by time resolved fluorescence anisotropy decay measurements. *Spectrochim Acta A Mol Biomol Spectrosc* **193**, 283–288 (2018).
140. Negishi, Y., Nobusada, K. & Tsukuda, T. Glutathione-protected gold clusters revisited: Bridging the gap between gold(I)-thiolate complexes and thiolate-protected gold nanocrystals. *J Am Chem Soc* **127**, 5261–5270 (2005).
141. Bai, Y. *et al.* Glutathione-Stabilized Fluorescent Gold Nanoclusters Vary in Their Influences on the Proliferation of Pseudorabies Virus and Porcine Reproductive and Respiratory Syndrome Virus. *ACS Appl Nano Mater* acsanm.7b00386 (2018) doi:10.1021/acsanm.7b00386.
142. Tian, D., Qian, Z., Xia, Y. & Zhu, C. Gold nanocluster-based fluorescent probes for near-infrared and turn-on sensing of glutathione in living cells. *Langmuir* **28**, 3945–3951 (2012).
143. Wen, Q., Gu, Y., Tang, L. J., Yu, R. Q. & Jiang, J. H. Peptide-templated gold nanocluster beacon as a sensitive, label-free sensor for protein post-translational modification enzymes. *Anal Chem* **85**, 11681–11685 (2013).

144. Chen, L. Y., Wang, C. W., Yuan, Z. & Chang, H. T. Fluorescent gold nanoclusters: Recent advances in sensing and imaging. *Anal Chem* **87**, 216–229 (2015).
145. Katla, S. K., Zhang, J., Castro, E., Bernal, R. A. & Li, X. Atomically Precise Au25(SG)18 Nanoclusters: Rapid Single-Step Synthesis and Application in Photothermal Therapy. *ACS Appl Mater Interfaces* **10**, 75–82 (2018).
146. Shang, L. *et al.* Facile preparation of water-soluble fluorescent gold nanoclusters for cellular imaging applications. *Nanoscale* **3**, 2009–2014 (2011).
147. Alvarez, M. M. *et al.* Hidden Components in Aqueous 'gold-144' Fractionated by PAGE: High-Resolution Orbitrap ESI-MS Identifies the Gold-102 and Higher All-Aromatic Au-pMBA Cluster Compounds. *Journal of Physical Chemistry B* **120**, 6430–6438 (2016).
148. Koivisto, J. *et al.* Acid-base properties and surface charge distribution of the water-soluble au102(pmba)44 nanocluster. *Journal of Physical Chemistry C* **120**, 10041–10050 (2016).
149. Negishi, Y. *et al.* A critical size for emergence of nonbulk electronic and geometric structures in dodecanethiolate-protected Au clusters. *J Am Chem Soc* **137**, 1206–1212 (2015).
150. Sokołowska, K. *et al.* Towards Controlled Synthesis of Water-Soluble Gold Nanoclusters: Synthesis and Analysis. *Journal of Physical Chemistry C* **123**, 2602–2612 (2019).
151. Xie, J., Zheng, Y. & Ying, J. Y. Highly selective and ultrasensitive detection of Hg2+ based on fluorescence quenching of Au nanoclusters by Hg2+-Au+ interactions. *Chemical Communications* **46**, 961–963 (2010).
152. Wu, Y. T., Shanmugam, C., Tseng, W. Bin, Hiseh, M. M. & Tseng, W. L. A gold nanocluster-based fluorescent probe for simultaneous pH and temperature sensing and its application to cellular imaging and logic gates. *Nanoscale* **8**, 11210–11216 (2016).
153. Li, H. *et al.* Combination of active targeting, enzyme-triggered release and fluorescent dye into gold nanoclusters for endomicroscopy-guided photothermal/photodynamic therapy to pancreatic ductal adenocarcinoma. *Biomaterials* **139**, 30–38 (2017).
154. Saarnio, V. *Fluorescent Probes, Noble Metal Nanoparticles and Their Nanocomposites*. (JYU Dissertations, 2021).
155. McNaught, A. D., Wilkinson, A. & Chalk, S. J. 'Beer–Lambert law'. in *IUPAC Compendium of Chemical Terminology* (International Union of Pure and Applied Chemistry, Oxford, 2006).
156. McGhee, J. D. & von Hippel, P. H. Theoretical aspects of DNA-protein interactions: Co-operative and non-co-operative binding of large ligands to a one-dimensional homogeneous lattice. *J Mol Biol* **86**, 469–489 (1974).
157. Gross, J. H. *Mass Spectrometry - A Textbook*. (2017).
158. Mordehai, A. & Fjeldsted, J. *Agilent Jet Stream Thermal Gradient Focusing Technology*. www.agilent.com/chem/lcms (2009).

159. Günther, H. *NMR Spectroscopy: Basic Principles, Concepts and Applications in Chemistry*. (Wiley, Weinheim, 2013).
160. Rigaku Oxford Diffraction. CrysAlisPro Software System, Version 38.46, Rigaku Corporation. (2017).
161. Sheldrick, G. M. SHELXT - Integrated space-group and crystal-structure determination. *Acta Crystallogr A* **71**, 3–8 (2015).
162. Sheldrick, G. M. Crystal structure refinement with SHELXL. *Acta Crystallogr C Struct Chem* **71**, 3–8 (2015).
163. Sheldrick, G. M. A short history of SHELX. *Acta Crystallographica Section A* **A64**, 112–122 (2008).
164. Morris, G. M. *et al.* AutoDock4 and AutoDockTools4: Automated Docking with Selective Receptor Flexibility. *J Comput Chem* **30**, 2785–2791 (2009).
165. Frisch, M. J. *et al.* Gaussian 09; Gaussian, Inc. *Wallingford, CT* **32**, 5648–5652 (2009).
166. Van Der Spoel, D. *et al.* GROMACS: Fast, Flexible, and Free. *J Comput Chem* **26**, 1701–1718 (2005).
167. Hornak, V. *et al.* Comparison of Multiple Amber Force Fields and Development of Improved Protein Backbone Parameters. *Proteins: Structure, Function and Bioinformation* **65**, 712–725 (2006).
168. Ying, L. Nucleic acid detections and methods of their use. *US Pat.* US20130137875A1 (2013).
169. Thompson, M. Synthesis, photophysical effects, and DNA targeting properties of oxazole yellow-peptide bioconjugates. *Bioconjug Chem* **17**, 507–513 (2006).
170. Monnier, F. & Taillefer, M. Catalytic C-C, C-N, and C-O Ullmann-type coupling reactions. *Angewandte Chemie - International Edition* **48**, 6954–6971 (2009).
171. Nguyen, R. *et al.* Core-shell inversion by pH modulation in dynamic covalent micelles. *Soft Matter* **10**, 2926–2937 (2014).
172. Ramurthy, S. *et al.* Quinazolines for PDK1 Inhibition. 37 (2007).
173. Rhönnstad, P., Apelqvist, T., Wenner-Stål, M., Cheng, A. & Gordon, S. Novel Estrogen Receptor Ligands. 307 (2010).
174. Mao, F., Cheung, C., Leung, W., Windler, S. & Roberts, L. M. Fluorescent Compounds and Uses Thereof. (2014).
175. Gopika, G. S. *et al.* Chemistry of cyanine dyes - A review. *Mater Today Proc* **46**, 3102–3108 (2020).
176. Salorinne, K., Lahtinen, T., Malola, S., Koivisto, J. & Häkkinen, H. Solvation chemistry of water-soluble thiol-protected gold nanocluster Au102 from DOSY NMR spectroscopy and DFT calculations. *Nanoscale* **6**, 7823–7826 (2014).
177. Lahtinen, T. *et al.* Covalently linked multimers of gold nanoclusters Au102(: P -MBA)44 and Au~250(p -MBA)n. *Nanoscale* **8**, 18665–18674 (2016).

ORIGINAL PAPERS

I

SYSTEMATIC STUDY OF SYBR GREEN CHROMOPHORE REVEALS MAJOR IMPROVEMENT WITH ONE HETEROATOM DIFFERENCE

by

Saarnio, V. K., Alaranta, J. M. & Lahtinen, T. M., 2021

Journal of Materials Chemistry B, 9, 3484–3488.

https://doi.org/10.1039/D1TB00312G

Journal of Materials Chemistry B

COMMUNICATION

Cite this: *J. Mater. Chem. B*, 2021, **9**, 3484

Received 15th February 2021,
Accepted 7th April 2021

DOI: 10.1039/d1tb00312g

rsc.li/materials-b

Systematic study of SYBR green chromophore reveals major improvement with one heteroatom difference†

Ville K. Saarnio,* Johanna M. Alaranta and Tanja M. Lahtinen *

Five nucleic acid binding cyanine dyes were synthesized and their photophysical properties were evaluated. Changing a single heteroatom in the chromophore causes major differences both in brightness and photostability between the dyes. With such alteration, the brightness of the chromophore increased two-fold compared to the one found in SYBR Green I.

Detection of nucleic acids using fluorescent probes is an important tool for cell and molecular biologists in many different applications.[1] These include visualising DNA using gel electrophoresis,[2] and imaging RNA in microscopy,[3] among others. Monomethine cyanine dyes are widely used for these purposes due to their turn-on fluorescence, selective to binding to double stranded nucleic acids.[4] The fluorescence light up is induced by rigidification of the chromophore after intercalating between base pairs of a nucleic acid.[5,6] As such, dyes with this type of binding offer highly selective sensing of nucleic acids in cells over other biomolecules. This class of nucleic acid stain has been studied vigorously[7–9] and as a result, the SYBR family of fluorescent probes has become a popular choice for their sensing.[10–12] They can be employed for general visualization of nucleic acids, from electrophoresis gels[13] to microscopy applications.[14] There are a few attributes that such fluorescent probes need to exhibit to be viable for sensing applications. These include high brightness combined with low background emission, high photostability under prolonged excitation, and low cytotoxicity if applied *in vivo*. In particular, the demand for increasingly bright nucleic acid sensors continues to increase, as the ambition for imaging singular biomolecules in a cellular environment grows.[15,16]

In order to meet this demand, we have synthesized five new cyanine dyes and evaluated their photophysical properties (Chart 1). The synthesis of the compounds was conducted using previously published protocols,[17,18] combined with an additional nucleophilic substitution step, as shown in the ESI† Scheme S2. Our previous results indicated significant differences in the dye properties of the heteroatoms in the chromophore;[18] in this study, we set out to evaluate those differences. The examined dyes were varied in structure by changing between an oxazole and thiazole moiety and varying the 2-substituent between a mercaptomethyl, dimethylamine or chloride.

Already the absorption and emission spectra of the synthesized dyes exhibited significant differences (Fig. 1a). The lowest energy absorption maxima of the dyes were found between 455 and 516 nm, differing slightly between solvents. The introduction of third period heteroatoms seems to decrease the absorption energy of the dyes as supported by OxN **2** showing the highest and ThzS **5** the lowest energy of absorption, with other products found half way between the two. The emission spectra behave in a similar manner with emission maxima observed at the region of 492–535 nm when bound to calf thymus DNA (ctDNA) (Fig. 1b). The excitation/emission spectra for individual dyes are presented in the ESI† Fig. S9–S13. This lead to Stoke's shifts from 16 to 28 nm with OxS **3** being responsible for the lowest value. Surprisingly, the presence of dimethylamine substitution (OxN **2** and ThzN **4**) seems to increase the Stoke's shift compared to the other products OxCl **1** and ThzS **5**.

The absorption coefficients (ε) of the dyes were evaluated in three different solvents; tris-EDTA (TE) buffer, ethanol and 100 μM ctDNA in TE buffer (S14–S16, ESI†). No clear relationship

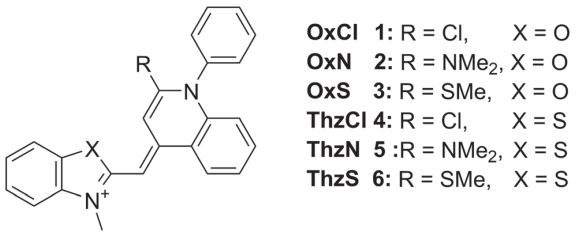

Chart 1 Chemical structure of the studied cyanine dyes.

Department of Chemistry, Nanoscience Center, University of Jyväskylä, Jyväskylä FI-40500, Finland. E-mail: tanja.m.lahtinen@jyu.fi

† Electronic supplementary information (ESI) available: Experimental details, synthesis and characterization of the products, raw absorption/fluorescence spectra and insight into the binding characterization. See DOI: 10.1039/d1tb00312g

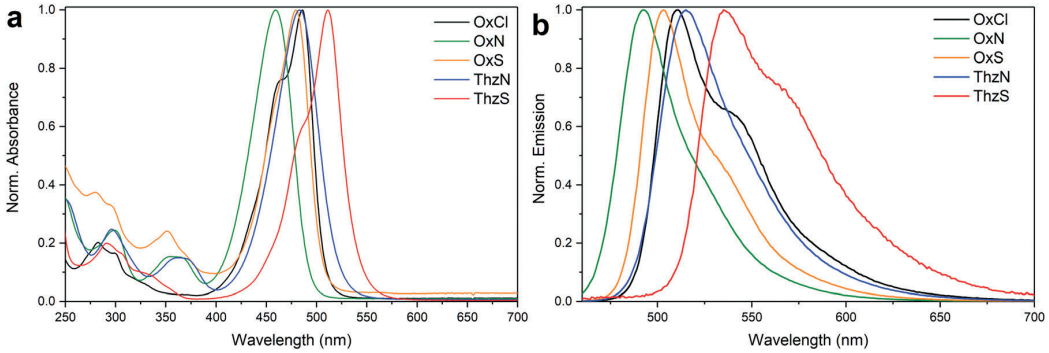

Fig. 1 (a) Normalized absorption spectra of the dyes in 19.6 μM concentration in ethanol. (b) Normalized emission spectra of the dyes in 100 μM ctDNA in TE Buffer.

between the dye structure and absorptivity was observed, although the OxS **3** displayed significantly lower ε values compared to the other dyes across all media. In the ThzN **4** compound, the given absorptivity was lower by 10 000 M^{-1} cm^{-1}, compared to molecules **1**, **2**, and **5**. Generally, compound **2** showed the highest absorptivity of 73 600 M^{-1} cm^{-1} in ethanol between the three dyes and comparable values to the two others in aqueous media. In order to evaluate which chromophore offers the best brightness, we determined the quantum yield Φ of all five dyes, when fully bound to ctDNA, using fluorescein as a standard (Fig. S17 and S18, ESI†).[19] These values and the other spectral characteristics of the synthesized dyes are presented in Table 1. The benefit of maintaining a chromophore consisting of second period elements becomes apparent once again as the quantum yield of OxN **2** was determined to be 100%. Compared to this result, replacing one of the heteroatoms with sulphur in OxS **3** and ThzN **4** resulted in the quantum yields diminishing significantly, by 24% and 30%, respectively. Ohulchanskyy and co-workers found a similar trend when evaluating a series of xanthene dyes by varying a heteroatom between oxygen, sulphur and selenium in the chromophore.[20] In particular, the chlorine atom in the 2-position has a dramatic effect on the quantum yield. The Φ value for OxCl **1** was found to be as low as 18% similar in magnitude to the 14% of two-sulphur-containing ThzS **5**. It is possible, that the chlorine (and other halogens) atom offers additional pathways for non-radiative relaxation, perhaps due to the intersystem crossing caused by the heavy-atom effect inflicted by the substituent. Similar observations have been made by Vasilev *et al.*,[21] who synthesized a series of halogen-containing thiazole orange (TO) derivatives, where increasing inclusion of halogens on the chromophore led exclusively to lower quantum yields. In general, the trend towards favouring second period elements to maximize the brightness seems evident among the synthesized dyes.

Next, to establish the stability of the dyes in practical use, we exposed them to a microscope light source, *i.e.* a 3300 K halogen lamp of 22 mW cm^{-2} light intensity. The use of such a light source not only provided a sufficient timeframe for observing dye decomposition but also gave a reasonable source of maximal excitation light that the dyes would experience in daily use. However, this also led to some differences in the amount of light absorbed depending on the absorption maximum of the dye, as demonstrated in Fig. S19 (ESI†). The photobleaching of the dyes was then followed over time, by measuring dye absorbance at different points of time and fitting exponential decay functions to observed absorption maxima, as shown in Fig. 2a and b. While measuring fluorescence would have granted higher sensitivity to the photobleaching, the non-fluorescent state of the dyes in TE Buffer (Fig. 2a) would have gone unmeasured in addition to a solution of ctDNA (Fig. 2b). We observed that the differences in the dye half-lives are remarkable between each other and different media (Table 2). Surprisingly, the OxCl **1** dye exhibits the highest photostability among the examined molecules in both media. The ThzN **4** on the other hand was highly unstable compared to the other dyes. In general, the dyes have significantly different half-lives free in solution and bound to ctDNA. As expected, the dyes decompose faster in the TE buffer compared to the ctDNA solution.

Free in solution, the observed values varied between 0.5–6.3 h, increasing to 1.6–36 h when DNA bound. Interestingly, the oxazole

Table 1 Spectral and brightness related parameters measured for the studied dyes

Dye	OxCl **1**	OxN **2**	OxS **3**	ThzN **4**	ThzN **5**
λ_{exc} (nm)	491	464	487	488	514
λ_{emi} (nm)	511	492	503	515	535
Stoke's shift (nm)	20	28	16	27	21
$\varepsilon_{max,\ TE}$ ($\times 10^3$ M^{-1} cm^{-1})	59.5 ± 0.4	56.5 ± 0.8	16.0 ± 0.3	35.3 ± 1	47.5 ± 2
$\varepsilon_{max,\ EtOH}$ ($\times 10^3$ M^{-1} cm^{-1})	60.7 ± 0.9	73.6 ± 0.6	25.7 ± 0.3	56.9 ± 0.3	65.4 ± 1.1
$\varepsilon_{max,\ ctDNA}$ ($\times 10^3$ M^{-1} cm^{-1})	42.0 ± 0.3	47.3 ± 0.2	18.0 ± 0.3	36.5 ± 0.3	49.1 ± 0.1
Quantum yield Φ (%)	18	100	76	68	14
Brightness (M^{-1} cm^{-1})	7600	47 300	13 700	24 800	6900

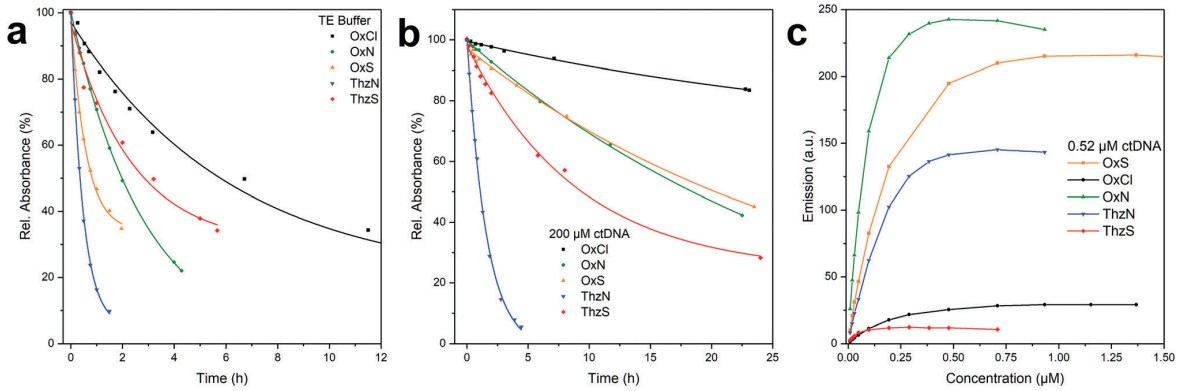

Fig. 2 Exponential decay functions fitted to the relative decrease of the initial absorption at the maximum wavelength over time in (a) TE Buffer and (b) 200 μM ctDNA. Data can be derived from Fig. S20 and S21 (ESI†). (c) Fluorescence emission maxima plotted with increasing dye concentration in 0.52 μM ctDNA solution at room temperature derived from Fig. S22 (ESI†).

Table 2 Collection of parameters involved in photostability and ctDNA binding of the dyes

Dye	OxCl **1**	OxN **2**	OxS **3**	ThzN **4**	ThzS **5**
K_a ($\times 10^6$ M^{-1})	1.4 ± 0.04	8.5 ± 1.5	4.6 ± 1	5.8 ± 0.4	2.3 ± 0.1
n (bp)	4.3 ± 0.3	3.4 ± 0.4	1.6 ± 0.1	2.1 ± 0.12	1.7 ± 1
ΔG^0 (kJ mol^{-1})	−34.6	−39.0	−37.5	−38.1	−35.8
$t_{1/2,\ TE}$ (h)	6.3	2.9	0.6	0.5	2.4
$t_{1/2,\ 200\ \mu M\ ctDNA}$ (h)	35.9	32.4	29.8	1.6	9.0

moiety benefits from binding to nucleic acids notably more, compared to thiazole containing products. In particular, OxS **3** that decomposes rapidly in TE Buffer, experiences a 50-fold increase in its half-life after binding to its target. The thiazole derivatives **4** and **5** only stabilized by 3.2-fold and 3.75-fold, respectively. While dyes **1** and **2** were already the most stable in TE buffer, the enhancements to photostability were further improved by 5.7-fold and 11.2-fold, respectively. The knowledge of stability in both media is highly important, as the dyes are constantly interchanging between bound and unbound states in solution.

To better understand the differences between dyes in their nucleic acid binding, we conducted two fluorescence titration experiments; one with a limited amount and the other with a high excess of ctDNA available for binding (Fig. 2c and Fig. S24b, ESI† respectively). From the relative fluorescence between the two experiments, it was possible to determine both the binding constant (K_a) and the number of nucleic acid base pairs required to accommodate a single dye molecule (n). This was made possible by employing the theoretical model of DNA–protein interactions developed by von Hippel and McGhee elucidated in more detail in our previous work.[18,22] The processing of the obtained data produced a Scatchard plot (Fig. S24c, ESI†) that enabled the fitting of the McGhee and von Hippel equation for non-cooperative binding to obtain values for K_a, n and subsequent determination of the Gibbs free energy of binding involved (ΔG^0, Table 2). The currently accepted model of nucleic acid binding for SYBR family (and TO related) compounds is, that the quinoline moiety intercalates between base pairs, and the indole moiety binds through electrostatic interactions to the phosphate group while the 2-substituents settle along the minor/major groove.[23,24]

As the synthesized dyes had a high structural similarity, we did not expect major differences among the dyes to be observed in the binding values. As expected, the binding site size between dimethylamine and methylthiol substituted dyes differs, as the extra methyl group on the amine requires additional space in binding. The effects to the binding energy of this structural change are similar between the two comparing pairs (**2** *vs.* **3** and **4** *vs.* **5**); this change leads to a decrease of 1.5 kJ mol^{-1} and 2.3 kJ mol^{-1}, respectively. Curiously, also the changes from oxazole to thiazole had a significant effect on the binding energy. Comparing the binding energies between the two derivative pairs (**2** and **4**, **3** and **5**) the ΔG^0 is found to differ by 0.9 kJ mol^{-1} and 1.7 kJ mol^{-1}, respectively. These changes can be contributed to the change of both to the electronegativity of the heteroatom, as well as to the weak binding provided by the additional methyl group in the first pair. In the case of the latter comparison pair, the differences are solely heteroatom derived. Subtracting the difference of the latter pair from the former yields 0.6 kJ mol^{-1} in both cases, giving a realistic estimate of the contribution of a single methyl group to the binding energy. However, another series aimed towards confirming that this estimate should be conducted. The effect on the binding energy due to the change

from thiazole to oxazole can be explained by the electronegativities of the other heteroatom present in the 2-position. Oxygen, nitrogen and sulphur have electronegativities of 3.44, 3.04, and 2.58 in the Pauling scale, respectively. An oxygen atom in the oxazole is able to draw a greater amount of electron density from a sulphur atom *vs.* a nitrogen that is more negatively charged. As the DNA bases are electronegative in nature, it is logical that depleting the intercalating molecule of electron density would increase the binding affinity, as was observed. Furthermore, by examining the electronegativity difference between the heteroatoms in the comparison of **2** and **4**, as well as **3** and **5**, we found a relation to the binding energy differences between the two pairs. Multiplying the 1.7 kJ mol^{-1} with the electronegativity difference gives 0.8 kJ mol^{-1}, very close to the 0.9 kJ mol^{-1} value of the **2** and **4** pair. The low binding energy determined for OxCl **1** also supports this notion, although part of this might be due to chlorine hindering the intercalation itself, as observed with the high *n* value for the compound. The idea of manipulating electron density in the intercalating part of the molecule to increase target binding warrants high interest when designing new molecules in the future.

To summarize, in this work, we set out to synthesize five nucleic acid binding cyanine dyes with different heteroatomic constitutions in order to evaluate their photophysical properties. The molecules were designed so that the effects of single atom differences in the chromophore could be evaluated. In addition to the determination of the brightness related parameters, also the photostability, binding energy, and binding site size with ctDNA were established for all dyes. Among the evaluated products one dye, OxN **2**, showed outstanding performance compared to the others. These properties include brightness of 47 300 M^{-1} cm^{-1}, −39 kJ mol^{-1} binding energy, and over 32 h photobleaching half-life in complex with ctDNA, coupled with a 28 nm Stoke's shift. Generally, the introduction of second period heteroatoms (S and Cl) seemed to decrease the performance in all aspects compared to OxN **2**. In particular, the introduction of the chlorine (**1**) or two sulphur atoms (**5**) had a dramatic effect on the quantum yield of the dyes, albeit the photostability of **1** was the best among the compounds herein. The binding studies on the synthesized molecules indicated a benefit from introducing more electronegative elements to the intercalating moiety in the dyes. As researchers aspire towards the detection of diminishing amounts of nucleic acids in many biological contexts, the demand for increasingly sensitive probes rises. While another approach to this problem has been preparing artificial nucleosides with fluorescent properties, this method requires always synthetically altering the nucleic acid strand in question.[25] Intercalating turn-on fluorescent probes offers a universal solution for all solution based nucleic acid detection. The molecules presented in this work should be applicable in a similar manner to the SYBR family dyes in imaging and otherwise. This is why such probes with continuously improving photophysical properties are highly enticing and hence, understanding the underlying patterns leading to the best possible results should be of interest to every chemist, biochemist and biologist involved in their use.

This work was supported by Jane and Aatos Erkko Foundation project Novel Probes for Discovering Anti-Virals and Vilho, Yrjö and Kalle Väisälä Fund. We are thankful for the assistance provided by Dr Elina Kalenius with mass spectroscopy. The authors thank Prof. Kari Rissanen for his contribution to the fruitful discussion.

Conflicts of interest

There are no conflicts to declare.

Notes and references

1 L. J. Kricka, *Ann. Clin. Biochem.*, 2002, **39**, 114–129.
2 A. M. Haines, S. S. Tobe, H. J. Kobus and A. Linacre, *Electrophoresis*, 2015, **36**, 941–944.
3 S. Ray, J. R. Widom and N. G. Walter, *Chem. Rev.*, 2018, **118**, 4120–4155.
4 A. Bruce, in *Topics in Heterocyclic Chemistry*, ed. L. Strekowski, Springer, Pittsburgh, 14th edn, 2008, pp. 11–29.
5 H. Ihmels and D. Otto, *Top. Curr. Chem.*, 2005, **258**, 161–204.
6 V. Karunakaran, J. L. Pérez Lustres, L. Zhao, N. P. Ernsting and O. Seitz, *J. Am. Chem. Soc.*, 2006, **128**, 2954–2962.
7 N. I. Shank, H. H. Pham, A. S. Waggoner and B. A. Armitage, *J. Am. Chem. Soc.*, 2013, **135**, 242–251.
8 H. J. Karlsson, M. H. Bergqvist, P. Lincoln and G. Westman, *Bioorg. Med. Chem.*, 2004, **12**, 2369–2384.
9 T. G. Deligeorgiev, N. I. Gadjev, A. A. Vasilev, V. A. Maximova, I. I. Timcheva, H. E. Katerinopoulos and G. K. Tsikalas, *Dyes Pigm.*, 2007, **75**, 466–473.
10 X. Jin, S. Yue, V. L. Singer, L. J. Jones, M. P. Beaudet, C.-Y. Cheung and R. S. Tuma, *Anal. Biochem.*, 2003, **288**, 278–288.
11 H. Zipper, H. Brunner, J. Bernhagen and F. Vitzthum, *Nucleic Acids Res.*, 2004, **32**, e103.
12 W. E. Evenson, L. M. Boden, K. A. Muzikar and D. J. Oleary, *J. Org. Chem.*, 2012, **77**, 10967–10971.
13 L. J. Jones, S. T. Yue, C. Y. Cheung and V. L. Singer, *Anal. Biochem.*, 1998, **265**, 368–374.
14 T. Suzuki, K. Fujikura, T. Higashiyama and K. Takata, *J. Histochem. Cytochem.*, 1997, **45**, 49–53.
15 A. S. Boutorine, D. S. Novopashina, O. A. Krasheninina, K. Nozeret and A. G. Venyaminova, *Molecules*, 2013, **18**, 15357–15397.
16 A. D. Cawte, P. J. Unrau and D. S. Rueda, *Nat. Commun.*, 2020, **11**, 1283.
17 L. Ying, *US Pat.,* US20130137875A1, 2013.
18 V. K. Saarnio, K. Salorinne, V. P. Ruokolainen, J. R. Nilsson, T.-R. Tero, S. Oikarinen, L. M. Wilhelmsson, T. M. Lahtinen and V. S. Marjomäki, *Dyes Pigm.*, 2020, **177**, 108282.
19 C. Würth, M. Grabolle, J. Pauli, M. Spieles and U. Resch-Genger, *Nat. Protoc.*, 2013, **8**, 1535–1550.
20 T. Y. Ohulchanskyy, D. J. Donnelly, M. R. Detty and P. N. Prasad, *J. Phys. Chem. B*, 2004, **108**, 8668–8672.
21 A. A. Vasilev, M. I. Kandinska, S. S. Stoyanov, S. B. Yordanova, D. Sucunza, J. J. Vaquero, O. D. Castaño, S. Baluschev and S. E. Angelova, Beilstein, *J. Org. Chem.*, 2017, **13**, 2902–2914.

22 J. D. McGhee and P. H. von Hippel, *J. Mol. Biol.*, 1974, **86**, 469–489.
23 C. D. Geddes, A. I. Dragan, J. R. Casas-Finet, M. A. Schenerman, J. B. McGivney, R. J. Strouse, R. Pavlovic and E. S. Bishop, *J. Fluoresc.*, 2012, **22**, 1189–1199.
24 A. I. Dragan, J. R. Casas-Finet, E. S. Bishop, R. J. Strouse, M. A. Schenerman and C. D. Geddes, *Biophys. J.*, 2010, **99**, 3010–3019.
25 R. T. Ranasinghe and T. Brown, *Chem. Commun.*, 2011, **47**, 3717–3735.

II

OPTIMIZING THE SYBR GREEN RELATED CYANINE DYE STRUCTURE TO AIM FOR BRIGHTER NUCLEIC ACID VISUALIZATION

by

Alaranta J. M., Truong, K-N., Matus, M. F., Malola, S. A., Rissanen, K. T., Shroff, S. S., Marjomäki, V. S., Häkkinen, H. J. & Lahtinen, T. M. 2022

Dyes and Pigments, 208, 110844.

https://doi.org/10.1016/j.dyepig.2022.110844

Dyes and Pigments 208 (2022) 110844

Contents lists available at ScienceDirect

Dyes and Pigments

journal homepage: www.elsevier.com/locate/dyepig

Optimizing the SYBR green related cyanine dye structure to aim for brighter nucleic acid visualization

Johanna M. Alaranta [a], Khai-Nghi Truong [a], María Francisca Matus [b], Sami A. Malola [b], Kari T. Rissanen [a], Sailee S. Shroff [c], Varpu S. Marjomäki [c], Hannu J. Häkkinen [a,b], Tanja M. Lahtinen [a,*]

[a] University Of Jyväskylä, Department of Chemistry, Nanoscience Centre, Jyväskylä, P.O. Box 35, FI-40014, Finland
[b] University Of Jyväskylä, Department of Physics, Nanoscience Centre, Jyväskylä, P.O. Box 35, FI-40014, Finland
[c] University Of Jyväskylä, Department of Cell and Molecular Biology, Nanoscience Center, Jyväskylä, FI-40014, Finland

ARTICLE INFO

Keywords:
Cyanine dye
Nucleic acid
Fluorescent probe
X-ray crystal structure
Molecular docking
DFT calculations

ABSTRACT

In recent years, the studies of RNA and its use for the development of RNA based vaccines have increased drastically. Although cyanine dyes are commonly used probes for studying nucleic acids, in a wide range of applications, there is still a growing need for better and brighter dyes. To meet this demand, we have systematically studied the structure of SYBR green-related cyanine dyes to gain a deeper understanding of their interactions with biomolecules especially how they interact with nucleic acids and the structural components which makes them strongly fluorescent. Herein, five new dyes were synthesized, and their photophysical properties were evaluated. Observations of photophysical characteristics were compared to calculations by using density functional theory in its ground state and time-dependent form to model the optical absorption spectra and excited state properties of the selected molecules. Single crystal X-ray crystal structures of five cyanine dyes were determined and the interactions of the cyanine dye-DNA complex were studied by using molecular docking and molecular dynamics calculations. Three molecular structural features were discovered: a) removing the benzene ring from the thiazolium moiety of the dye lowers the fluorescence drastically, and that the quantum yield can be enhanced, therefore increasing the fluorescence, by b) incorporating methanethiol substituent at the quinoline moiety instead of dimethylamine or c) changing the thiazolium moiety to an oxazolium moiety.

1. Introduction

Cyanine dye studies are nowadays widely focused on biological and medicinal research. New potential uses for cyanine dyes are for example cancer treatment [1–3], nanofibers mimicking tissues [4], detecting cysteine, which is linked to many illnesses, such as Alzheimer's disease [5], turn-on probes for redox reactions in cells [6] and using cyanine dyes as selective fluorescent probes for RNA [7]. Cyanine dyes are already a popular choice as fluorescent probes to image nucleic acids in many cell and molecular biology laboratories [8]. In the field of cyanine dyes the monomethine cyanine dyes are one of the most used fluorescent probes for visualizing nucleic acids in different applications due to their fluorescence enhancement when binding to nucleic acids [9].

Cyanine dyes can be defined as molecules containing two nitrogen substituted heterocycles sharing a cationic charge through a conjugated carbon bridge [10]. Monomethine cyanine dyes are one class of the cyanine dyes, given the name due to only one monomethine carbon in the carbon bridge [11]. A classical way to synthesize monomethine cyanine dyes is the cyanine condensation reaction of two quaternary amine salts [12]. Molar absorptivity of these compounds usually range from 10^4–10^5 $cm^{-1}M^{-1}$ and they can exhibit up to 1000-fold increase in fluorescence intensity when binding nucleic acids. Due to these excellent qualities, this host-quest type of interaction between the cyanine dyes and nucleic acids is widely utilized in different applications [10].

The great fluorescence enhancement of cyanine dyes is described as a result of restriction of the torsional motion of the molecule. The group of Geddes [13] has shown that both PicoGreen and SYBR Green I form a complex with double stranded DNA (dsDNA), in which the aromatic quinolinium core unit intercalates into the dsDNA, while the benzothiazolium unit, carrying a localized positive charge enhances the

* Corresponding author.
E-mail address: tanja.m.lahtinen@jyu.fi (T.M. Lahtinen).

https://doi.org/10.1016/j.dyepig.2022.110844
Received 2 September 2022; Received in revised form 7 October 2022; Accepted 8 October 2022
Available online 13 October 2022

binding affinity by providing additional electrostatic interaction with the DNA. In addition, the dimethylaminopropyl side chains are positioned in the minor groove of the DNA for added stability of the complex. Another possible binding mode is minor groove binding where the whole dye molecule binds in minor grove of the dsDNA. For example, Karlsson et al. [14] reported two minor groove binding unsymmetrical cyanine dyes also suitable for DNA detection.

Knowledge of the binding and structural modifications to the brightness of these dyes is mostly based on a few examples. However, for the future development of more selective and efficient dyes that enable the study of more complex biological systems (*e.g.* viruses and their mode of action in living cells), it is highly significant to understand the structural and binding properties of the cyanine dye molecules. Since these fluorescent probes must have some particular features to be useable for sensing applications: high brightness combined with low background emission, high photostability under prolonged excitation, and low cytotoxicity when applied *in vivo*, it is important to understand how the structures of these dyes can be modified without losing these features but still exhibit a new quality.

The aim of this study is to reveal the key factors that improve the behavior of the monomethine cyanine dyes as fluorescent probes for nucleic acid staining. To accomplish this, we made systematic modifications to quinoline, benzothiazolium, and -oxazolium moieties around the fixed core fluorophore skeleton of different SYBR green-related monomethine cyanine dye molecules. Five new monomethine cyanine dyes (**1–5**) were prepared and their photophysical properties compared with other known dyes (**6**–**9**) of the same family using fluorescence and UV–Vis spectroscopy. For selected dyes (**1**, **2**, **6**, **8**, **10a** and **10b**, X-ray crystal structures were determined, and their potential DNA binding modes were studied by molecular modeling.

2. Materials and methods

All used reagents and materials were commercially available and used as received unless otherwise mentioned. All dyes were synthesized with a modified and developed synthesis method previously published by our group [15] based on protocols found in literature [16,17].

2.1. Synthesis

All of the studied dyes (**1-10**) were synthesized by first introducing quinolone or pyridine **11** to phosphorus oxychloride to get positively charged ions **12** (see Scheme 1). After that cyanine condensation reaction was done as described by Karlsson et al. [18]. This resulted in a mixture of dyes with chlorine and methyl thiol substituents in pyridine or quinoline moiety. After separation, thiol dyes can be used as such, and chlorine dye can be mixed with dimethylamine to obtain amine dyes.

The synthesis procedure is very versatile, and it can be used with differently substituted starting materials as seen in Scheme 1. All new cyanine dyes are presented in Fig. 2. along with the dyes previously published [15].

2.2. Analytical methods

Synthesized dyes were characterized using mass spectrometry and NMR spectroscopy. NMR spectra were measured with Bruker Avance III 500 MHz NMR spectrometer. Agilent LC-IMMS-TOF mass spectrometer was used to determine accurate mass for each dye.

Photophysical properties of the dyes were measured with UV–Vis and fluorescence spectrometers. Agilent Technologies Cary 8454 was used to measure absorbance and Varian Cary Eclipse for fluorescence studies.

Atomic coordinates and structure factors for the reported crystal structures have been deposited with the Cambridge Crystallographic Data Centre (CCDC) under accession numbers 2194823 (PyrON **1**), 2194824 (PyrN **2**), 2194825 (OxN **6**), 2194826 (ThzN **8**) and 2194827 (**10**, see Scheme S10.).

For comprehensive synthetic and experimental details please see the Supporting Information.

3. Results and discussion

In this study, we have synthesized five new nucleic acid-binding cyanine dyes to study how different functional groups affect to the nature of the quality of the dyes in photophysical measurements. In our previous paper, we concluded that a single heteroatom could change the qualities of the dyes drastically and oxazolium moiety seemed to produce better dyes [15]. With that in mind, we were interested to see the effect of the thiazolium moiety. Therefore, we present the new S-series of dyes containing thiazolium moieties with modified structures. We set our goal to study the structures of these cyanine dyes to see if the aromatic rings in the molecules have an essential role in the brightness and

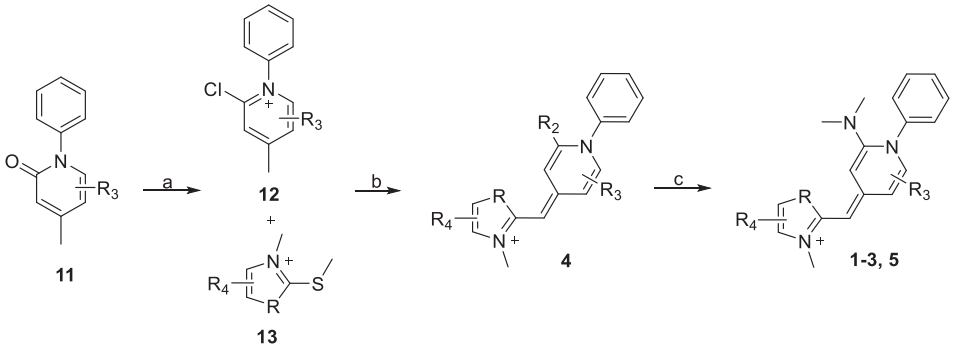

Pyridine moiety, R_3 = none
1 R = O, R_4 = Ph
2 R = S, R_4 = Ph

Quinoline moiety, R_3 = Ph, R_4 = none
3 R = S, R_2 = -NMe_2,
4 R = S, R_2 = -SMe,
5 R = S, R_2 = -NMe_2, no double bond at the thiazolium moiety

Scheme 1. Synthesis scheme for studied dyes. Reagents: a) $POCl_3$, 1.2-DCE, Δ b) DCM, Et_3N c) Chlorine dye from previous step, $HNMe_2$, ACN.

DNA binding modes. Trusting the results will open new ideas for developing dyes in the future. The five new synthesized cyanine dyes and selection of the commercial cyanine dyes were compared to our previously published cyanine dyes [15] to get deeper information on how these modifications affect the fluorescence behavior.

The R_3 represents the benzene ring for dyes with quinolone moiety, while for pyridine moiety, there is no R_3 substituent. Thiazolium and oxazolium dyes have sulfur and oxygen as R atom, respectively (see Scheme 1). Accordingly, these two different groups of dyes are represented as sulfur and oxygen series in Fig. 2. The arm R_2 can be either methyl thiol or dimethylamine.

The currently accepted model for interaction between SYBR green-related dyes and dsDNA is based on the intercalation of quinoline moiety (red circle in Fig. 1.) between the base pairs in the double helix. Thiazolium/oxazolium moiety (blue circle in Fig. 1.) bears the positive charge, and hence, provides electrostatic interactions with the negatively charged phosphate groups in the nucleic acid backbone. The arms (green circle in Fig. 1.) could bind along the helix with minor or major groove, and therefore it enhances the binding [13].

3.1. X-ray crystallography

The crystallization of dyes **1**–**9** and separation of **10a** and **10b** (see Scheme S10) were attempted, but crystals with suitable quality for single crystal X-ray structural analysis resulted in only for dyes **1**, **2** (a mixed crystal, see Fig. 3), **6**, **8** and **10** (a mixed crystal, see Scheme S10. and Fig. S15) and X-ray structures are shown in Fig. 3. The crystal data and other experimental details are given in SI. The main molecular skeleton (oxazolium/thiazolium moiety and quinoline/pyridine moiety) of all dyes is nearly planar in the solid state, despite the fact that it appears to be non-planar in solution. Only the dimethylamine (-NMe_2) arm and the phenyl group attached to the main skeleton deviate from the planarity due to their close proximity. The configuration of **2** in the solid state differs from all other dyes. Using O/N atom of the oxa/thia moiety and the -NMe_2 or -SMe arms as substituents of the C═C moiety (Fig. 3.), then **2** is defined as *cis*, while all other dyes have a *trans* configuration. In dye **6** (the best performing dye from the studied dyes), the -NMe_2 arm (which is planar too) has a twist/torsion angle of 20.7° while the phenyl group is nearly perpendicular towards the plane of the main skeleton of the molecule (twist angle of 77.4°). The other dyes containing the -NMe_2 arm have similar twist angles: **1**, 33.1° and 53.9°; **2,** 42.8° and 65.0° and **8**–35.6°, −64.6°. The commercial dye, **SYBR Green II** and **MeS**, which have R–S arm instead of -NMe_2, differ from the above as the R–S group is co-planar with the main skeleton and the phenyl ring twist angle is closer to 90° (**MeS** 79.3° and **SYBR Green II** 88.1°). The overall structure of these dyes is very similar (see the VDW radii plots in the SI, Fig. S16). The major structural difference affecting the brightness of the dye is the thiazolium moiety. The longer C–S bonds, 1.74 Å *vs.* 1.37/1.39 Å opens the C═C–C angle between the oxa/thia moiety and quin/py moiety angle from 125° to 128°. In addition, the larger 5-membered thiazolium ring induces a change in the mutual orientation of the oxa/thia and quin/py moiety of the dye. The cent1 – Csp2 – cent2 angle (cent1, Csp2 and cent2 being the centroid of the oxa/thia benzene ring, the alkene carbon, and the centroid to the benzene ring of the quin/py moiety, respectively) in the thiazolium moiety-containing dyes opens up by 10°, being 137.8° in **2** and 136.2° in **8**. In the oxazolium moiety-containing dyes, the same angle is 127.4°, 126.4°, 124.1°, and 126.8° for **1**, **6**, **SYBR Green II**, and **MeS**, respectively.

3.2. Photophysical studies

Photophysical properties of dyes (**1–9**) were evaluated with UV–Vis- and fluorescence spectrometers. For the molar absorption coefficient, series of absorption titrations were done for each dye in EtOH, TE buffer and ctDNA in TE buffer solution to visualize the linear correlation between the concentration and the absorbance [19]. For the fluorescence measurements, titrations were measured in excess ctDNA in TE buffer (100 μM solution) and in restricted ctDNA concentration (0.52 μM). These fluorescence titrations were used to estimate the binding properties of the dyes according to the McGhee Von Hippel equation [20]. The quantum yields of the dyes were determined by comparing the dyes to fluorescein standard by exciting the studied dyes and the fluorescein at same wavelengths regardless of the previously measured maxima. Resulting emission spectra were integrated and plotted against absorbance maxima at the used excitation wavelength. Slopes of these linear plots were then used to determine the quantum yields for the dyes [21].

All dyes (**1–9**) absorb light at different wavelengths which can be seen from Fig. 4., ranging from 466 to 511 nm. Some correlations on the absorption maxima depending on the structures of the dyes can be seen from the plot. The dyes with benzothiazolium moiety (ThzS **9**, ThzN **8** and PyrN **2**) seem to absorb at higher wavelengths than dyes containing oxazolium moieties; dyes **9**, **8** and **2** have maxima at higher wavelengths compared to MeS **7**, OxN **6** and PyrON **1**. Similar observations have been made by Benson and Kues [22]. The dyes with thiol arm, **7**, **9** and QuinoS **4** absorb at higher wavelengths than the amine arm containing dyes, **6**, **8** and QuinoN **3**. Also removing benzene ring from quinoline moiety, lowers the absorption wavelength for dyes **1** and **2** compared to dyes **6** and **8** with the benzene ring attached to quinoline, respectively. Same trend goes to the quino dyes (**3–5**) where the benzene ring has been removed from the thiazolium moiety. QuinoN **3** and QuinoN-2 **5** absorb at lower wavelengths than dye **8** and similarly dye **4** at lower wavelength than dye **9**. Quite interestingly, dyes seem to have different peak shape depending on which arm they have. Thiol containing dyes (**4**, **7** and **9**) show a shoulder, a bit smoothed out in dye **7** but still visible which cannot be seen for amine dyes (**1–3**, **5**, **6**, **8**). Same trends were expected to be observed in emission spectra of all studied dyes.

Peaks are more overlapping in normalized emission spectra compared to absorption spectra above. Emission maxima range from

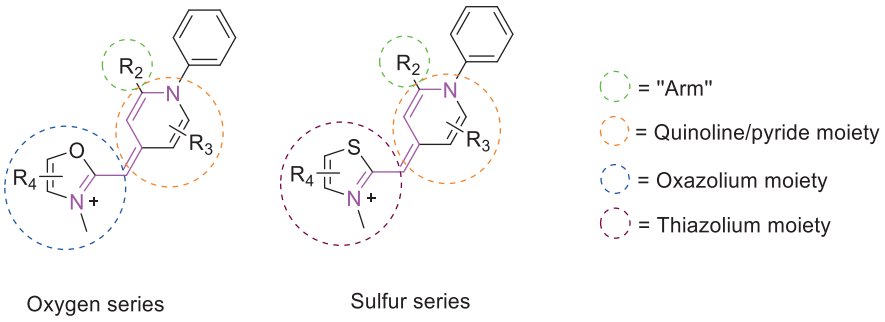

Fig. 1. Schematic picture of studied dyes with explanations for different structural moieties. The common fixed core skeleton found in all cyanine dyes is highlighted with magenta.

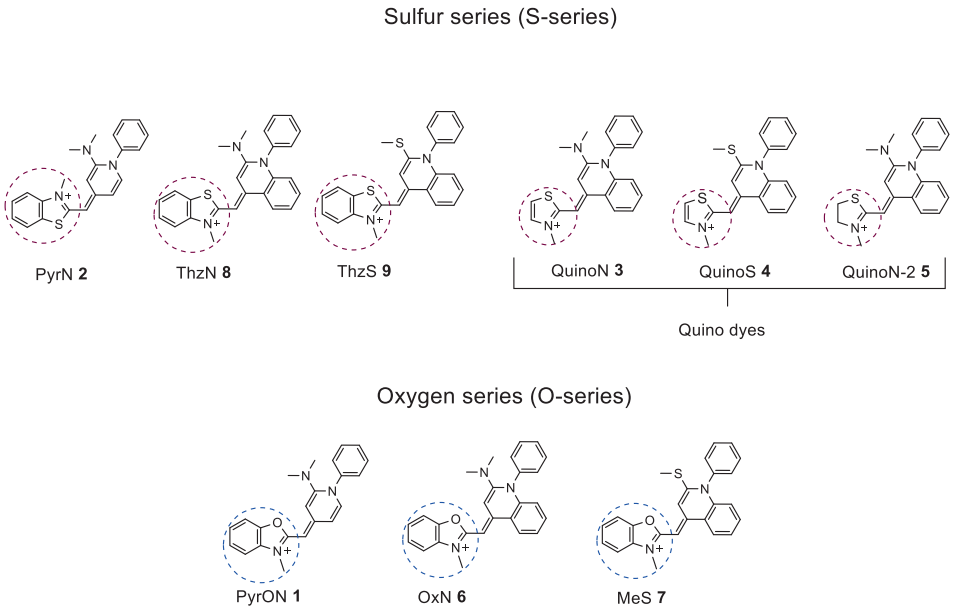

Fig. 2. Structures of newly synthesized (**1–5**) and previously published (**6–9**) [15], [17] dyes.

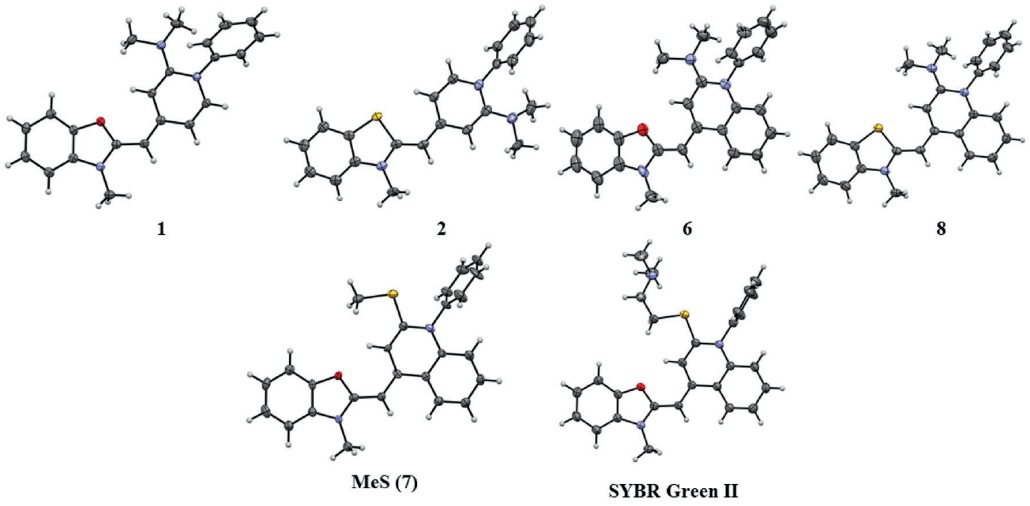

Fig. 3. The X-ray structures of dyes **1**, **2**, **6**, **8** (top) and the commercial dyes **MeS** and **SYBR Green II** (below). Anions and solvent molecules are omitted for clarity.

436 nm to 514 nm, a bit wider range compared to absorption maxima. In Fig. 4., same trends observed in absorbance plot can be seen; dyes with benzothiazolium moiety (**2**, **8**, **9**) emit at higher wavelengths compared to dyes with oxazolium moiety (**1**, **6**, **7**). As also observed in absorption spectra, dyes with thiol arm (**4**, **7**, **9**) emit at higher wavelengths compared to the amine dyes with otherwise same structure (**3**, **6**, **8**,). Removing benzene from either thiazolium or quinoline moiety lowers the emission wavelengths for studied dyes. Dyes **1** and **2** emit at lower wavelengths compared to dyes **6** and **8**. Similarly, Dye **4** emits a bit lower compared to compound **9**. Biggest difference between emission maxima when benzene have been removed can be seen for compound **5** compared to dye **8**. Dye **5** emits 44 nm lower than **8**, when second biggest difference between dyes **6** and **1** is 27 nm. Surprisingly, dye **3** emits 1 nm higher than compound **8** being the only exception to the trend observed. Line shapes for compounds **3** and **4** are not as smooth as other dyes due to low intensities even at high dye concentrations. To be able to understand how the dyes behave in more detailed manner series of titrations were performed to obtain molar absorption coefficients in various solvents.

Molar absorption coefficients, ε_{max}, were measured for each dye in three different solvents: TE buffer, ctDNA and ethanol. Ethanol was chosen as organic solvent to see if water solubility has effect in the absorption. Molar absorption coefficient is based on Beer-Lambert law:

$$A = \epsilon lc$$

Where ϵ = molar absorption coefficient, l = path length in cm (usually 1 cm) and c = concentration of the studied molecule. Hence, the molar absorption coefficient describes the correlation between the measured absorption and the concentration of the sample [19].

Absorption coefficients between studied dyes vary depending on the

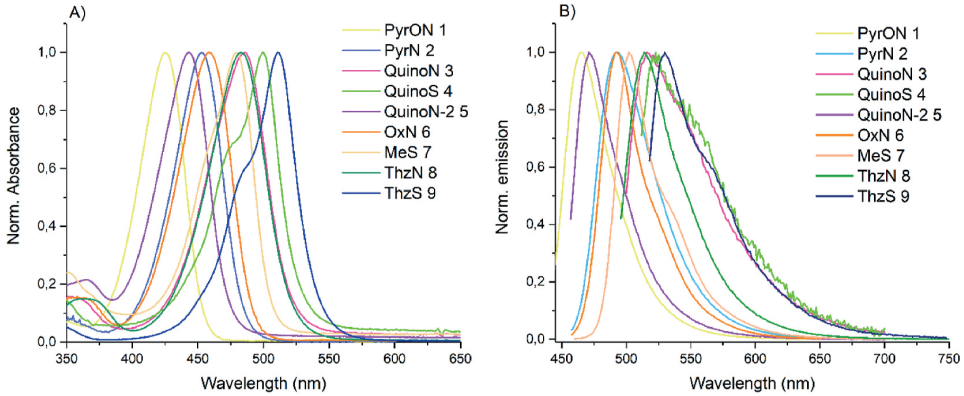

Fig. 4. A) Normalized absorptions of all dyes (**1–9**) in EtOH. B) Normalized emissions of all dyes (**1–9**) in 100 μM ctDNA solution. Dyes were excited with the excitation maxima unique to each dye: **1** at 436 nm, dye **2** at 463 nm, dye **3** at 492 nm, dye **4** at 505 nm, dye **5** at 449 nm, dye **6** at 464 nm, dye **7** at 487 nm, dye **8** at 488 nm and dye **9** at 514 nm.

structures and used solvents. From Table 1. no clear correlation can be seen between the dye's structures and the magnitude of absorption coefficients. All dyes, however, exhibit the highest absorption coefficients in ethanol. This indicates that when dyes are fully soluble in a certain solvent, the absorption enhances. Dyes **3** and **4** show the lowest absorption coefficients throughout the measurements regardless of the solvent. Compound **5** has two-folds higher values compared to dye **3** due to the missing double bond. Dyes **1** and **2** have similar absorption coefficient values compared to dyes **6** and **8**, the latter containing the benzene ring in pyridine moiety. When imagining biological samples, a clear difference between the excitation and emission maxima is preferred to avoid self-quenching of the emission peak. Hence Stoke's shifts were calculated and compared.

Stoke's shifts seemed to have a correlation to the structure of studied dyes. In the dyes **6–9** this correlation was already observed; dyes with thiol arm, **7** and **9** and also the new dye **4,** have smaller Stoke's shifts compared to the dyes with amine arm (**1–3, 5, 6, 8**). However, the Stoke's shifts of dyes **3** and **5** with amine arm are not significantly higher compared to dyes with thiol arms (**4**, **7** and **9**) but the overall trend can still be seen. Similar enhancement of Stoke's shift was also found by Zhang et al. [23] and Peng et al. [24] when replacing chloride by amine group. The same was also observed in our previous studies [15]. Together with the Stoke's shifts, quantum yield is an important way to evaluate fluorescent probes since it tells how much of the absorbed photons are emitted and therefore it can illuminate which dyes could be potentially strongly fluorescent.

Quantum yields of the dyes were evaluated by comparing them to the fluorescein standard. Dye **6** was determined to have a quantum yield of 100% and the new dye **1** is a match to it, also exhibiting a quantum yield of 100%. These compounds have similar structures, except for the absence of the benzene ring in the quinoline moiety in dye **1**. Therefore, similar result was expected for compound **2** when compared with dye **8**. Interestingly, quantum yield for dye **2** is 10% lower than compound **8** even though the only difference between these two structures is the benzene ring missing from the quinoline moiety. With these results, we expected to observe quantum yields in same region for Quino dyes (**3–5**) compared to similar dyes with benzene rings at thiazolium moiety. Surprisingly, removing the benzene from thiazolium moiety lowered the quantum yields severely, biggest difference being 65.3% between dyes **8** and **3**. This result indicates that the benzene ring at thiazolium moiety has important role to the dyes and their photophysical properties.

All studied dyes exhibit low background emission (see Fig. S21 and Fig. S22) in TE buffer without ctDNA presence. The best fluorescent enhancement was exhibited by dye **6**, of 1050 times, the similar value to commercially available dyes PicoGreen [13] and SYBR Green I [25]. Generally, fluorescent enhancements of the studied dyes were over 400 times for the dyes with the best quantum yields (over 50%) and similarly, dyes with poor quantum yield (lower than 15%), also exhibited lower fluorescent enhancement, maximum of under 300 times. Thus, the relation with the fluorescent increasement and quantum yield is noticeable. However, high quantum yield does not automatically mean high fluorescence enhancement, the dye **1** with quantum yield of 100% exhibited fluorescent enhancement only of 414 times due to the highest measured background emission. In order to get a more comprehensive understanding how useable probes the studied dyes are, also the brightness was determined for each dye.

Brightness was calculated for each dye to have a number describing their quality (complementing the molar absorption coefficient). Brightness is calculated by multiplying the molar absorption coefficient in the 100 μm ctDNA solution with the determined quantum yield. Dye **6** has the highest brightness, compound **1** being just a bit short with a brightness of 36100. Similarly, dye **2** is just a bit less bright than dye **8**.

Table 1
Spectral data measured from studied dyes, see Fig. S17.-Fig. S23. for related plots. Data for dyes **6–9** was taken from our previous article [15] to be compared with the dyes (**1**–**5**) here presented. Reported excitation maxima were used to record emission spectra and vice versa for each dye.

Dye	λ_{exc} (nm)	ε_{max} (TE Buffer)*	ε_{max} (EtOH)*	ε_{max} (100 μM ctDNA)*	λ_{emi} (nm)	Stoke's Shift (nm)	Φ (%)	Brightness ($M^{-1}cm^{-1}$)
PyrON **1**	436	59.4 ± 0.30	68.4 ± 0.50	36.1 ± 0.80	465	29	100	36100
PyrN **2**	463	40.3 ± 0.20	56.1 ± 0.14	30.8 ± 0.40	492	29	52.3	16000
QuinoN **3**	492	11.9 ± 0.12	19.7 ± 0.20	12.2 ± 0.02	516	24	2.8	431
QuinoS **4**	505	8.87 ± 0.14	14.4 ± 0.06	8.4 ± 0.10	523	18	2.2	264
QuinoN-2 **5**	449	22.5 ± 0.06	38.1 ± 0.30	20.1 ± 0.01	471	22	6.5	1310
OxN **6**	464	56.5 ± 0.80	73.6 ± 0.60	47.3 ± 0.20	492	28	100	47300
MeS **7**	487	16.0 ± 0.30	25.7 ± 0.30	18.0 ± 0.30	503	16	76.4	13800
ThzN **8**	488	47.53 ± 2.00	56.9 ± 0.30	36.5 ± 0.30	515	27	68.1	24900
ThzS **9**	514	35.3 ± 1.00	65.4 ± 1.10	49.1 ± 0.07	533	19	13.6	6700

*Unit for molar absorption coefficient in this table is $x10^3$ $M^{-1}cm^{-1}$

Quino dyes (**2–5**), however, show very low brightness compared to all other dyes. This result further indicated even that benzene ring at the thiazolium moiety has a key role in the structures since its remotion drastically lowers the brightness. However, the benzene ring can be removed from quinoline moiety without a major impact in the brightness. This could be due to the inductive effect of the benzene ring and positively charged nitrogen. Nitrogen with positive charge is an electron withdrawing group and hence it could withdraw electrons from the benzene ring to itself [26] When benzene donates electron density to the nitrogen, it could stabilize the positive charge of the nitrogen. However, the assignment of the local positive charge is uncertain since, based on the X-ray crystal structure studies, there is an indication of delocalization of this charge along the carbon chain between the two nitrogen atoms.

Next, the experimental observations of photophysical properties were compared to calculations. We used density functional theory (DFT) as implemented in code-package called GPAW and time-dependent density functional theory in linear response formalism (lr-TDDFT) to model the optical absorption spectra and excited state properties of the selected molecules [27] In all calculations we used real-space grids and Perdew-Burke-Ernzerhof (PBE) functional [28] Our calculations concentrated on two dyes from oxygen series: dyes **6** and **7** and one dye from sulfur series: dye **2**. Selected molecules comprise of higher and lower fluorescence efficiencies as well as have structural variation in the arm R_2 and in the R_3 and R_4 moieties. Calculated optical absorption spectra are shown in Fig. S26. In general, the calculated main peak positions (dye **6**, 417 nm; dye **7**, 431 nm; dye **2**, 399 nm), are systematically blueshifted by 0.3–0.4 eV as compared to experimental. Dye **2** absorbs with highest intensity at the shortest wavelengths from the three dyes whereas dye **7** absorbs at the longest wavelengths with the second highest intensity. Calculated absolute intensity of the weakest absorption peak of dye **6** is 83% of the strongest absorption of dye **2**. Despite of the systematic blueshift, the relative order of the peak positions is exactly the same as observed experimentally.

Emission properties were calculated by relaxing the excited states using finite differences method to the excited state energy within the lr-TDDFT framework. Excited states for the relaxation were selected based on the main absorption peak. Root mean square deviation (RMSD) per atom between optimized excited state and ground state structures is seen to be in a range of 0.083 Å - 0.108 Å, which means that all structures are rather static as visualized in Fig. S27. By visual inspection it can be noticed that there is slightly more out-of-plane deviation in the positions of the atoms in the excited state structures compared to ground state, but the differences are very small. Oscillator strengths of the lowest energy transitions of the relaxed excited states were then plotted as Gaussian broadened curves to mimic the emission spectrum which is visualized in Fig. S28. In contrary to the blueshift of the absorption peaks, the positions of the calculated emission peaks (dye **6**, 494 nm; dye **7**, 482 nm; dye **2**, 504 nm) are very close to the experimental (dye **6**, 492 nm; dye **7**, 503 nm; dye **2**, 493 nm). Remarkably, the absolute intensity of the emission peak of the dye **2** is 4–5 times lower than for dye **6** and **7**. This difference is in qualitative agreement with the experimental observed differences in fluorescence behavior, for example, the brightness. Calculated spectrum of dye **7** shows also a shoulder next to the main emission peak as observed in the experiments. Due to the systematic blueshift in the absorption peaks, also the calculated Stoke's shifts get radically overestimated, but their order is again the same as in the experiments, *i.e.*, compound **7** gives the largest and **2** clearly the lowest Stoke's shift from the three selected dyes. These calculated results give qualitative support to experiments and confirm observed trends in photophysical properties with respect to the structural modifications. Since the experimental and calculated emission and absorbance spectra were similar with only systematic shifts, the relationship between the dyes and ctDNA was studied even further by determining the binding parameters.

McGheen Von Hippel equation [20] was used to estimate binding constant (K_a) and binding site size (n) for each dye. Binding modes between the dyes and DNA were studied by measuring emission in two different ctDNA solutions, in excess ctDNA and 0.52 μM ctDNA solution. Then this data was plotted using the McGhee Von Hippel equation. From the binding constant K_a, dissociation constant (K_d) can be calculated which can be further used to calculate Gibbs free energies (ΔG°) for the dyes. Results for K_a, K_d and ΔG° are presented in Table 2. Theory and application of this equation have been presented in a more detailed manner in an article published by our group [17].

Surprisingly results from McGhee Von Hippel plots show noticeable variation between studied dyes. Interestingly, dyes **3** and **4** which showed poor emission throughout the measurements, seem to bind tightly with DNA since the binding constants, K_a, for both compounds are in the same region as dye **6**, exhibiting strong emission with DNA. Also worth noting is the decrease in binding constant from $7.7 \times 10^6\ M^{-1}$ to $2.2 \times 10^6\ M^{-1}$ when the double bond from compound **3** is removed to get compound **5**. Dyes **3** and **4** have much smaller bindings site sizes compared to other new dyes, **1**, **2** and **5**. The binding site is two sizes larger for compounds **2** and **5** and four sizes larger for dye **1** when compared to the dyes **3** and **4**. This result would suggest that these dyes bind differently to the DNA. Dyes **6–9** show clear correlation between the binding constant and the brightness; dyes with higher binding constant, also showed better brightness, which is not observed for the dyes **1–5**. Interestingly dyes with low brightness (**3–5**) exhibit strong binding with DNA but they are not as emissive as dyes with looser binding. Compounds **1** and **2** have low binding constants, but they are still very emissive and are brighter than, for example, dye **7**. The latter exhibits two times higher binding constant compared to compound **2** and almost four times higher than dye **1**. Dyes **1**, **2** and **5** have lower binding constants, and they take effectively more space in binding sites compared to other dyes indicating that they do not bind as tightly to the DNA as for example dye **6**. As discussed in introduction, interaction mode between SYBR green related dyes and nucleic acids is described by the intercalation of quinoline moiety between the base pairs and the thiazolium moiety interacting with phosphate groups of the nucleic acids [13] or by the whole dye binding with the minor groove of the DNA [14]. Removing the benzene ring from the quinoline moiety makes the intercalator part and the whole molecule smaller; hence it might get too small to the binding site making it twist and escape the site more easily. Removing the benzene from thiazolium moiety seem to increase the binding constant if the double bond is kept. Dye **5**, however, requires much more space and has a weaker DNA binding, due to the missing double bond in the thiazolium moiety.

Two of the best dyes, **1** and **6** were selected for further studies with cellular RNA to prove that these monomethine cyanine dyes can be used to image both DNA and RNA.

Both dyes **1** and **6** do emit when bound to RNA. The intensity of dye **1** in complex with RNA is noticeably lower compared to its intensity when bound to DNA as shown in Fig. 5. Only very slight lowering of intensity can be observed for dye **6** when bound to DNA as compared to RNA. Emission maxima of dye **6** shifts from 492 nm to 496 nm in RNA solution. Interestingly, dye **6** shows a two-fold increase in intensity when

Table 2
Binding related data based on McGhee Von Hippel equation [20] (see Fig. S24 and Fig. S25. for related plots).

Dyes	Ka ($x10^6\ M^{-1}$)	Kd (nM)	n	ΔG^0 (kJ/mol)
PyrON **1**	1.2 ± 0.40	850	6.8 ± 0.30	−34.1
PyrN **2**	2.3 ± 0.20	441	4.2 ± 0.05	−35.7
QuinoN **3**	7.7 ± 0.20	129	1.9 ± 0.01	−38.8
QuinoS **4**	8.0 ± 0.90	124	1.7 ± 0.04	−38.9
QuinoN-2 **5**	2.2 ± 0.20	447	4.0 ± 0.20	−35.8
OxN **6**	8.5 ± 1.50	118	3.4 ± 0.40	−39.0
MeS **7**	4.6 ± 1.00	218	1.6 ± 0.04	−37.5
ThzN **8**	5.8 ± 0.40	171	2.1 ± 0.12	−38.1
ThzS **9**	2.3 ± 0.04	441	1.7 ± 1.00	−38.1

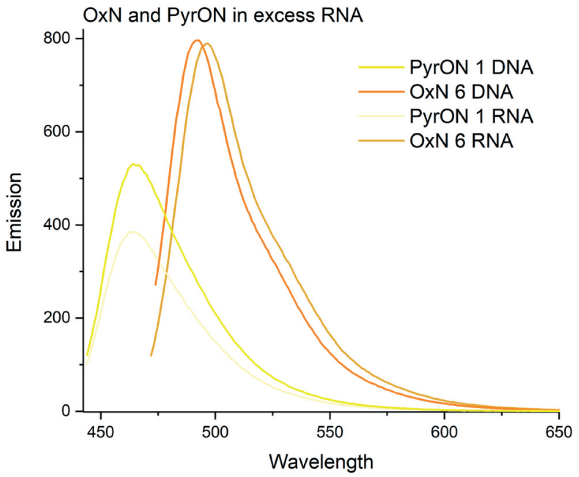

Fig. 5. Dyes **1** and **6** in excess cellular RNA in TE buffer solution. Dye concentrations were 0.3 μM for all four measurements. Dye **1** was excited at 436 nm and dye **6** at 464 nm.

bound to RNA compared to dye **1**, the only difference being the presence/absence of the benzene ring from the quinoline moiety. Both dyes **1** and **6** are suitable for both DNA and RNA detection.

3.3. Binding mode prediction and dynamics of DNA-dye complexes

In order to identify the specific DNA-dye interactions, molecular docking calculations were performed for dyes 2, 6, and 7. As observed in Fig. 6., all three dye molecules bind to AT-rich minor groove with calculated binding energies of −10.58 ± 0.04, −8.65 ± 0.57, and −8.88 ± 0.03 kcal/mol (average of ten lowest energy conformations; see Fig. S29) for dye 2, 6, and 7, respectively. The main contacts established between the dye molecules and nucleotides were lone pair–π, hydrogen bonds, and sulfur–π interactions (Fig. 6.). In all complexes, the heteroatom from the oxa/thia moiety is observed inside the minor groove; however, this atom contributes to the binding affinity only in dye 2. In contrast, in dyes 6 and 7, the interaction with the nucleotides is formed through the R3 ring, which also tends to be inside (Fig. 6).

As a further step, we investigated the dynamics of the (fully flexible) complexes in explicit solvent by mimicking the experimental conditions to see if the DNA somehow induces a rigidity of dye molecules after complex formation. Molecular dynamics (MD) simulations showed the same binding site observed in docking calculations. The orientation of the dye molecules is parallel to the DNA strands throughout each MD simulation, and no intercalation between the base pairs is observed (see Supplementary Videos). Even though the dye molecules explore different regions of the DNA, they prefer to stay in the minor groove where the more significant interactions are stacking contacts (Fig. S30). The rigidity increases significantly (10–20 times) when dye molecules are bound to DNA compared to their free form, as shown in RMSD plots (Fig. 7). And more importantly, our results suggest that the movement restriction in the binding region as a result of this rigidity could be crucial for improving the brightness of the dyes. This is illustrated in Fig. 7, where the center of mass motion of the different dyes along the DNA shows a different binding site flexibility. Although dye 6 showed the lowest calculated binding affinity (from rigid docking), its behavior under more dynamic conditions shows that it is capable of forming the most stable complex with a low degree of fluctuation over the simulated period, which might explain the highest fluorescence observed experimentally.

Supplementary video related to this article can be found at https://doi.org/10.1016/j.dyepig.2022.110844

4. Conclusions

Five new cyanine dyes (**1**–**5**) were synthesized and their photophysical properties were compared to previously published dyes (**6**–**9**) to gain a deeper understanding of which structural changes make these dyes better fluorescent probes for nucleic acids. Measured data clearly shows that a benzene ring at the thiazolium moiety plays a key role, and removing it lowers the brightness of the dyes drastically, making them too weak to be useable. This is not the case for removing a benzene ring from the quinoline moiety since it does not affect the brightness as strongly. As already discussed earlier [15] dyes with an oxazolium moiety or dimethylamine arm were brighter compared to dyes with thiazolium moiety or with methanethiol substituent. The molar absorption coefficients, which are used to determine how bright the dyes are, were the highest for each dye in ethanol suggesting that when dyes are fully solubilized their brightness is maximized. Hence enhancing water solubility could be one pathway to brighter dyes. Interestingly, the molecular docking calculations to identify the specific DNA-dye interactions showed that dye molecules **2**, **6** and **7** bind to the AT-rich minor groove and the main contacts established between the dye molecules and nucleotides were lone pair–π, hydrogen bonds, and sulfur–π

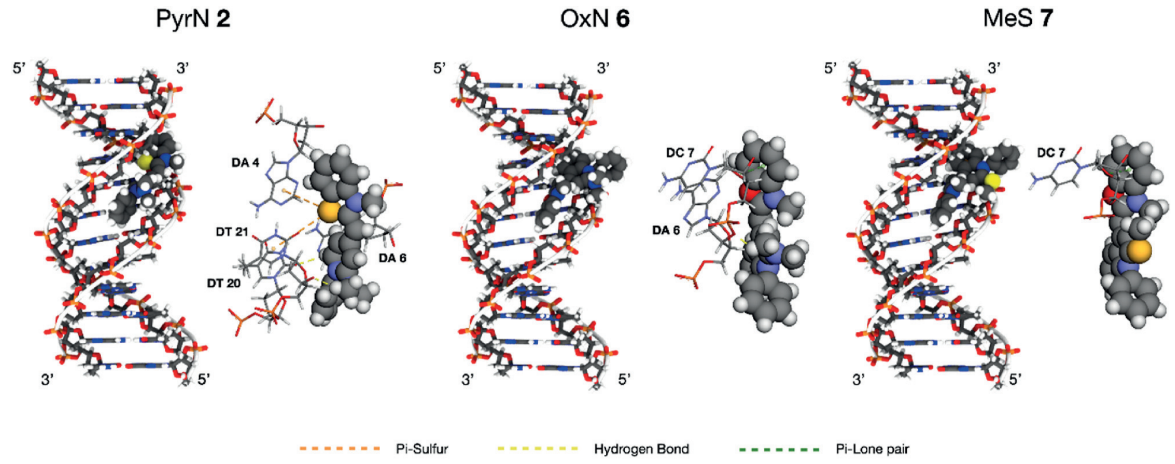

Fig. 6. Best docked conformations of PyrN **2**, OxN **6**, and MeS **7** dyes bound to B-DNA. For each complex, a full view of the binding site (left) and the main interactions established with nucleotides (right) are shown.

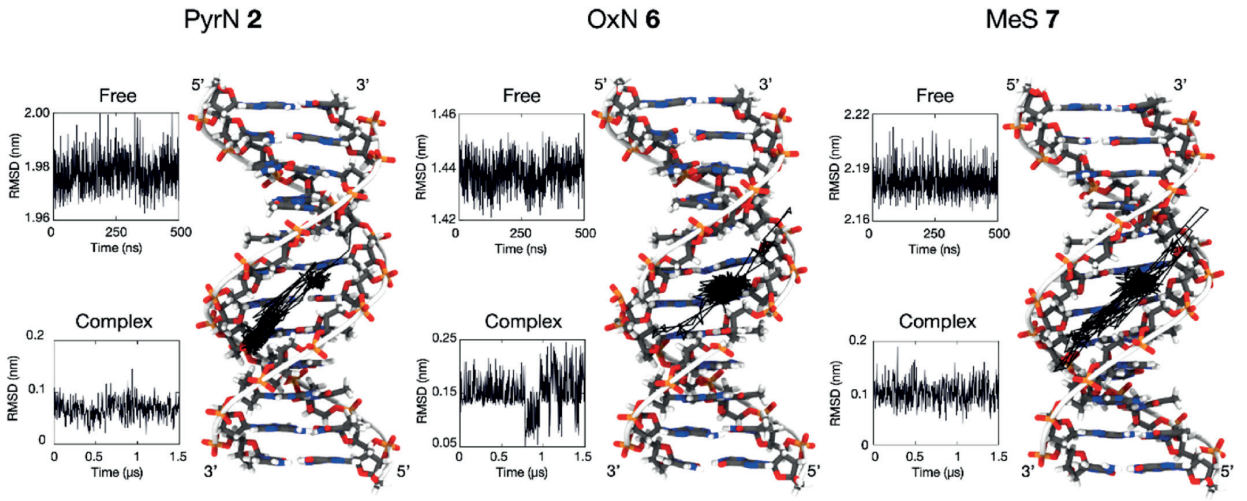

Fig. 7. Root mean square deviation (RMSD) of PyrN **2**, OxN **6**, and MeS **7** dyes in free form and in complex with B-DNA during simulated time. Black lines inside the B-DNA fragments represent the center of mass motion of the different dyes along the strands during the 1.5-μs MD simulation.

interactions. The structures **1**, **2**, **6**, **8** and **10** (due to a mixed composition, **10**, was not included in the photophysical studies) were determined by single crystal X-ray crystallography.

Our results give valuable information on how different structural modifications around the fixed fluorophore skeleton changes the nature and performance of these dyes. This information is crucial when new dyes are designed to obtain great brightness along with other desired traits such as better water solubility or even selectivity between DNA and RNA. The dyes discussed herein are currently being investigated with respect to their biological applications, including visualizing the virus uncoating in cells.

CRediT authorship contribution statement

Johanna M. Alaranta: Writing – original draft, Data curation, Formal analysis, Investigation. **Khai-Nghi Truong:** Data curation, Formal analysis, Investigation. **María Francisca Matus:** Writing – original draft, Data curation, Formal analysis, Investigation. **Sami A. Malola:** Writing – original draft, Data curation, Formal analysis, Investigation. **Kari T. Rissanen:** Writing – original draft, Data curation, Formal analysis, Investigation, Funding acquisition. **Sailee S. Shroff:** Data curation, Formal analysis, Writing, Investigation. **Varpu S. Marjomäki:** Data curation, Formal analysis, Writing, Investigation, Funding acquisition. **Hannu J. Häkkinen:** Writing – original draft, Investigation, Funding acquisition. **Tanja M. Lahtinen:** Writing – original draft, Data curation, Formal analysis, Investigation, Funding acquisition, Project administration.

Declaration of competing interest

The authors declare that they have no known competing financial interests or personal relationships that could have appeared to influence the work reported in this paper.

Data availability

No data was used for the research described in the article.

Acknowledgements

This work was supported by the Academy of Finland [342251 to V. M. and S.S., and 319208 to H.H.] and the University of Jyväskylä. Authors thank Dr. Tatu Kumpulainen for his assistance with the photophysical studies. Dr. Ville Saarnio is thanked for the fruitful discussions. Dr. James Ward is thanked for proofreading.

Appendix A. Supplementary data

Supplementary data to this article can be found online at https://doi.org/10.1016/j.dyepig.2022.110844.

References

[1] Shi H, Tan X, Wang P, Qin J. A novel near-infrared trifluoromethyl heptamethine cyanine dye with mitochondria-targeting for integration of collaborative treatment of photothermal and sonodynamic therapy. Mater Today Adv 2022;14:100251. https://doi.org/10.1016/j.mtadv.2022.100251.
[2] Wangngae S, Chansaenpak K, Weeranantanapan O, Piyanuch P, Sumphanapai T, Yamabhai M, et al. Effect of morpholine and charge distribution of cyanine dyes on cell internalization and cytotoxicity. Sci Rep 2022;12. https://doi.org/10.1038/s41598-022-07533-5.
[3] Li S, Wu Y, Liu S, Wu T, Liu G, Li T, et al. A multifunctional platinum(iv) and cyanine dye-based polyprodrug for trimodal imaging-guided chemo-phototherapy. J Mater Chem B 2022;10:1031–41. https://doi.org/10.1039/d1tb02682h.
[4] Ratto F, Magni G, Aluigi A, Giannelli M, Centi S, Matteini P, et al. Cyanine-doped nanofiber mats for laser tissue bonding. 2022. https://doi.org/10.3390/nano12091613.
[5] Liu L, Shi L, Liu J yong, wei Yang D, Fu Y, ying Ma X, et al. A cysteine and Hg2+ detection method based on transformation supramolecular assembly of cyanine dye by AGRO100. Spectrochim Acta Mol Biomol Spectrosc 2022;270:120779. https://doi.org/10.1016/j.saa.2021.120779.
[6] Heing-Becker I, Achazi K, Haag R, Licha K. Hydroquinone-functionalized cyanine dye as reduction-sensitive probe for imaging of biological reducing species. Dyes Pigments 2022;201:110198. https://doi.org/10.1016/j.dyepig.2022.110198.
[7] Aristova D, Kosach V, Chernii S, Slominsky Y, Balanda A, Filonenko V, et al. Monomethine cyanine probes for visualization of cellular RNA by fluorescence microscopy. Methods Appl Fluoresc 2021;9. https://doi.org/10.1088/2050-6120/AC10AD.
[8] Fei X, Gu Y. Progress in modifications and applications of fluorescent dye probe. Prog Nat Sci 2009;19:1–7. https://doi.org/10.1016/j.pnsc.2008.06.004.
[9] Shindy HA. Fundamentals in the chemistry of cyanine dyes: a review. Dyes Pigments 2017;145:505–13. https://doi.org/10.1016/j.dyepig.2017.06.029.
[10] Armitage BA. Cyanine dye–nucleic acid interactions. Top Heterocycl Chem 2008;14:11–29. https://doi.org/10.1007/7081_2007_109.
[11] Kristinai L, Henary M. Cyanine dyes containing quinoline moieties: history, Synthesis, optical properties, and applications. Chem Eur J 2021;27:4230–48. https://doi.org/10.1002/chem.202003697.
[12] Mizuno Y, Watanabe K. Syntheses of cyanine dyes. Yakugaku Zasshi 1948;68:250–2. https://doi.org/10.1248/yakushi1947.68.7-9_250.
[13] Dragan AI, Casas-Finet JR, Bishop ES, Strouse RJ, Schenerman MA, Geddes CD. Characterization of PicoGreen interaction with dsDNA and the origin of its fluorescence enhancement upon binding. Biophys J 2010;99:3010–9. https://doi.org/10.1016/J.BPJ.2010.09.012.

[14] Karlsson HJ, Eriksson M, Perzon E, Kerman AÊ, Westman G. Groove-binding unsymmetrical cyanine dyes for staining of DNA: syntheses and characterization of the DNA-binding. Nucleic Acids Res 2003;31:6227–34. https://doi.org/10.1093/nar/gkg821.
[15] Saarnio VK, Alaranta JM, Lahtinen TM. Systematic study of SYBR green chromophore reveals major improvement with one heteroatom difference. J Mater Chem B 2021;9:3484–8. https://doi.org/10.1039/d1tb00312g.
[16] Ying L. Nucleic acid detections and methods of their use. 2013. 2013/0137875.
[17] Saarnio VK, Salorinne K, Ruokolainen VP, Nilsson JR, Tero TR, Oikarinen S, et al. Development of functionalized SYBR green II related cyanine dyes for viral RNA detection. Dyes Pigments 2020;177:108282. https://doi.org/10.1016/j.dyepig.2020.108282.
[18] Karlsson HJ, Bergqvist MH, Lincoln P, Westman G. Syntheses and DNA-binding studies of a series of unsymmetrical cyanine dyes : structural influence on the degree of minor groove binding to natural DNA. Bioorg Med Chem 2004;12:2369–84. https://doi.org/10.1016/j.bmc.2004.02.006.
[19] IUPAC. Compendium of chemical terminology. In: The "Gold Book"). Compiled by A. D. McNaught and A. Wilkinson. second ed. Oxford: Blackwell Scientific Publications; 1997. Online version (2019-) created by S. J. Chalk., n.d.
[20] McGhee JD, von Hippel PH. Theoretical aspects of DNA-protein interactions: Co-operative and non-co-operative binding of large ligands to a one-dimensional homogeneous lattice. J Mol Biol 1974;86:469–89. https://doi.org/10.1016/0022-2836(74)90031-X.
[21] Brouwer AM. Standards for photoluminescence quantum yield measurements in solution (IUPAC technical report). Pure Appl Chem 2011;83:2213–28. https://doi.org/10.1351/PAC-REP-10-09-31.
[22] Benson RC, Kues HA. Absorption and fluorescence properties of cyanine dyes. J Chem Eng Data 1977;22:379–83. https://doi.org/10.1021/je60075a020.
[23] Zhang J, Moemeni M, Yang C, Liang F, Peng W-T, Levine BG, et al. General strategy for tuning the Stokes shifts of near infrared cyanine dyes. J Mater Chem C 2020;8:16769. https://doi.org/10.1039/d0tc03615c.
[24] Peng X, Song F, Lu E, Wang Y, Zhou W, Fan J, et al. Heptamethine cyanine dyes with a large Stokes shift and strong fluorescence: a paradigm for excited-state intramolecular charge transfer. J Am Chem Soc 2005;127:4170–1. https://doi.org/10.1021/JA043413Z.
[25] Dragan AI, Pavlovic R, McGivney JB, Casas-Finet JR, Bishop ES, Strouse RJ, et al. SYBR Green I: fluorescence properties and interaction with DNA. J Fluoresc 2012;22:1189–99. https://doi.org/10.1007/s10895-012-1059-8.
[26] Smith JG. Organic chemistry. fourth ed. New York: McGraw-Hill Education; 2014.
[27] Enkovaara J, Rostgaard C, Mortensen JJ, Chen J, Dułak M, Ferrighi L, et al. Electronic structure calculations with GPAW: a real-space implementation of the projector augmented-wave method. J Phys Condens Matter 2010;22:253202. https://doi.org/10.1088/0953-8984/22/25/253202.
[28] Perdew JP, Burke K, Ernzerhof M. Generalized gradient approximation made simple. Phys Rev Lett 1996;77:3865–8. https://doi.org/10.1103/PhysRevLett.77.3865.

III

TAILORING THE INTERACTION BETWEEN A GOLD NANOCLUSTER AND A FLUORESCENT DYE BY CLUSTER SIZE: CREATING A TOOLBOX OF RANGE-ADJUSTABLE PH SENSORS

by

Pyo, K., Matus, M. F., Malola, S., Hulkko, E., Alaranta, J., Lahtinen, T., Häkkinen, H. & Pettersson, M. 2022

Nanoscale Advances, 4, 4579-4588.

https://doi.org/10.1039/D2NA00487A

Nanoscale Advances

ROYAL SOCIETY OF CHEMISTRY

PAPER

View Article Online
View Journal | View Issue

Cite this: *Nanoscale Adv.*, 2022, **4**, 4579

Tailoring the interaction between a gold nanocluster and a fluorescent dye by cluster size: creating a toolbox of range-adjustable pH sensors†

Kyunglim Pyo,[a] María Francisca Matus,[b] Sami Malola,[b] Eero Hulkko,[a] Johanna Alaranta,[a] Tanja Lahtinen,*[a] Hannu Häkkinen*[ab] and Mika Pettersson*[a]

We present a novel strategy for tailoring the fluorescent azadioxatriangulenium (KU) dye-based pH sensor to the target pH range by regulating the pK_a value of the gold nanoclusters. Based on the correlation between the pK_a and surface curvature of ligand-protected nanoparticles, the pK_a value of the gold nanoclusters was controlled by size. In particular, three different-sized *para*-mercaptobenzoic acid (*p*-MBA) protected gold nanoclusters, $Au_{25}(p\text{-MBA})_{18}$, $Au_{102}(p\text{-MBA})_{44}$, and $Au_{210-230}(p\text{-MBA})_{70-80}$ were used as the regulator for the pH range of the KU response. The negatively charged gold nanoclusters enabled the positively charged KU to bind to the surface, forming a complex and quenching the fluorescence of the KU by the energy transfer process. The fluorescence was restored after adjusting the surface charge of the gold nanocluster by controlling the solution pH. In addition, the KU exhibited a significantly different pH response behaviour for each gold nanocluster. $Au_{210-230}(p\text{-MBA})_{70-80}$ showed a higher pH response range than $Au_{102}(p\text{-MBA})_{44}$, which was intuitive. However, $Au_{25}(p\text{-MBA})_{18}$ showed an unexpectedly high pH response behaviour. pK_a titration measurement, molecular dynamics simulations, and essential dynamics analysis showed that small nanoclusters do not follow the scaling between the curvature and the pK_a value. Instead, the behaviour is governed by the distribution and interaction of *p*-MBA ligands on the nanocluster surface. This work presents an effective design strategy for fabricating a range adjustable pH sensor by understanding the protonation behaviour of the ultrasmall gold nanoclusters in an atomic range.

Received 27th July 2022
Accepted 21st September 2022

DOI: 10.1039/d2na00487a

rsc.li/nanoscale-advances

Introduction

Due to the connection between the pH and many chemical processes, pH measurement plays a vital role in a broad range of applications, such as environmental, industrial, chemical, and biomedical fields.[1–4] For that reason, enhancing the accuracy of the pH measurement and fabricating a suitable pH sensor has become an essential task in scientific research. Especially for intracellular pH measurements, it is crucial to develop a highly sensitive method to measure the small pH changes in a wide pH range. Intracellular pH controls cellular processes such as cell metabolism, apoptosis, and proliferation, making it extremely important to be strictly regulated in organelles.[5–10] Even a small pH change could dramatically trigger an inappropriate cell function, as observed in some common diseases such as cancer and Alzheimer's.[11,12]

Optical pH sensors have many advantageous properties, such as ease of transport, need for low concentration of the pH indicator, high sensitivity and spatial resolution, and the non-invasive nature. Fluorescence-based indicators such as organic dyes have been the most studied materials for optical sensors because of their high sensitivity and brightness.[13–16] However, despite these merits, they suffer from poor solubility, low photobleaching resistance, and a lack of understanding of the behaviour towards harsh environments.[17,18] Moreover, the pH detection range for the pH-sensitive fluorophore only covers two pH units. This range depends on the acid dissociation constant (K_a), which gives a sigmoidal curve in a pH range of pK_a ±1. Because of these limitations, the pH-sensitive fluorophores are not ideal for general pH measurements alone, and additional modifications are needed for further use.

There have been some attempts to overcome these limitations by modifying the structure of the dye to adjust the pH range[19,20] or functionalizing various pH indicators (*e.g.*, using large nanoparticles as carriers), which have different pH detection ranges to widen the pH range of the sensor.[21,22] For

[a]*Department of Chemistry, Nanoscience Centre, University of Jyväskylä, P. O. Box 35, FI-40014, Finland. E-mail: mika.j.pettersson@jyu.fi*

[b]*Department of Physics, Nanoscience Centre, University of Jyväskylä, P. O. Box 35, FI-40014, Finland*

† Electronic supplementary information (ESI) available. See https://doi.org/10.1039/d2na00487a

example, Benjaminsen *et al.* have formed a triple-labeled sensor with a pH measurement range of 3.2–7.0, composed of two pH-sensitive fluorophores with different pK_a values and a nanoparticle as a carrier.[22] These pH sensors have a more extensive pH detection range, brighter fluorescence signals, higher photostability, and easier functionalization, which provides the opportunity to introduce various strategies to fabricate fluorescent pH sensors. However, there were still drawbacks to this method. The water solubility of the dye-functionalized nanoparticles would decrease with an increasing number of aromatic dyes, and thus the level of functionalization has to be a compromise between the function and the solubility. Moreover, the fabrication method differs for each dye which will intricate the synthesis steps, lower the yield, and reproducibility of the final product with the exact composition of the dyes. Therefore, it is crucial to distinctly understand the materials' properties before and after forming the sensors when designing a pH sensor. Furthermore, developing a method to freely control the pH range of the sensor with the least number of ingredients is significantly needed.

In our previous report,[23] we fabricated a fluorescent pH sensor by covalently binding a pH-independent dye (azaoxotriangulenium dye, KU) with an atomically precise and a water-soluble gold nanocluster (Au_{102}(*p*-MBA)$_{44}$; *p*-MBA = *para*-mercaptobenzoic acid) to create a functional hybrid material for intracellular pH imaging in live cells. The gold nanoclusters act as both nanocarriers and regulators of the fluorescence intensity in the targeted live cells. In acidic conditions, the dye-nanocluster hybrid is dissociated *via* hydrolysis of the ester bond. However, the dye and the nanocluster form a complex by weak interactions, which leads to quenching of fluorescence *via* Förster type of energy transfer. Simultaneously, local pH changes also influence the surface charge of the *p*-MBA ligand of the gold nanoclusters, which modifies the strength of the electrostatic interaction between the dye and the nanocluster, adjusting the extent of fluorescence quenching. Furthermore, the pH dependency behaviour of the dissociated KU dye and gold nanoclusters follows the gold nanoclusters' protonation behaviour, showing a more comprehensive pH range than other pH indicators. In other words, the functionality of the KU response on pH is tailored by nanoclusters with a different protonation behaviour.

In this report, we present a novel strategy for regulating the nanocluster's pK_a value to tailor the KU dye-based pH sensor to the target pH range. As a starting point, the pK_a value is known to be dependent on the surface curvature of the nanoclusters.[24–26] Large-sized nanoclusters have a low curvature surface, leading to a more densely packed ligand distribution. Because of the negative charge of the ligands and the short distance between the ligands, electrostatic repulsion between the ligands grows stronger. To reduce the repulsion between the ligands, the acid–base equilibrium of the ligands tends to shift to a higher pH and protonate the natively charged groups. Consequently, the pK_a of the large-size nanocluster shifts to a higher pH.

We used Au_{25}(*p*-MBA)$_{18}$, Au_{102}(*p*-MBA)$_{44}$, and $Au_{210-230}$(*p*-MBA)$_{70-80}$ (referred further on as Au_{250}(*p*-MBA)$_n$)[27] as the regulator for the pH range of the KU response. First, a complex of gold nanocluster and the KU dye was formed in an alkaline solution. Then the pH response of the KU was measured by lowering the pH by adding an acid. Three different nanoclusters showed significantly different response behaviours. Furthermore, the pK_a of each nanocluster was measured by the acid–base titration measurement. The Au_{102}(*p*-MBA)$_{44}$ and Au_{250}(*p*-MBA)$_n$ showed an intuitively correct difference in the pK_a value, while Au_{25}(*p*-MBA)$_{18}$ exhibited an unexpected pK_a value. Therefore, to understand the unique pK_a shift behaviour of Au_{25}(*p*-MBA)$_{18}$, molecular dynamics (MD) simulations and essential dynamics (ED) analysis were carried out to compare the structural difference of the ligand surface between the small and large nanoclusters. The results showed that small nanoclusters do not follow the scaling between the curvature and the pK_a but the behaviour is governed by the distribution and interaction of *p*-MBA ligands on the nanocluster surface. This is the first study attempting to analyse the pK_a value of ultrasmall nanoclusters and pinpoint what regulates the protonation behaviour in an atomic range. By understanding the pK_a trend of each nanocluster, it is possible to easily design or modify the pH sensor by tailoring the nanocluster size. Furthermore, the use of atomically precise nanoclusters facilitates synergy between theory and experiments toward paving the way for the rational design of new probes.

Experimental

Materials

Gold(III)chloride trihydrate ($HAuCl_4 \cdot 3H_2O$, ≥99.9%), *para*-mercaptobenzoic acid (*p*-MBA, 99%), sodium borohydride ($NaBH_4$, 99%), and ammonium persulfate (APS, ≥98%) were purchased from Sigma-Aldrich (Merck). Hydrochloric acid (HCl, 37%) and methanol (MeOH, 99.9%) were purchased from Honeywell. Acrylamide/bisacrylamide (bio reagent, 30%) was purchased by Bio-Rad. Sodium hydroxide (NaOH, ≥98.5%) was purchased from VWR Internationals, and etax Aa (anhydrous ethanol, 99.5%) was purchased from Anora Industrial. Glycerol (99.5%) was purchased from VWR BDH Prolabo. Carbon monoxide (CO, 99.9%) was purchased from Messer Griesheim. The 10× TBE (Tris–borate–EDTA) buffer for the PAGE separation was homemade with Trizma base (≥99%), borate (99%), and ethylenedinitrilotetraacetic acid (EDTA, pH 8.0). The solution was sterilized before use. Water was purified by using a Millipore Elix Essential 3 UV water purification system (15 MΩ cm). The azaoxotriangulenium dye (KU) used in the complex studies was obtained as a courtesy of Thomas Just Sørensen and Bo W. Larsen from the University of Copenhagen and was used without further modifications. All the chemicals were used as received without further purification.

Methods

UV-vis absorption and photoluminescence spectra of the synthesized gold nanoclusters and KU dye were collected with Horiba AquaLog spectrophotometer. Sample solutions were measured at ambient conditions using quartz fluorescence

cuvettes from Hellma. Fluorescence emission spectra were measured after exciting the sample at 500 nm wavelength.

Transmission electron microscopy (TEM) samples were prepared by drop-casting 2 μL of the aqueous solution of clusters on a glow discharged 400 mesh lacey carbon copper grid (01824, Ted Pella). The solution was let to adsorb for 10 min, after which the excess sample was removed and washed with water and methanol. The grids were allowed to dry for more than 2 h at room temperature before imaging. $Au_{25}(p\text{-MBA})_{18}$ was measured with 120 kV high voltage, $Au_{102}(p\text{-MBA})_{44}$ and $Au_{250}(p\text{-MBA})_n$ were measured with 80 kV high voltage. All samples were imaged with JEOL electron microscope (JEM-1400). The size of the nanoclusters was analysed by using ImageJ. The isolated gold nanoclusters were run through polyacrylamide gel electrophoresis (PAGE) by Mini-PROTEAN Tetra Cell (Bio-Rad) to verify the purity of the prepared samples. The PAGE was run on homemade 15% polyacrylamide gel (29 : 1 acryl-amide : bisacrylamide) using a 1× TBE run buffer at 130 V for 2 h. The PAGE gel was imaged using an iPhone 13 pro camera.

Synthesis of gold nanoclusters ($Au_{25}(p\text{-MBA})_{18}$, $Au_{102}(p\text{-MBA})_{44}$, $Au_{250}(p\text{-MBA})_n$)

$Au_{102}(p\text{-MBA}_{44})$ and $Au_{250}(p\text{-MBA})_n$ were obtained by following a previously published procedure.[27,28] $Au_{25}(p\text{-MBA})_{18}$ was synthesized by a reported protocol with minor modifications.[29] In a typical synthesis, 50 mM $HAuCl_4 \cdot 3H_2O$ (5 mL) and 50 mM *p*-MBA aqueous solution (in 10 mL of 150 mM NaOH) were added into 235 mL of ultrapure water in a 500 mL Erlenmeyer flask during vigorous stirring. After stirring for 10 min, the pH of the solution was adjusted to 11.0 by adding 1 M NaOH aqueous solution, which made the solution turn clear yellow. After stirring for 30 min, CO gas was bubbled into the reaction mixture for 2 min (1 bar) for reduction. The reaction was kept air-tight for more than 3 days under stirring until the solution showed a reddish-brown colour. Before further process, the bulk solution was observed with UV-vis spectra to verify the existence of $Au_{25}(p\text{-MBA})_{18}$ in the solution. The product solution was then rotary evaporated to near dryness (water bath 40 °C). After that, 15 mL water was added to dissolve the dried product. Then 15 mL of ethanol was added to induce precipitation of large-sized nanoclusters. After transferring the solution to a 50 mL conical tube, the precipitant was collected by centrifugation (3500 rpm for 3 min), and more ethanol (10 mL) was added to the supernatant to induce additional precipitation of $Au_{25}(p\text{-MBA})_{18}$. This process was repeated until the supernatant was clear, and each collected products were washed with ethanol and dried in air. The fraction containing $Au_{25}(p\text{-MBA})_{18}$ cluster was further purified by PAGE separation.

KU fluorescence quenching measurement

To observe the effect of the bound gold nanoclusters on the KU dye, the fluorescence intensity of the KU dye was measured while adding gold nanoclusters to the KU solution. In detail, 1.5 mL of KU dye (0.41 μM) and 1 mL of $Au_{25}(p\text{-MBA})_{18}$ solution (18 μM) were prepared in pH 10 solution. A small volume of gold nanoclusters (<10 μL) was carefully added to the KU solution and thoroughly mixed with a glass pipette. The solution was excited at 500 nm wavelength, and the fluorescence intensity was read at 554 nm. The gold nanocluster was added until the KU intensity was quenched completely. The mole of the nanocluster was calculated based on the added volume. The mole amount of $Au_{25}(p\text{-MBA})_{18}$ was divided by the KU mole to calculate the molar ratio. The KU intensity measurement for $Au_{102}(p\text{-MBA})_{44}$ and $Au_{250}(p\text{-MBA})_n$ was performed by a similar procedure. The KU dye concentration was prepared lower than 3 μM to avoid quenching behaviour by the high concentration. Moreover, to avoid the effect of the concentration changes by the added nanocluster solution, the gold nanocluster was prepared in a very high concentration.

Preparation of the gold nanocluster and KU complex

Based on the concentration of the KU dye, the gold nanocluster was added to the solution, and the concentration of the KU dye was calculated by using the extinction coefficient value. 2 mL of 1.0 μM KU dye solution and 2 mL of 0.5 μM of $Au_{25}(p\text{-MBA})_{18}$ solution were prepared in pH 10 aqueous solution. 1 mL of each solution was mixed to form a complexation. ($[mol_{Au}]/[mol_{KU}] = 2$) KU complex with $Au_{102}(p\text{-MBA})_{44}$ and $Au_{250}(p\text{-MBA})_n$ was prepared with the same method. The concentration for the KU dye was less than 3 μM.

Acid–base titration measurement of $Au_{25}(p\text{-MBA})_{18}$ and $Au_{250}(p\text{-MBA})_n$ nanoclusters

The protonation–deprotonation behaviour of the gold nanoclusters was studied using regular acid–base pH titration. Titration curves were measured in pure H_2O with the purified and precipitated gold nanoclusters. The nanocluster was dissolved in pH 4–5 water and centrifuged to remove any precipitating nanoclusters. In addition, the pK_a was extracted from the titration data by evaluating the titration curve's first and second derivative plots.

First derivative:

$$\mathrm{dpH/d}V$$

where, dpH is the change in pH between successive additions of titrant and dV is the volume of the added titrant.

Second derivative:

$$\mathrm{d(dpH/d}V)/\mathrm{d}V$$

Molecular dynamics simulations and essential dynamics analysis

Initial coordinates of $Au_{25}(p\text{-MBA})_{18}$ nanocluster were obtained from a previous model[29] based on the reported crystal structure of $Au_{25}(PET)_{18}$ (PET = phenylethylthiolate),[30,31] while $Au_{102}(p\text{-MBA})_{44}$ was obtained from the published X-ray crystal structure.[32] Simulations were performed with GROMACS 2020 (ref. 33) using an AMBER-compatible force field for thiolate-protected nanoclusters.[34] The fully deprotonated[35] *p*-MBA-protected gold

nanoclusters were placed in a periodic cubic box with TIP3P water molecules[36] using the SETTLE algorithm to constrain their internal degrees of freedom.[37] Sodium and chloride ions (0.15 M NaCl) were added to neutralize the systems. Energy minimizations were carried out by using the steepest descent algorithm, followed by a short equilibration consisting of 10 ns NVT ensemble (constant number of particles, volume, and temperature) at 300 K and 10 ns NPT (constant number of particles, pressure, and temperature) at 300 K and 1 bar pressure with position restraints on the heavy atoms of the nanoclusters. The velocity-rescale thermostat was used to keep the temperature constant at the desired value with a coupling time constant of 0.1 ps.[38] Berendsen barostat with a reference pressure of 1 bar and coupling time constant of 1.0 ps[39] was used in the NPT equilibration. Afterward, 100 ns of production MD were performed for each system removing all the position restraints. The velocity-rescale thermostat was used to keep the temperature at 300 K, and pressure was kept constant at 1 bar using Parrinello–Rahman barostat with relaxation times of 2.0 ps.[40] A leapfrog Verlet integrator was used with a 1.0 fs time step. Lennard–Jones interactions were truncated at 1.0 nm, and the particle-mesh Ewald (PME) method with a real-space cutoff of 1.0 nm and 0.12 nm grid spacing was used to model Coulomb interactions.[41] The lengths of covalent bonds containing hydrogens were constrained with the LINCS algorithm[42] for improved performance. All trajectories were visualized in VMD[43] and analysed by using the utility toolkits of GROMACS such as gmx rdf to obtain the pair correlation functions between the carbon atoms of the carboxylate groups of the ligands. The pair correlation function was calculated over the whole MD-trajectory. Pair correlation function was also solved for the phenyl rings of the ligands as a running average over 40 snapshots for the apex- and core-ligands and is reported here per phenyl ring per frame. Distances were determined from the centre of the apex/core phenyl ring to all other phenyl rings in the system. There are six apex-ligands in Au_{25} and two in Au_{102} being located at the centre of the longer SR–Au–SR–Au–SR (SR = *p*-MBA) protecting units.

ED analysis was carried out to extract the dominant modes in the overall molecular motion of the gold nanoclusters.[44,45] Covariance matrices were constructed using all the atoms of the nanoclusters and removing the rotation and translational movements. The calculated eigenvectors and eigenvalues of the covariance matrices were then projected along with the first two (most important) principal components. The trajectories were analysed by using the GROMACS utilities gmx covar and gmx anaeig. The data from ED analysis was plotted in two ways: first, as a time evolution scatter plot and second, as a configurational free energy plot. The first was plotted directly using the projection data of individual MD-snapshot structures by using colour scale dependent on the snapshot frame index 0–500. The second plot was formed by collecting the principal component analysis (PCA) projection data of all 500 MD-snapshots into equally distributed bins on the two principal axes based on the closest distance producing a 200 × 200 grid. The number of hits on bins directly gives the statistical probability distribution when correlated to the total number of snapshots in analysis. Finally, configurational free energy of the bins was solved from the probabilities using Boltzmann distribution. The minimum of the free energy was set to zero. Only the energy range between 0 kJ mol^{-1} and 5 kJ mol^{-1} was shown in the coloured contour plots. Gaussian distribution was applied to smoothen the data on the discrete grid with broadening parameter of 0.05 nm. For both studied clusters, Au_{25}(*p*-MBA)$_{18}$ and Au_{102}(*p*-MBA)$_{44}$, the last structure of the MD-simulations was used in structure visualizations. VMD symmetry tools were used to analyse the symmetries of the metal core of Au_{25}(*p*-MBA)$_{18}$ structures.

Results and discussion

Synthesis of highly pure gold nanoclusters

The three *p*-MBA protected gold nanoclusters with the composition of Au_{25}(*p*-MBA)$_{18}$, Au_{102}(*p*-MBA)$_{44}$, and Au_{250}(*p*-MBA)$_n$ were synthesized according to the reported methods.[27–29] The composition of the largest gold nanoclusters was predicted to be $Au_{210-230}$(*p*-MBA)$_{70-80}$ by experimental analysis and computationally aided prediction, based on the structurally known reference gold nanoclusters.[27] This large-size gold nanoclusters will be abbreviated as Au_{250} further on, as was defined by Sokołowska *et al.*[27] In addition, Au_{25}(*p*-MBA)$_{18}$ and Au_{102}(*p*-MBA)$_{44}$ will be abbreviated as Au_{25} and Au_{102}, respectively.

It is imperative to obtain highly pure gold nanoclusters to prevent any interference between the residues and the functionality of the pH sensor. The synthesis we followed is known to form only one size of the targeted nanoclusters. However, the bulky separated fractions could still carry excess counterions or a small portion of different size nanoclusters. In order to acquire highly purified gold nanoclusters, the fraction of each sample was separated once more through PAGE, and the targeted clusters were collected from the gel. After the distinct separation of the bands, they were cut out and extracted in water overnight. The extracted samples were purified by precipitating the nanoclusters using 100 μL 0.1 M NaCl and 0.1 M HCl (pH 2). The precipitant was thoroughly washed with clean water to remove excess salt or residue from the gel and air-dried for a day. The products were stored in the refrigerator and were re-dissolved with 0.01 M NaOH before use. The electrophoresis was run once more to evaluate the purity and stability of the separated nanoclusters. As shown in Fig. 1a, a single narrow band was observed for each nanocluster, indicating the high stability and purity of the prepared nanoclusters. The distinct difference in each band position shows that the size of the nanoclusters is relatively different, which is apposite to our comparison. The TEM results were also used to verify the purity of Au_{25}, Au_{102}, and Au_{250} nanoclusters (Fig. S1; see Experimental section† for more details). Each nanocluster showed a monodisperse nature with a spherical shape. The size of Au_{25}, Au_{102}, and Au_{250} was 1.1 nm, 1.3 nm, and 1.56 nm, respectively, and the values correspond to the sizes reported elsewhere.[27,29,46,47]

Optical measurements of the gold nanoclusters

UV-vis absorption spectra and the extinction coefficient values of the isolated gold nanoclusters in water are presented in Fig. 1b and c. The merit of using gold nanoclusters is that the

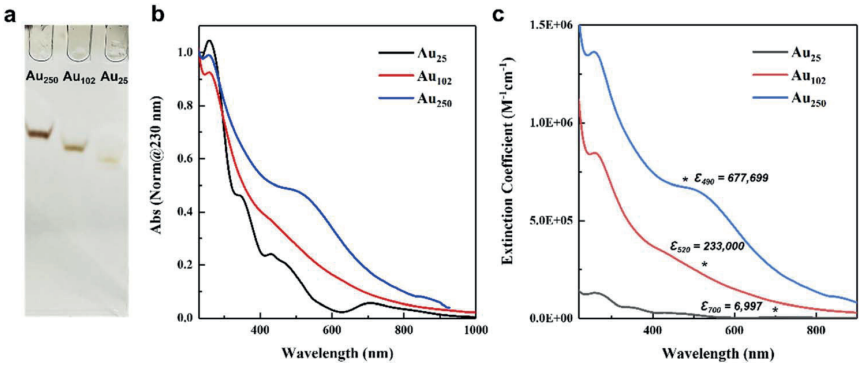

Fig. 1 Characterization of synthesized *p*-MBA protected gold nanocluster. (a) Image of PAGE separation of the purified Au_{250} (left), Au_{102} (middle), and Au_{25} (right). (b) Normalized UV-vis absorption spectra and (c) extinction coefficient spectra in water.

electronic structure of the nanoclusters changes by the size and shape of their metallic core, which is reflected in their UV-vis spectra. For smaller sizes, the spectrum is continuous with distinctive peaks, while for larger sizes, a clear localized surface plasmon resonance (LSPR) is observed.[48,49] These unique, distinctive absorbance features provide a convenient tool for identifying the isolated nanoclusters. As shown in Fig. 1b, the gold nanoclusters exhibit size-dependent absorption spectra with the same absorption peak around 200–300 nm, consistent with the hybridized transitions localized on the *p*-MBA ligand.[50] Au_{25} nanocluster displays characteristic absorption peaks at 701, 470, and 430 nm, corresponding to the Au_{25} characteristic optical transitions.[29] Larger nanoclusters show more featureless optical spectra than Au_{25}. Therefore, the optical spectra of the larger nanoclusters were compared with the reported spectra for evaluation. Au_{102} has a weak peak around 423 nm,[23] and Au_{250} exhibits weak LSPR around 530 nm.[27] These isolated large-size nanoclusters were identified as Au_{102} and Au_{250}, respectively.

We measured the extinction coefficients of the gold nanoclusters to determine the molar concentration of the dilute gold nanocluster solution for further observations. The extinction coefficient was calculated using the Beer–Lambert equation (see ESI† for details). As shown in Fig. 1c, the differences in the extinction coefficient vales for each nanocluster followed qualitatively the number of gold atoms. To avoid any interference by absorbance of the residues, such as salt and *p*-MBA (absorbance at ~200–300 nm), the extinction coefficient values of Au_{25}, Au_{102} and Au_{250} were read at 700, 520, and 490 nm, respectively. The molar extinction coefficient values of Au_{25} (6997 M^{-1} cm^{-1}), Au_{102} (233 000 M^{-1} cm^{-1}), and Au_{250} (677 699 M^{-1} cm^{-1}) (Fig. 1c) were further utilized to calculate the molar ratio between the gold nanoclusters and the KU dye.

pH response measurements of the Au + KU complex

The steady-state fluorescent intensity of the KU dye at different pH was measured in the presence of three different-sized gold nanoclusters protected with the same type of ligand, to understand the size effect on the functionality of the fluorescent pH sensor. The fluorescence of the positively charged (+1) KU dye is quenched when they are bound to the negatively charged ($-COO^-$) *p*-MBA protected gold nanoclusters, leading to an energy transfer process from the KU dye to the gold nanocluster[23] (Fig. 2a). This behaviour allows the fluorescence of the KU dye to quench and it is dependent on the surface charge of the nanocluster, which could be regulated by the amount of the nanoclusters or the number of charged ligands. It is worth noting that, based on the 8 electron superatom model, Au_{25} is known to have a −1 charge state, but it is mainly localized in the metal core, not affecting its surface charge. Thus, in our studies, this extra charge was not considered a factor affecting the interaction between the KU dye and the *p*-MBA ligands. Moreover, the only possible counterion to stabilize the cluster charge is Na^+, which, due to its small steric size, cannot considerably affect the accessibility of the dye to the cluster surface. As shown in Fig. 2b, Au_{25}, Au_{102}, and Au_{250} were added to the KU solution (pH 10) having the same concentration in each case, which triggered the KU intensity to drop rapidly (see Experimental section for more details). Moreover, the trend of the quenching curves differed by the nanoclusters. In detail, Au_{250} shows the fastest quenching characteristic, followed by Au_{102} and Au_{25}. Due to the abundance of the KU molecule in the solution and the availability of multiple ligands on each cluster, the complexation involves several KU dyes interacting with one gold nanocluster. To determine how many KU dyes tend to bound to the nanoclusters in a low concentration region ($[mol_{Au}]/[mol_{KU}] < 0.1$), the initial slope of the titration curve was determined. As shown in Fig. S2,† approximately 2, 5, and 19 KU dyes were bound to Au_{25}, Au_{102}, and Au_{250}, respectively. This result indicates that more than one KU dye molecules are bound to larger nanoclusters because of the highly negative surface charge and more *p*-MBA groups available for binding per clusters. Furthermore, the fluorescence for all three nanoclusters is almost totally quenched when the $[mol_{Au}]/[mol_{KU}]$ ratio reaches 2, indicating nearly all the KU dyes formed a complex with the nanoclusters.

The pH dependence measurements of the Au + KU complexes were carried out to observe the effect of the different gold nanoclusters on the response. In order to accurately compare how the KU fluorescence properties change according to the size of the gold nanocluster, it is essential to fix the other

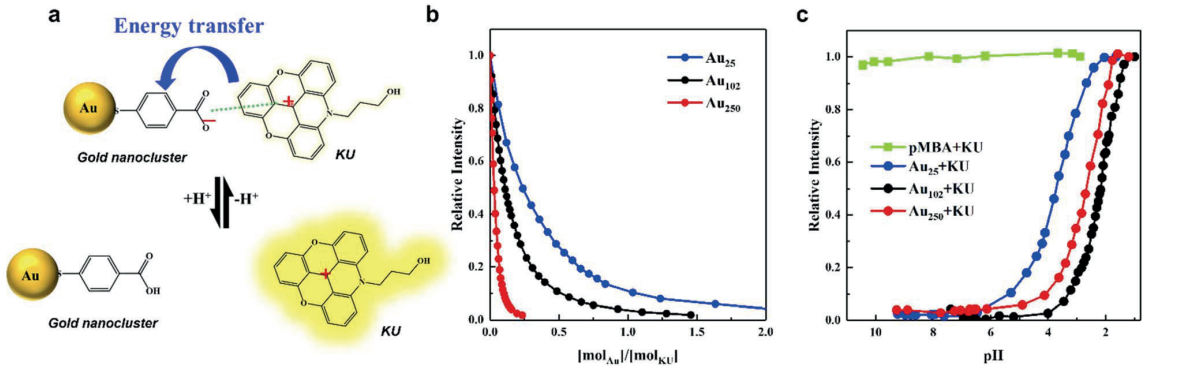

Fig. 2 (a) Schematic diagram illustrating electrostatic interaction and energy transfer process between the *p*-MBA protected gold nanoclusters (AuNC) and KU dye in different pH conditions. (b) Relative intensity of KU emission as function of $[mol_{Au}]/[mol_{KU}]$ molar ratio in pH 10 solution (excitation wavelength 500 nm). (c) Relative intensity of KU emission as function of pH. The molar ratio of the solution was $[mol_{Au}]/[mol_{KU}] = 2$.

conditions carefully. Therefore, in the subsequent pH experiment, the concentrations for the gold nanocluster and KU were fixed to $[mol_{Au}]/[mol_{KU}] = 2$, where the KU fluorescence quenches with all nanoclusters (see Experimental section for more details). The pH titration curve of the Au + KU complex was measured by gradually adding 0.01 M HCl to the Au + KU complex solution. As the HCl is added, the fluorescence of the KU dye dramatically starts to increase around pH 4–6 and saturates around pH 1 (Fig. 2c). On the other hand, the fluorescence of *p*-MBA + KU complex did not change during pH adjustments, which indicates that the pH dependence properties of the KU are exhibited only in the presence of the gold nanoclusters. Moreover, a distinct shift of the titration curve for each complex was observed. These significant changes in the titration curves lead us to determine the approximate half-point pH of each curve for further comparison. The pH values were read at the 0.5 relative intensity point. The half-point pH was 2.11, 2.66, and 3.70 for Au_{250}, Au_{102}, and Au_{25}, respectively. This result clearly shows that the pH response of the KU dye can be regulated by varying the size of the nanocluster as predicted. Moreover, this is the first experimental result on tuning the pH sensor properties by tailoring the size of the nanoclusters.

In detail, the pH titration curve for the Au_{250} + KU complex was shifted to a higher pH region than the Au_{102} + KU complex, indicating the correlation between the surface curvature and the pK_a value of the nanoclusters, assuming that the pH dependence of fluorescence is related to the surface charge of the cluster. On the other hand, the Au_{25} + KU complex exhibited an unexpectedly high pK_a trend compared to the other larger nanocluster-based complexes. Based on previous research,[24] Au_{25} was expected to have the lowest pH response range owing to its highest surface curvature among the nanoclusters. However, as shown in Fig. 2c, the Au_{25} + KU complex shows the highest pH response range, followed by Au_{250} and Au_{102}. To understand the grounds for the unexpected behaviour of the Au_{25} nanocluster, it is crucial to comprehend the fundamental nature of the nanoclusters. As shown in Fig. 2a, the KU dye's fluorescence intensity depends on the surface negativity of the gold nanoclusters. In other words, the pK_a of the nanoclusters will be one of the factors in regulating the effective pH range. Therefore, it was important to measure the protonation–deprotonation behaviour of the Au_{25}, Au_{102}, and Au_{250} nanoclusters by the acid–base pH titration method.

Acid–base titration of the gold nanoclusters

The titration curves were measured in pure H_2O, where the clusters were diluted and dispersed in the lowest pH solution that did not fully precipitate the nanoclusters (pH ~ 4–5, see Experimental section for more details). The titration studies for Au_{102} were referred to in our previous report.[35] As shown in Fig. 3, a single pK_a is observed in both Au_{25} and Au_{250}, and the pK_a values were extracted from the second derivative curve, as shown in Fig. S3 and Table S1.† The pK_a values for Au_{25} and Au_{250} nanoclusters were 6.82 and 6.29, respectively. The pK_a values for the nanoclusters had similar order compared to the Au + KU complex half-point pH. The difference in the apparent pK_a of the nanoclusters and the response pH of the Au + KU complex could be explained by the effect of the positively charged KU dye. In the presence of a positively charged counterion, the interaction between the neighbouring weak acid groups is reduced, thus decreasing the pK_a value as in our experimental results.[51–53] Moreover, the intermolecular interactions, *i.e.*, π–π stacking of the ligands, could affect the complexation between the gold nanocluster and the KU dye; thus, the pH response range and the acid–base titration will not follow each other in a one-to-one correlation. Even though we still have to understand the unexpected result from Au_{25}, the results indicate that the pK_a value of the nanocluster is controlled by the size, and by these pK_a values, the KU response range is regulated. Moreover, the consistency of the trends between the nanoclusters makes it possible to exhibit the probability of strategizing how to design and regulate the pH sensor with precision.

Surface structure analysis of Au_{25}(*p*-MBA)$_{18}$

The pK_a of the nanoclusters is regulated by their curvature, which will, in turn, determine the distance at which the

ligand–ligand interaction occurs. The closer the negatively charged ligands are, the higher the equilibrium shifts to a higher pH, enhancing the pK_a. Therefore, analysing and comparing the intermolecular packing of the nanocluster ligand layer is needed to understand the unique pK_a shift behaviour of Au_{25}. Fig. 4 shows the calculated pair correlation functions $g(r)$ between carbon atoms of *p*-MBA carboxylate groups ($-COO^-$) from MD simulations of Au_{25} and Au_{102} nanoclusters in water. For Au_{25}, a very sharp main peak is observed at 0.4 nm with broader but still well-defined minor peaks at longer distances. While, for Au_{102}, the first peak is observed at 0.5 nm with a remarkable difference in intensity compared to Au_{25} and minor oscillations above this distance. The $g(r)$ peaks for Au_{25} suggest a highly structured ligand layer, which is governed by the packing of phenyl rings of the *p*-MBA ligands and the multiple π–π stacking interactions. Computed $g(r)$ for phenyl–phenyl rings during 100 ns MD simulation (Fig. S4†) show how the highly ordered ligand layer of Au_{25} is established as the simulation time increases. This feature is exhibited in a sharp increase in the peaks related to the average nearest and second nearest neighbour distances between the π–π stacked groups. In contrary, Au_{102} shows considerably less structural ordering in the ligand layer and the characteristics are different compared to Au_{25} (see Fig. S5†). For Au_{102} a higher peak appears during the simulation at 0.5 nm distance which is typical for neighbouring T-stacked phenyl rings. It is known that parallel stacked phenyl rings have a higher pK_a compared to the T-stacked phenyl rings because of their higher repulsive behaviour. Therefore, Au_{25} is eligible to have a higher pK_a than Au_{102}.[54]

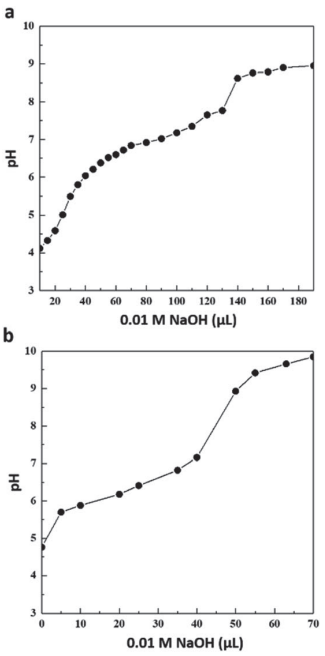

Fig. 3 Acid–base titration curve of (a) Au_{25} and (b) Au_{250} nanoclusters in water.

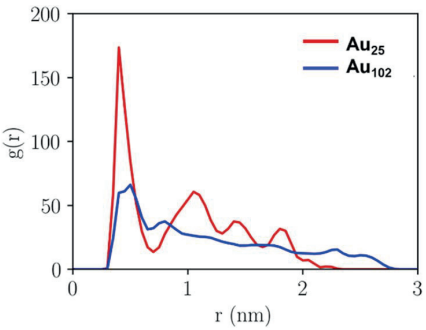

Fig. 4 Pair correlation function $g(r)$ of carbon atoms of the carboxylic groups of ligands of Au_{25} and Au_{102} clusters as calculated from MD-trajectory.

The flexibility and structural stability of the Au_{25} and Au_{102} ligand layer was also studied by ED analysis (Fig. 5a and b). ED analysis can be used to solve the principal collective modes of the atomic fluctuations and statistically analyse the most prominent conformations as projected to them. Here, the first two principal components were selected to analyse the projection of MD-trajectories in the conformational phase space. Au_{25} covered a smaller region of phase space with only one major basin (Fig. 5a and c), while Au_{102} showed several conformational basins distributed on a larger region (Fig. 5b and d), which demonstrates a higher ordered arrangement of *p*-MBA ligands on Au_{25} over Au_{102} nanoclusters. Time evolution in Fig. 5 shows that the structure of Au_{25} gets stabilized in 60 ns (after 300 snapshot frames) after which the conformation is frozen at the major basin of the phase space. The same kind of stabilization is not seen for Au_{102}. In terms of structural features, Au_{25} and Au_{102} exhibit a different gold–sulfur interface. Au_{25} has an icosahedral Au_{13} core protected by six long SR–Au–SR–Au–SR units, while Au_{102} has 19 short SR–Au–SR units and only two long SR–Au–SR–Au–SR units protecting the Au_{79} core.[31,32,55,56] Based on this composition, the Au_{25} ligand layer is expected to be more flexible due to the long units attached to an ultrasmall core with a high curvature. Hence, the flexibility allows Au_{25} cluster to adjust itself better for changed conditions than Au_{102} and find a highly ordered and stable ligand layer arrangement, although the relative distribution of the ligands in Au_{25} and Au_{102} was initially qualitatively the same (see Fig. S4 and S5†). Fig. 5e and f illustrates the multiple π–π stacking interactions formed between the locally densely packed phenyl rings of *p*-MBA ligands as observed in the final snapshot of 100 ns MD simulation of Au_{25} nanocluster in comparison to the final snapshot of Au_{102}. The point group symmetry of the metal core of the averaged structure of last 200 snapshots of Au_{25} MD-trajectory is D_{2d} with root mean square deviation (RMSD) of 0.054 Å from the ideal which resembles the structure distortions that are seen for the neutral and cationic experimental clusters as compared to the nearly ideal icosahedral metal core of experimental anionic cluster.[57] Our results indicate that Au_{25} has a more organized ligand layer orientation than Au_{102}, which can explain the singular pK_a shift observed.

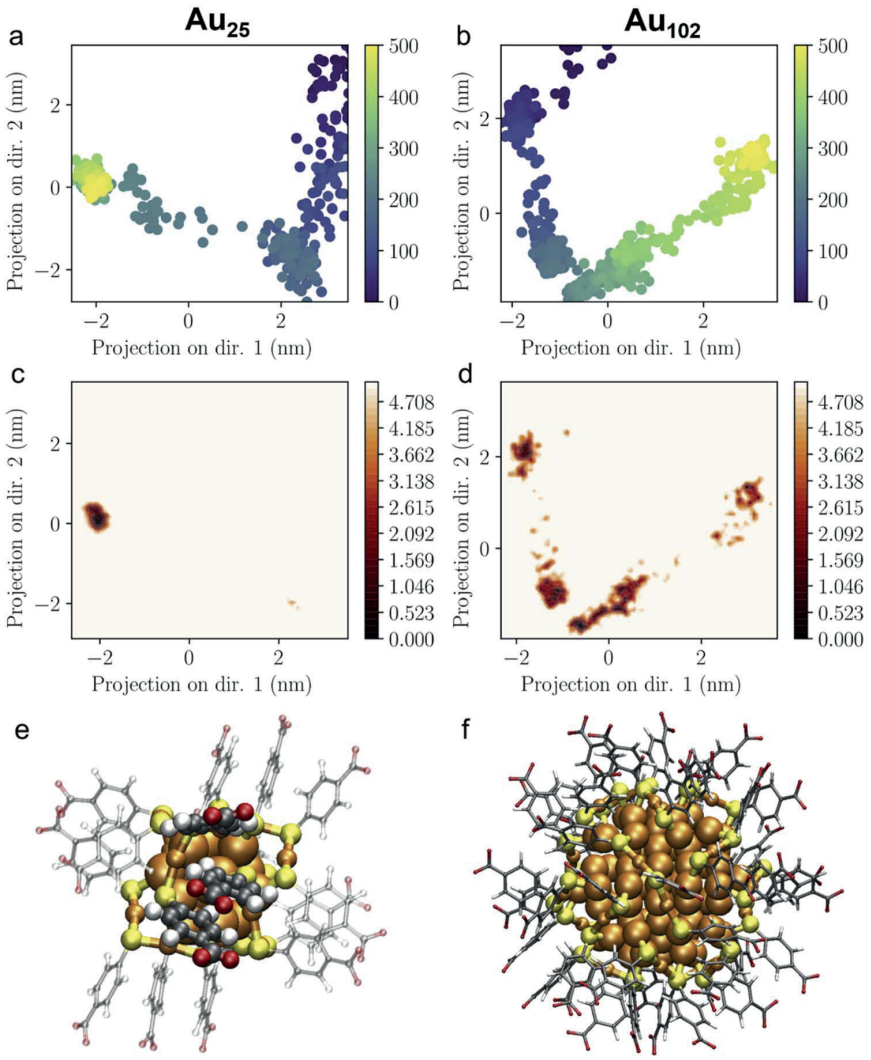

Fig. 5 a) and (b) Show the time evolution of the conformations, and (c) and (d) show the conformational free energies of the MD-trajectories of Au_{25} and Au_{102} in the essential dynamics analysis. Minimum of the free energy is set to zero and the colour scale is fixed to the energy scale from 0 kJ mol^{-1} to 5 kJ mol^{-1}. The data above 5 kJ mol^{-1} is not distinguished and is shown in the unified solid pale background. Projection is done based on the two main principal component eigenvector directions. (e) and (f) Show the final structure of Au_{25} and Au_{102} cluster taken from the same 100 ns MD simulation. Formation of six separate $\pi-\pi$ stacked groups of three ligands is highlighted for Au_{25}.

Conclusions

We have shown a robust strategy for regulating the pH response range by tailoring the size of the gold nanoclusters. For different-sized gold nanoclusters, Au_{25}, Au_{102}, and Au_{250} were synthesized and formed a complex with the KU dye for pH measurements. The pH titration measurement of the Au_n + KU complex (n = 25, 102, 250) showed that the pH response range of the KU dye was evidently shifted, which matched well with the order of the pK_a value measured by the acid–base titration measurement. Au_{250} exhibited a higher pH response range than Au_{102} based on the surface curvature effect. However, Au_{25} showed an unexpectedly high pK_a value compared to the larger size nanoclusters. This behaviour was understood by performing the MD simulations and ED analysis. The results showed that small nanoclusters do not follow the scaling between the curvature and the pK_a. Instead, the behaviour is more controlled by the distribution and interaction of the *p*-MBA ligands on the nanocluster surface. This is the first study attempting to analyse the pK_a value of ultrasmall nanoclusters and understand the factor that regulates the protonation behaviour in an atomic range. Understanding the relationship between the ligands orientation and the pK_a trend of each nanocluster on an atomic scale makes it possible to create a toolbox for efficiently designing or modifying the pH sensor by tailoring the size of the nanoclusters. Furthermore, the use of atomically precise

nanoclusters facilitates synergy between theory and experiments toward paving the way for the rational design of new probes.

Author contributions

Kyunglim Pyo: conceptualization, investigation, validation, visualization, writing – original draft. María Francisca Matus: formal analysis, visualization, writing – review & editing. Sami Malola: formal analysis, visualization, writing – review & editing. Eero Hulkko: resources, supervision. Johanna Alaranta: resources. Tanja Lahtinen: Resources, supervision. Hannu Häkkinen: conceptualization, funding acquisition, supervision, writing – review & editing. Mika Pettersson: conceptualization, funding acquisition, supervision, writing – review & editing. All authors discussed the results.

Conflicts of interest

There are no conflicts to declare.

Acknowledgements

This work was supported by the Academy of Finland (grants 292352, 319208), the post-doctoral program of the NSC, and by the Basic Science Research Program through the National Research Foundation of Korea (NRF) funded by the Ministry of Education (2021R1A6A3A03038668). The computations were made at the Finnish National Supercomputing Centre CSC. We thank Marta Monti for discussions on the analysis of the dynamics of the nanoclusters' ligand layer.

Notes and references

1 B. A. Webb, *et al.*, Dysregulated pH: a perfect storm for cancer progression, *Nat. Rev. Cancer*, 2011, **11**, 671–677.
2 M. Stubbs, *et al.*, Metabolic consequences of a reversed pH gradient in rat tumors, *Cancer Res.*, 1994, **54**, 4011–4016.
3 M. I. Khan, *et al.*, A review on pH sensitive materials for sensors and detection methods, *Microsyst. Technol.*, 2017, **23**, 4391–4404.
4 R. Avolio, *et al.*, Review of pH sensing materials from macro- to nano-scale: recent developments and examples of seawater applications, *Crit. Rev. Environ. Sci. Technol.*, 2022, **52**, 979–1021.
5 J. R. Casey, S. Grinstein and J. Orlowski, Sensors and regulators of intracellular pH, *Nat. Rev. Mol. Cell Biol.*, 2010, **11**, 50–61.
6 W. F. Boron, Regulation of Intracellular pH, *Adv. Physiol. Educ.*, 2004, **28**, 160–179.
7 Y. Liu, K. A. White and D. L. Barber, Intracellular pH regulates cancer and stem cell behaviors: a protein dynamics perspective, *Front. Oncol.*, 2020, **10**, e1401.
8 D. Lagadic-Gossmann, L. Huc and V. Lecureur, Alterations of intracellular pH homeostasis in apoptosis: origins and roles, *Cell Death Differ.*, 2004, **11**, 953–961.
9 R. A. Gottlieb, *et al.*, Apoptosis induced in jurkat cells by several agents is preceded by intracellular acidification, *Proc. Natl. Acad. Sci. U. S. A.*, 1996, **93**, 654–658.
10 A. Ishaque and M. Al-Rubeai, Use of intracellular pH and annexin-V flow cytometric assays to monitor apoptosis and its suppression by bcl-2 over-expression in hybridoma cell culture, *J. Immunol. Methods*, 1998, **221**, 43–57.
11 H. Izumi, *et al.*, Cellular pH regulators: potentially promising molecular targets for cancer chemotherapy, *Cancer Treat. Rev.*, 2003, **29**, 541–549.
12 T. A. Davies, *et al.*, Non-age related differences in thrombin responses by platelets from male patients with advanced Alzheimer's disease, *Biochem. Biophys. Res. Commun.*, 1993, **194**, 537–543.
13 J. Han and K. Burgess, Fluorescent indicators for intracellular pH, *Chem. Rev.*, 2010, **110**, 2709–2728.
14 J. Dakin and B. Culshaw, *Optical Fiber Sensors*, Artech House, Boston-London, 1997, vol. 15, ch. 8, pp. 53–107.
15 S. Schutting, *et al.*, New highly fluorescent pH indicator for ratiometric RGB imaging of pCO_2, *Methods Appl. Fluoresc.*, 2014, **2**, e024001.
16 N. Boens, V. Leen and W. Dehaen, Fluorescent indicators based on BODIPY, *Chem. Soc. Rev.*, 2012, **41**, 1130–1172.
17 A. P. Demchenko, Photobleaching of organic fluorophores: quantitative characterization, mechanisms, protection, *Methods Appl. Fluoresc.*, 2020, **8**, 022001.
18 P. Reineck, *et al.*, Brightness and photostability of emerging red and near-IR fluorescent nanomaterials for bioimaging, *Adv. Opt. Mater.*, 2016, **4**, 1549–1557.
19 A. Praetorius, *et al.*, Design of a fluorescent dye for indicator displacement from cucurbiturils: a macrocycle-responsive fluorescent switch operating through a pKa shift, *Org. Lett.*, 2008, **10**, 4089–4092.
20 K. N. More, *et al.*, Molecular design of fluorescent pH sensors based on reduced rhodol by structure-pKa relationship for imaging of lysosome, *Dyes Pigm.*, 2021, **184**, 108785.
21 D. R. Wilson, *et al.*, A triple-fluorophore-labeled nucleic acid pH nanosensor to investigate non-viral gene delivery, *Mol. Ther.*, 2017, **25**, 1697–1709.
22 R. V. Benjaminsen, *et al.*, Evaluating nanoparticle sensor design for intracellular pH measurements, *ACS Nano*, 2011, **5**, 5864–5873.
23 E. Hulkko, *et al.*, Covalent and non-covalent coupling of a Au102 nanocluster with a fluorophore: energy transfer, quenching and intracellular pH sensing, *Nanoscale Adv.*, 2021, **3**, 6649–6658.
24 D. Wang, *et al.*, How and why nanoparticle's curvature regulates the apparent pKa of the coating ligands, *J. Am. Chem. Soc.*, 2011, **133**, 2192–2197.
25 D. A. Walker, *et al.*, Geometric curvature controls the chemical patchiness and self-assembly of nanoparticles, *Nat. Nanotechnol.*, 2013, **8**, 676–681.
26 J. Lin, *et al.*, Understanding the synergistic effect of physicochemical properties of nanoparticles and their cellular entry pathways, *Commun. Biol.*, 2020, **3**, 205.

27 K. Sokołowska, *et al.*, Towards controlled synthesis of water-soluble gold nanoclusters: synthesis and analysis, *J. Phys. Chem. C*, 2019, **123**, 2602–2612.
28 K. Salorinne, *et al.*, Solvation chemistry of water-soluble thiol-protected gold nanocluster Au_{102} from DOSY NMR spectroscopy and DFT calculations, *Nanoscale*, 2014, **6**, 7823–7826.
29 Y. Cao, *et al.*, Reversible isomerization of metal nanoclusters induced by intermolecular interaction, *Chem*, 2021, **7**, 2227–2244.
30 M. W. Heaven, *et al.*, Crystal Structure of the Gold Nanoparticle $[N(C_8H_{17})_4][Au_{25}(SCH_2CH_2Ph)_{18}]$, *J. Am. Chem. Soc.*, 2008, **130**, 3754–3755.
31 M. Zhu, *et al.*, Correlating the crystal structure of a thiol-protected Au_{25} cluster and optical properties, *J. Am. Chem. Soc.*, 2008, **130**, 5883–5885.
32 P. D. Jadzinsky, *et al.*, Structure of a thiol monolayer-protected gold nanoparticle at 1.1 Å resolution, *Science*, 2007, **318**, 430–433.
33 D. Van Der Spoel, *et al.*, GROMACS: Fast, flexible, and free, *J. Comput. Chem.*, 2005, **26**, 1701–1718.
34 E. Pohjolainen, *et al.*, A unified AMBER-compatible molecular mechanics force field for thiolate-protected gold nanoclusters, *J. Chem. Theory Comput.*, 2016, **12**, 1342–1350.
35 J. Koivisto, *et al.*, Acid−base properties and surface charge distribution of the water-soluble $Au_{102}(pMBA)_{44}$ nanocluster, *J. Phys. Chem. C*, 2016, **120**, 10041–10050.
36 W. L. Jorgensen, *et al.*, Comparison of simple potential functions for simulating liquid water, *J. Chem. Phys.*, 1983, **79**, 926–935.
37 S. Miyamoto and P. A. Kollman, Settle: an analytical version of the SHAKE and RATTLE algorithm for rigid water models, *J. Comput. Chem.*, 1992, **13**, 952–962.
38 G. Bussi and M. Parrinello, Stochastic thermostats: comparison of local and global schemes, *Comput. Phys. Commun.*, 2008, **179**, 26–29.
39 H. J. C. Berendsen, *et al.*, Molecular dynamics with coupling to an external bath, *J. Chem. Phys.*, 1984, **81**, 3684–3690.
40 M. Parrinello and A. Rahman, Polymorphic transitions in single crystals: a new molecular dynamics method, *J. Appl. Phys.*, 1981, **52**, 7182–7190.
41 T. Darden, D. York and L. Pedersen, Particle mesh Ewald: an N log(N) method for Ewald sums in large systems, *J. Chem. Phys.*, 1993, **98**, 10089–10092.
42 B. Hess, *et al.*, LINCS: a linear constraint solver for molecular simulations, *J. Comput. Chem.*, 1997, **18**, 1463–1472.
43 W. Humphrey, A. Dalke and K. Schulten, VMD: visual molecular dynamics, *J. Mol. Graph. Model.*, 1996, **14**, 33–38.
44 A. Amadei, A. B. M. Linssen and H. J. C. Berendsen, Essential dynamics of proteins, *Proteins: Struct., Funct., Bioinf.*, 1993, **17**, 412–425.
45 M. Monti, M. Stener and M. Aschi, A computational approach for modelling Electronic Circular Dichroism of solvated chromophores, *J. Comput. Chem.*, 2022, DOI: **10.1002/jcc.27001**.
46 T. Lahtinen, *et al.*, Covalently linked multimers of gold nanoclusters $Au_{102}(p\text{-}MBA)_{44}$ and $Au_{\sim 250}(p\text{-}MBA)_n$, *Nanoscale*, 2016, **8**, 18665–18674.
47 Z. Wu, J. Suhan and R. Jin, One-pot synthesis of atomically monodisperse, thiol-functionalized Au_{25} nanoclusters, *J. Mater. Chem.*, 2009, **19**, 622–626.
48 Y. Negishi, *et al.*, A critical size for emergence of nonbulk electronic and geometric structures in dodecanethiolate-protected Au clusters, *J. Am. Chem. Soc.*, 2015, **137**, 1206–1212.
49 C. Yi, *et al.*, Nanometals: identifying the onset of metallic relaxation dynamics in monolayer-protected gold clusters using femtosecond spectroscopy, *J. Phys. Chem. C*, 2015, **119**, 6307–6313.
50 M. Walter, *et al.*, A unified view of ligand-protected gold clusters as superatom complexes, *Proc. Natl. Acad. Sci. U. S. A.*, 2008, **105**, 9157–9162.
51 C. N. Pace, G. R. Grimsley and J. M. Scholtz, Protein ionizable groups: pK values and their contribution to protein stability and solubility, *J. Biol. Chem.*, 2009, **284**, 13285–13289.
52 S. Mafé, V. Garcia-Morale and P. Ramirez, Estimation of pKa shifts in weak polyacids using a simple molecular model: effects of strong polybases, hydrogen bonding and divalent counterion binding, *Chem. Phys.*, 2004, **296**, 29–35.
53 P. Ramirez, *et al.*, Donnan equilibrium of ionic drugs in pH-dependent fixed charge membranes: theoretical modeling, *J. Colloid Interface Sci.*, 2002, **253**, 171–179.
54 A. Olasz, *et al.*, Effect of the π-π stacking interaction on the acidity of phenol, *Chem. Phys. Lett.*, 2005, **407**, 504–509.
55 H. Häkkinen, The gold–sulfur interface at the nanoscale, *Nat. Chem.*, 2012, **4**, 443–455.
56 M. Zhu, W. T. Eckenhoff, T. Pintauer and R. Jin, Conversion of anionic $[Au_{25}(SCH_2CH_2Ph)_{18}]^-$ cluster to charge neutral cluster *via* air oxidation, *J. Phys. Chem. C*, 2008, **112**, 14221–14224.
57 M. A. Tofanelli, *et al.*, Jahn–Teller effects in $Au_{25}(SR)_{18}$, *Chem. Sci.*, 2016, **7**, 1882–1890.

IV

MODIFYING THE TERMINAL PHENYL GROUP OF MONOMETHINE CYANINE DYES AS A PATHWAY TO BRIGHTER NUCLEIC ACID PROBES

by

Alaranta, J., Valkonen, A., Rissanen, K. & Lahtinen, T. 2024

New Journal of Chemistry, 48, 4931-4935.

https://doi.org/10.1039/d3nj05400d

NJC

PAPER

View Article Online
View Journal | View Issue

Cite this: *New J. Chem.*, 2024, **48**, 4931

Modifying the terminal phenyl group of monomethine cyanine dyes as a pathway to brighter nucleic acid probes†

Johanna M. Alaranta, [a] Arto M. Valkonen, [a] Sailee S. Shroff, [b] Varpu S. Marjomäki, [b] Kari Rissanen [a] and Tanja M. Lahtinen *[a]

Received 23rd November 2023,
Accepted 19th February 2024

DOI: 10.1039/d3nj05400d

rsc.li/njc

Three novel monomethine cyanine dyes were synthesized carrying electron donating groups to obtain even brighter nucleic acids probes. Photophysical properties of these dyes were evaluated with DNA and selected dyes with RNA. A great variation in brightness and binding properties of the dyes was observed. Moreover the X-ray crystal structures are presented for two dyes.

Fluorescent probes are an essential part of the molecular biologist's instrumentation to image nucleic acids in a wide range of applications. These include for example PCR,[1–5] melting curve analysis,[6,7] quantification of nucleic acids from environmental samples[8] and gel electrophoresis.[9] A widely utilized probe for these applications is, for example, **SYBR Green I**, which has been very popular since it was introduced.[10] Monomethine cyanine dyes exhibit all the expected qualities for excellent fluorescent probes for nucleic acids: turn-on fluorescence with low background emission, desirable photostability and they are less toxic to cells when compared to another popular DNA stain, ethidium bromide.[11] However, during recent years the demand for selective dyes for different types of nucleic acids has increased. The increasing interest to study RNA, for example to the develop antivirals[12] and RNA vaccines,[13] has only amplified the appeal to research RNA specific fluorescent probes. Also designing even more sensitive dyes to accommodate the new challenging applications, such as studying the opening mechanism of viruses is equally important.[14] By understanding the structural elements underlying the biological activity of these dyes, is one possible way to achieve these goals.

In recent years we have systematically studied the structure of SYBR green related cyanine dyes, trying to find the key points that change the photophysical qualities of these dyes. 14 newly synthesized monomethine cyanine dyes and their structural differences and their effect to the photophysical qualities have been studied by us.[14–16] The goal is to identify the important elements, so that the best structural features can be combined to produce the ultimate fluorescent probe for nucleic acid staining. In our previous studies, the binding properties were investigated for all 14 dyes with DNA and for selected dyes, also with RNA, to understand the phenomena behind the great turn-on fluorescence. The molecular modelling indicated that the dyes synthesised by us bind in the minor groove of the DNA double helix, while it had been widely accepted that SYBR Green related dyes are mainly intercalators.[17,18] It was also shown that one way to improve the brightness of the dyes could be by enhancing the rigidity of the molecule when binding the dsDNA. We also noted that the heteroatoms in different positions of the dye core had great effect to the photophysical qualities and just by changing one heteroatom, for example oxygen to sulphur, clear difference in these qualities could be observed. The effect of heteroatoms on the photophysical qualities have intrigued many scientists working in the wide field of fluorescent probes, such as rhodamines,[21] which has been extensively studied as well as difluoroborates.[22] Moreover, all our dyes have had highest molar absorption coefficients in ethanol or DCM where the dyes are fully soluble.[14,15] Kurutos *et al.*[23] have previously showed that one way to improve monomethine cyanine dyes qualities and make them more user friendly is to improve the water solubility by adding substituents to alkyl chains with additional charges to the main core of the dyes.

With all these results in mind, we designed modifications for the terminal phenyl group in a way that aims to improve the binding rigidity and/or the water solubility of these dyes (Fig. 1). As we had a demonstrated earlier, we had a core structure of **OxN (4)** which already has many of the desired qualities for a fluorescent probe – good quantum yield, photostability even in prolonged studies, strong binding with DNA

[a] *University of Jyväskylä, Department of Chemistry, Nanoscience Centre, P.O. Box 35, Jyväskylä, FI-40014, Finland. E-mail: tanja.m.lahtinen@jyu.fi*
[b] *University of Jyväskylä, Department of Cell and Molecular Biology, Nanoscience Centre, Jyväskylä, FI-40014, Finland*

† Electronic supplementary information (ESI) available: Experimental details, detailed synthesis methods, product characterizations, comprehensive photophysical studies, including binding studies including dyes and dsDNA. CCDC 2294210 and 2294211. For ESI and crystallographic data in CIF or other electronic format see DOI: https://doi.org/10.1039/d3nj05400d

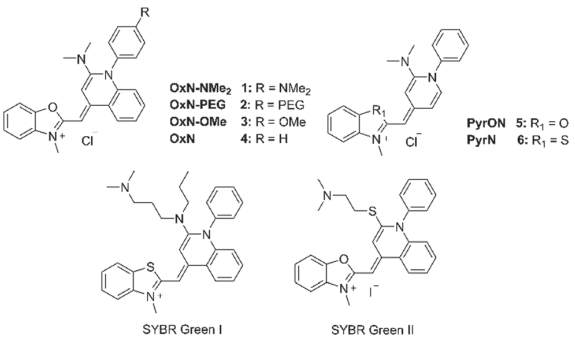

Fig. 1 Novel dyes **1–3** compared to previously published dyes **4–6**[16] and commercial dyes **SYBR Green I**[10,19] and **SYBR Green II**.[14,20]

and great turn-on fluorescence with low background emission. By further modifying this core we wanted to achieve two goals: increase the water solubility along with binding affinity and to gain more understanding how these structural modifications change the photophysical properties of the dyes.

Dimethylamine as a substituent was obvious choice since we had already seen that it improves the binding and brightness compared to thiol[15,16] and since it its capable of hydrogen bonding with the lone pair electrons, it could also improve the water solubility and at the same time enhance the binding affinity with the DNA. PEG group was included to for certain to see if the water solubility could be the answer to brighter and perhaps more user-friendly usage. Since **OxN-PEG** has the outreaching oxyethylene chain, we also wanted to include control of just methoxy group to see if the length of PEG chain affects the binding properties.

Dyes **1–3** were synthesized by using previously published methods.[14,15,24] The dye synthesis were done using the cyanine condensation method with quinoline salt and benzoxazolium salt as starting materials. In inert conditions, using triethylamine as a base catalyst, condensation is achieved in room temperature within four hours. Our synthesis also has additional substitution step to replace chloride in the quinoline moiety with dimethylamine. Purification is done with flash column chromatography, which are usually done at least twice to achieve desired purity. PEGylation of 4-iodophenol was done according to procedure by Nguyen *et. al.*[25] Detailed synthesis routes along with X-ray crystal structure parameters and geometry calculations can be found in ESI.†

Suitable crystal quality for single crystal X-ray diffraction (SCXRD) analysis were obtained from **1** and **3**. The crystal data and other experimental details for dyes **1** and **3** are given in the ESI.† As observed with the related dyes in our previous study,[16] the main molecular skeletons of **1** and **3** including benzoxazolium and quinoline moieties are planar in the solid state (Fig. S15 and S16, ESI†). The overall structures are also very similar to the quinoline containing dyes previously described by us.[16] The most notable deviation from the planarity of the entire molecules is observed with the phenyl ring bonded to quinoline nitrogen. The plane of the phenyl ring shows angles of 67.0° in **1** and of 71.6° (72.7°, 2nd molecule) in **3** to the plane of the dye skeleton. The high-level DFT [M06-2X, def2-TZVP with acetonitrile (dielectric = 37.50] as a solvent using C-PCM model) calculations match extremely well with the SCXRD geometry of **OxN-NMe$_2$ (1)**, **OxN-OMe (3)** and previously[16] studied dye **PyrON (5)** (Fig. S19, ESI†).

For absorption, emission, and excitation maxima (Fig. S22 and S23, ESI†), only few nanometre shifts between the dyes **1–3** are seen, essentially, all new dyes have similar maxima as the core dye **OxN (4)**. This is also observed with Stoke's shifts, the shifts only vary from 29 to 34 nm (Table 1). Previously, we had observed that even small, one heteroatom changes in the chromophore could change these maxima drastically in the nanometre scale.

Molar absorption coefficients (ε) were measured in three different solvents, ethanol, tris-EDTA (TE) buffer and 100 μM ct DNA in TE buffer solution. To investigate if the binding with DNA alters the absorption coefficient of the dyes, TE buffer was used as a reference for the final ctDNA solution. Ethanol was chosen as organic solvent to investigate the effect of solubility to the absorption coefficients. All dyes (**1–4**) have the highest absorption coefficients in ethanol (Table 1), following the trend previously observed.[15,16] Interestingly, **OxN-NMe$_2$ (1)** and **OxN-PEG (2)** have the lowest absorption coefficients in TE buffer. This could potentially indicate that without DNA in solution, dyes can for example aggregate, which is known quality of cyanine dyes,[26] lowering the absorption coefficients. While DNA offers favorable binding site where the dyes can fit, preventing the aggregation from happening and the dyes having higher absorption coefficients in ctDNA solution.

Table 1 Photophysical and binding parameters of the studied dyes. Full details of the measurements can be found in ESI

Dye	**OxN (4)**	**OxN-NMe$_2$ (1)**	**OxN-PEG (2)**	**OxN-OMe (3)**	**SYBR Green I**
λ_{abs} (nm)	464	462	463	463	497
ε_{max} (TE buffer) M^{-1} cm^{-1}	56 500 ± 800	52 500 ± 400	13 300 ± 200	51 000 ± 900	73 000[10]
ε_{max} (Ethanol) M^{-1} cm^{-1}	73 600 ± 600	93 000 ± 400	26 900 ± 150	77 900 ± 300	43 300
ε_{max} (100 μM ctDNA) M^{-1} cm^{-1}	47 300 ± 200	61 600 ± 1005	20 300 ± 200	49 800 ± 500	29 500
λ_{emi} (nm)	492	496	493	492	520
Stoke's shift (nm cm^{-1})	28/1230	34/1480	30/1310	29/1270	23/890
Φ	~1	0.014	~1	~1	0.8[19]
Brightness (M^{-1} cm^{-1})	**47 300**	**868**	**20 300**	**49 800**	**34 640**
K_a ($\times 10^6$ M^{-1})	8.5 ± 1.50	0.2 ± 0.02	57.9 ± 3.00	12.8 ± 1.10	5.9 ± 0.05
K_d (nM)	118	4100	17.3	78.1	167
n	3.4 ± 0.40	4.7 ± 0.30	6.0 ± 0.30	3.9 ± 0.09	3.2 ± 0.11
ΔG^0 (kJ mol^{-1})	−39.0	−27.7	−43.1	−41.2	−38.0

OxN-NMe$_2$ (1) and **OxN-OMe (3)** both had excellent absorption coefficients across all media, especially **OxN-NMe$_2$ (1)** having highest value of 93 000 M^{-1} cm^{-1} in ethanol. While **OxN-PEG (2)** did not excel with the absorption coefficients, including PEG arm did not completely shut down the absorption of the dye. Surprisingly, no clear evidence could be observed for the PEG increasing water solubility in UV-vis measurements.

Quantum yields of the dyes were determined with fluorescein standard (Fig. S25, ESI†) to gain more knowledge how the dyes perform when fully bound with ctDNA. Since all experiments so far gave consistent results between the dyes, same was expected for quantum yields. **OxN-PEG (2)** and **OxN-OMe (3)** do follow the trend, since the quantum yield was determined to be **1** for both dyes matching the quantum yield of **OxN (4)**. Surprisingly, the quantum yield of **OxN-NMe$_2$ (1)** was only 0.014 meaning that the additional amine group at the terminal phenyl group significantly quenched the fluorescence intensity of **OxN-NMe$_2$ (1)** when binding ctDNA. This result indicates that this additional electron donating group may alter the relaxation method of the dye after excitation.

Selected dyes (**1**, **3–6** and **SYBR Green I** and **II**) were also studied with RNA, to evaluate their performance compared to DNA. In this study, dye concentrations were kept at 0.05 μm in either DNA solution with concentration of 4.9 ng μl^{-1} or in RNA solution with concentration of 4.4 ng μl^{-1}, respectively. As we can see from Fig. 2, The new dye **OxN-OMe (3)** performs best with DNA, and almost as good as **OxN (4)** with RNA. Interestingly, the **OxN-NMe$_2$ (1)** performed very poorly with both DNA and RNA. **OxN-OMe (3)** and **OxN (4)** outperformed both commercial dyes, **SYBR Green I** and **II** as they have higher normalized emission values with DNA. **OxN (4)** and **OxN-OMe (3)** have slightly higher exaltation (ratio of intensity) with RNA than **SYBR Green II**, but the intensities are quite similar. **PyrON (5)** and **PyrN (6)** presented in our previous studies,[16] have significantly lower exaltation compared to the commercial dyes **SYBR Green I** and **II**, but a slight preference could be seen – **PyrON (5)** has higher exaltation with DNA and **PyrN (6)** with RNA, respectively. The only structural difference between these two is the change from oxazolium (**PyrON (5)**) to thiazolium moiety (**PyrN (6)**). Hence, with one heteroatom change from oxygen to sulfur, we can observe significant change in the photophysical qualities. When dyes have oxygen moiety, benzoxazolium, they seem to prefer DNA over RNA and when dyes have sulfur, benzothiazolium moiety in this study, they seem to prefer RNA. **SYBR Green II** also has the same thiazolium moiety as **PyrN (6)**, hinting that the sulfur might be a possible key element in synthesizing RNA selective dye. To support this theory Lu *et al.*[27] presented an RNA targeting dye with also thiazolium moiety combined with additional thiol substituent.

The binding properties of the dyes were evaluated using McGhee Von Hippel equation (Fig. S24, ESI†).[28] Due to the poor quantum yield of the **OxN-NMe$_2$ (1)**, it was also suspected to bind poorly with the ctDNA. This hypothesis was confirmed in our studies since the binding constant (K_a) was only 0.2 × 10^6 while previously synthesized **OxN (4)** has had the highest binding constant so far of 8.5 × 10^6, indicating that the **OxN-NMe$_2$ (1)** has relatively loose binding with the ctDNA compared to previously seen values. However, **OxN-OMe (3)** and especially **OxN-PEG (2)** shows even higher binding affinities than **OxN (4)** and **SYBR Green I**. **OxN-OMe (3)** has binding constant of 12.8 × 10^6 but **OxN-PEG (2)** is in other level compared to rest of the dyes; it has binding constant of 57.6 × 10^6. This result indicates that the oxygen rich functional sidechain enhances the binding, which could already be seen for the short methoxy chain in **OxN-OMe (3)**. Binding site sizes (n) for **OxN-NMe$_2$ (1)** and **OxN-OMe (3)** are in same level than to **OxN (4)** which has binding site size 3.4, **OxN-NMe$_2$ (1)** binding site size being 4.7 and **OxN-OMe (3)** 3.9, respectively. Both dyes having slightly larger binding sites due to the additional

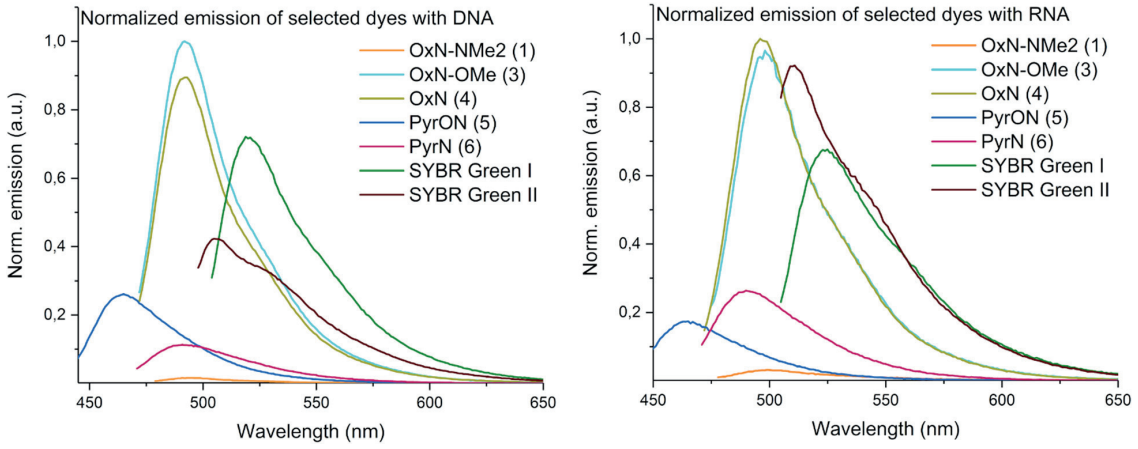

Fig. 2 Normalized emissions of studied dyes with DNA and RNA. The plots are normalized with the emission intensity of the highest emitting dye, **OxN-OMe** for DNA and **OxN** for RNA, to allow comparison of possible trends. For each measurement, dye concentrations were 0.05 μM. Nucleic acid solutions were prepared in TE buffer where DNA concentration was 4.9 ng μl^{-1} and RNA concentration was kept at 4.4 ng μl^{-1}, respectively.

functional groups in the terminal phenyl group. Similarly, **OxN-PEG (2)** has noticeably larger binding site size of 6.0 due to the longer side chain.

Finally, to have one number to compare the dyes, brightness was calculated for each dye by multiplying absorption coefficient in ctDNA solution with the determined quantum yield. This value estimates how many of the absorbed photons can eventually be emitted, hence giving a single value how well the dye can perform as fluorescent probe. Due to the low quantum yield, **OxN-NMe$_2$ (1)** has the lowest brightness of 868 M^{-1} cm^{-1} even though it had the highest absorption coefficient when bound with ctDNA. Great quantum yield and high absorption coefficient of **OxN-OMe (3)** makes it slightly brighter than **OxN (4)** and commercial dye **SYBR Green I** with brightness of 49 800 M^{-1} cm^{-1}. Similar methoxy group enhancement was also observed with indole-based copper probes[29] and tuning thiazole orange with electron donor and acceptor.[30] **OxN-PEG (2)** lands right in the middle, having great quantum yield, but the PEG group lowering the absorption coefficient even though it binds remarkably strongly with ctDNA.

To conclude, three new monomethine cyanine dyes with additional functional groups at the terminal phenyl group were synthesized and compared to the commercial dyes **SYBR Green I** and **II** and to selection of our previously published ones. Effect of different electron donating groups at terminal phenyl group to the photophysical properties were investigated. X-ray crystal structures were solved for **OxN-NMe$_2$ (1)** and **OxN-OMe (3)**. Methoxy (**OxN-OMe (3)**) increased the molar absorption coefficient and emission compared to the dye without any functional group at the same position (**OxN (4)**). However, including amine at this position (**OxN-NMe$_2$ (1)**), did increase the molar absorption coefficient of the dye, but it also quenched the emission intensity almost completely since the quantum yield dropped from 1 to only 0.014. Similarly, also the binding properties of **OxN-NMe$_2$ (1)** dropped significantly compared to other dyes. Interestingly, **OxN-PEG (2)** seems to bind extremely tightly with ctDNA compared to other studied dyes. The PEG substituent could provide additional binding interactions due to the oxygen lone pair electrons in the PEG chain which could interact with the DNA double helix, as observed by Howerton *et al.*[31]

In the end, we were able to design new and even better dye with excellent photophysical properties, **OxN-OMe (3)** exhibiting brightness of 49 800 M^{-1} cm^{-1}, quantum yield $\sim$1 and tight binding with ctDNA. Noting that **OxN-OMe (3)** is also significantly brighter than commercially available **SYBR Green I** with brightness 34 600 M^{-1} cm^{-1}. In this paper we also demonstrated that **OxN (4)** and **OxN-OMe (3)** are excellent choices to image viral RNA, even though they are not selective towards DNA or RNA, but they are more sensitive than the commercially available **SYBR Green II**, which prefers RNA. Additionally compared to other popular nucleic acid stains, ethidium bromide and YOYO-1, our dyes **OxN (4)** and **OxN-OMe (3)** exhibit higher quantum yields and brightness as well as better quantum yield than TOTO-1.[32] It is also noted that including sulphur to the dyes seemed to shift their preference from DNA towards RNA. We believe **OxN-OMe (3)** with additional electron donating group is excellent choice to image nucleic acids in future since it is very sensitive with both ctDNA and RNA. This researched also revealed extremely valuable information about how small changes of the functional groups outside the main chromophore can have drastic effects to the photophysical properties of the dyes.

Author contributions

Johanna Alaranta: writing – original draft, investigation, formal analysis, data curation. Arto Valkonen: data curation, writing – original draft, formal analysis. Sailee Shroff – data curation. Varpu Marjomäki – supervision, investigation. Kari Rissanen: supervision, data curation, formal analysis, writing – original draft. Tanja Lahtinen: writing – original draft, data curation, formal analysis, investigation, funding acquisition, project administration.

Conflicts of interest

There are no conflicts to declare.

Acknowledgements

Authors thank Dr Tatu Kumpulainen for his assistance with the spectroscopy studies. Kari Rissanen gratefully acknowledge the Academy of Finland (grant number: 351121).

Notes and references

1 F. Ponchel, C. Toomes, K. Bransfield, F. T. Leong, S. H. Douglas, S. L. Field, S. M. Bell, V. Combaret, A. Puisieux, A. J. Mighell, P. A. Robinson, C. F. Inglehearn, J. D. Isaacs and A. F. Markham, *BMC Biotechnol.*, 2003, **3**, DOI: 10.1186/1472-6750-3-18.
2 N. Marmiroli and E. Maestri, in *Food Toxicants Analysis*, Elsevier, 2007, ch. 6, pp. 147–187.
3 H. Cao and J. M. Shockey, *J. Agric. Food Chem.*, 2012, **60**, 12296–12303.
4 M. Bengtsson, H. J. Karlsson, G. Westman and M. Kubista, *Nucleic Acids Res.*, 2003, **31**, e45.
5 D. R. Marinowic, G. Zanirati, F. V. F. Rodrigues, M. V. C. Grahl, A. M. Alcará, D. C. Machado and J. C. Da Costa, *Sci. Rep.*, 2021, **11**, 2224.
6 J. S. Farrar and C. T. Wittwer, in *Molecular Diagnostics*, Elsevier, 2017, pp. 79–102.
7 K. M. Ririe, R. P. Rasmussen and C. T. Wittwer, *Anal. Biochem.*, 1997, **245**, 154–160.
8 H. Zipper, C. Buta, K. Lämmle, H. Brunner, J. Bernhagen and F. Vitzthum, *Nucleic Acids Res.*, 2004, **32**, e103.
9 A. E. Kiltie and A. J. Ryan, *Nucleic Acids Res.*, 1997, **25**, 2945–2946.
10 H. Zipper, H. Brunner, J. Bernhagen and F. Vitzthum, *Nucleic Acids Res.*, 2004, 32.

11 K. I. Kirsanov, E. A. Lesovaya, M. G. Yakubovskaya and G. A. Belitsky, *Mutat. Res., Genet. Toxicol. Environ. Mutagen.*, 2010, **699**, 1–4.
12 M. Laajala, K. Kalander, S. Consalvi, O. S. Amamuddy, Ö. T. Bishop, M. Biava, G. Poce and V. Marjomäki, *Pharmaceutics*, 2023, 15.
13 N. Pardi, M. J. Hogan, F. W. Porter and D. Weissman, *Nat. Rev. Drug Discovery*, 2018, **17**, 261–279.
14 V. K. Saarnio, K. Salorinne, V. P. Ruokolainen, J. R. Nilsson, T. R. Tero, S. Oikarinen, L. M. Wilhelmsson, T. M. Lahtinen and V. S. Marjomäki, *Dyes Pigm.*, 2020, **177**, 108282.
15 V. K. Saarnio, J. M. Alaranta and T. M. Lahtinen, *J. Mater. Chem. B*, 2021, **9**, 3484–3488.
16 J. M. Alaranta, K.-N. Truong, M. F. Matus, S. A. Malola, K. T. Rissanen, S. S. Shroff, V. S. Marjomäki, H. J. Häkkinen and T. M. Lahtinen, *Dyes Pigm.*, 2022, **208**, 110844.
17 A. I. Dragan, R. Pavlovic, J. B. McGivney, J. R. Casas-Finet, E. S. Bishop, R. J. Strouse, M. A. Schenerman and C. D. Geddes, *J. Fluoresc.*, 2012, **22**, 1189–1199.
18 A. I. Dragan, J. R. Casas-Finet, E. S. Bishop, R. J. Strouse, M. A. Schenerman and C. D. Geddes, *Biophys. J.*, 2010, **99**, 3010–3019.
19 Invitrogen. SYBR ® green I nucleic acid gel stain product information sheet, vols. 1–5, 2006.
20 SYBR® Green II RNA Gel Stain, Molecular Probes, 2001.
21 F. Deng and Z. Xu, *Chin. Chem. Lett.*, 2019, **30**, 1667–1681.
22 A. M. Grabarz, B. Jędrzejewska, A. Skotnicka, N. A. Murugan, F. Patalas, W. Bartkowiak, D. Jacquemin and B. Ośmiałowski, *Dyes Pigm.*, 2019, 170.
23 A. Kurutos, I. Balabanov, F. S. Kamounah, K. Nikolova-Ganeva, D. Borisova, N. Gadjev, T. Deligeorgiev and A. Tchorbanov, *Dyes Pigm.*, 2018, **157**, 267–277.
24 L. Ying, *US Pat.*, US20130137875A1, 2013.
25 R. Nguyen, N. Jouault, S. Zanirati, M. Rawiso, L. Allouche, G. Fuks, E. Buhler and N. Giuseppone, *Soft Matter*, 2014, **10**, 2926–2937.
26 G. S. Gopika, P. M. H. Prasad, A. G. Lekshmi, S. Lekshmypriya, S. Sreesaila, C. Arunima, M. S. Kumar, A. Anil, A. Sreekumar and Z. S. Pillai, *Mater. Today: Proc.*, 2020, **46**, 3102–3108.
27 Y. J. Lu, Q. Deng, D. P. Hu, Z. Y. Wang, B. H. Huang, Z. Y. Du, Y. X. Fang, W. L. Wong, K. Zhang and C. F. Chow, *Chem. Commun.*, 2015, **51**, 15241–15244.
28 J. D. McGhee and P. H. von Hippel, *J. Mol. Biol.*, 1974, **86**, 469–489.
29 X. Meng, L. Wang, Y. Zhai and H. Duan, *Res. Chem. Intermed.*, 2020, **46**, 5517–5533.
30 E. E. Rastede, M. Tanha, D. Yaron, S. C. Watkins, A. S. Waggoner and B. A. Armitage, *Photochem. Photobiol. Sci.*, 2015, **14**, 1703–1712.
31 S. B. Howerton, A. Nagpal and L. D. Williams, *Biopolymers*, 2003, **69**, 87–99.
32 Z. Zhang and S. Achilefu, *Org. Lett.*, 2004, **6**, 2067–2070.

DEPARTMENT OF CHEMISTRY, UNIVERSITY OF JYVÄSKYLÄ
RESEARCH REPORT SERIES

1. Vuolle, Mikko: Electron paramagnetic resonance and molecular orbital study of radical ions generated from (2.2)metacyclophane, pyrene and its hydrogenated compounds by alkali metal reduction and by thallium(III)trifluoroacetate oxidation. (99 pp.) 1976
2. Pasanen, Kaija: Electron paramagnetic resonance study of cation radical generated from various chlorinated biphenyls. (66 pp.) 1977
3. Carbon-13 Workshop, September 6-8, 1977. (91 pp.) 1977
4. Laihia, Katri: On the structure determination of norbornane polyols by NMR spectroscopy. (111 pp.) 1979
5. Nyrönen, Timo: On the EPR, ENDOR and visible absorption spectra of some nitrogen containing heterocyclic compounds in liquid ammonia. (76 pp.) 1978
6. Talvitie, Antti: Structure determination of some sesquiterpenoids by shift reagent NMR. (54 pp.) 1979
7. Häkli, Harri: Structure analysis and molecular dynamics of cyclic compounds by shift reagent NMR. (48 pp.) 1979
8. Pitkänen, Ilkka: Thermodynamics of complexation of 1,2,4-triazole with divalent manganese, cobalt, nickel, copper, zinc, cadmium and lead ions in aqueous sodium perchlorate solutions. (89 pp.) 1980
9. Asunta, Tuula: Preparation and characterization of new organometallic compounds synthesized by using metal vapours. (91 pp.) 1980
10. Sattar, Mohammad Abdus: Analyses of MCPA and its metabolites in soil. (57 pp.) 1980
11. Bibliography 1980. (31 pp.) 1981
12. Knuuttila, Pekka: X-Ray structural studies on some divalent 3d metal compounds of picolinic and isonicotinic acid N-oxides. (77 pp.) 1981
13. Bibliography 1981. (33 pp.) 1982
14. 6^{th} National NMR Symposium, September 9-10, 1982, Abstracts. (49 pp.) 1982
15. Bibliography 1982. (38 pp.) 1983
16. Knuuttila, Hilkka: X-Ray structural studies on some Cu(II), Co(II) and Ni(II) complexes with nicotinic and isonicotinic acid N-oxides. (54 pp.) 1983
17. Symposium on inorganic and analytical chemistry May 18, 1984, Program and Abstracts. (100 pp.) 1984
18. Knuutinen, Juha: On the synthesis, structure verification and gas chromatographic determination of chlorinated catechols and guaiacols occuring in spent bleach liquors of kraft pulp mill. (30 pp.) 1984
19. Bibliography 1983. (47 pp.) 1984
20. Pitkänen, Maija: Addition of BrCl, B_2 and Cl_2 to methyl esters of propenoic and 2-butenoic acid derivatives and ^{13}C NMR studies on methyl esters of saturated aliphatic mono- and dichlorocarboxylic acids. (56 pp.) 1985
21. Bibliography 1984. (39 pp.) 1985
22. Salo, Esa: EPR, ENDOR and TRIPLE spectroscopy of some nitrogen heteroaromatics in liquid ammonia. (111 pp.) 1985

23. Humppi, Tarmo: Synthesis, identification and analysis of dimeric impurities of chlorophenols. (39 pp.) 1985
24. Aho, Martti: The ion exchange and adsorption properties of sphagnum peat under acid conditions. (90 pp.) 1985
25. Bibliography 1985 (61 pp.) 1986
26. Bibliography 1986. (23 pp.) 1987
27. Bibliography 1987. (26 pp.) 1988
28. Paasivirta, Jaakko (Ed.): Structures of organic environmental chemicals. (67 pp.) 1988
29. Paasivirta, Jaakko (Ed.): Chemistry and ecology of organo-element compounds. (93 pp.) 1989
30. Sinkkonen, Seija: Determination of crude oil alkylated dibenzothiophenes in environment. (35 pp.) 1989
31. Kolehmainen, Erkki (Ed.): XII National NMR Symposium Program and Abstracts. (75 pp.) 1989
32. Kuokkanen, Tauno: Chlorocymenes and Chlorocymenenes: Persistent chlorocompounds in spent bleach liquors of kraft pulp mills. (40 pp.) 1989
33. Mäkelä, Reijo: ESR, ENDOR and TRIPLE resonance study on substituted 9,10-anthraquinone radicals in solution. (35 pp.) 1990
34. Veijanen, Anja: An integrated sensory and analytical method for identification of off-flavour compounds. (70 pp.) 1990
35. Kasa, Seppo: EPR, ENDOR and TRIPLE resonance and molecular orbital studies on a substitution reaction of anthracene induced by thallium(III) in two fluorinated carboxylic acids. (114 pp.) 1990
36. Herve, Sirpa: Mussel incubation method for monitoring organochlorine compounds in freshwater recipients of pulp and paper industry. (145 pp.) 1991
37. Pohjola, Pekka: The electron paramagnetic resonance method for characterization of Finnish peat types and iron (III) complexes in the process of peat decomposition. (77 pp.) 1991
38. Paasivirta, Jaakko (Ed.): Organochlorines from pulp mills and other sources. Research methodology studies 1988-91. (120 pp.) 1992
39. Veijanen, Anja (Ed.): VI National Symposium on Mass Spectrometry, May 13-15, 1992, Abstracts. (55 pp.) 1992
40. Rissanen, Kari (Ed.): The 7. National Symposium on Inorganic and Analytical Chemistry, May 22, 1992, Abstracts and Program. (153 pp.) 1992
41. Paasivirta, Jaakko (Ed.): CEOEC'92, Second Finnish-Russian Seminar: Chemistry and Ecology of Organo-Element Compounds. (93 pp.) 1992
42. Koistinen, Jaana: Persistent polychloroaromatic compounds in the environment: structure-specific analyses. (50 pp.) 1993
43. Virkki, Liisa: Structural characterization of chlorolignins by spectroscopic and liquid chromatographic methods and a comparison with humic substances. (62 pp.) 1993
44. Helenius, Vesa: Electronic and vibrational excitations in some

biologically relevant molecules. (30 pp.) 1993

45. Leppä-aho, Jaakko: Thermal behaviour, infrared spectra and x-ray structures of some new rare earth chromates(VI). (64 pp.) 1994
46. Kotila, Sirpa: Synthesis, structure and thermal behavior of solid copper(II) complexes of 2-amino-2- hydroxymethyl-1,3-propanediol. (111 pp.) 1994
47. Mikkonen, Anneli: Retention of molybdenum(VI), vanadium(V) and tungsten(VI) by kaolin and three Finnish mineral soils. (90 pp.) 1995
48. Suontamo, Reijo: Molecular orbital studies of small molecules containing sulfur and selenium. (42 pp.) 1995
49. Hämäläinen, Jouni: Effect of fuel composition on the conversion of fuel-N to nitrogen oxides in the combustion of small single particles. (50 pp.) 1995
50. Nevalainen, Tapio: Polychlorinated diphenyl ethers: synthesis, NMR spectroscopy, structural properties, and estimated toxicity. (76 pp.) 1995
51. Aittola, Jussi-Pekka: Organochloro compounds in the stack emission. (35 pp.) 1995
52. Harju, Timo: Ultrafast polar molecular photophysics of (dibenzylmethine)borondifluoride and 4-aminophthalimide in solution. (61 pp.) 1995
53. Maatela, Paula: Determination of organically bound chlorine in industrial and environmental samples. (83 pp.) 1995
54. Paasivirta, Jaakko (Ed.): CEOEC'95, Third Finnish-Russian Seminar: Chemistry and Ecology of Organo-Element Compounds. (109 pp.) 1995
55. Huuskonen, Juhani: Synthesis and structural studies of some supramolecular compounds. (54 pp.) 1995
56. Palm, Helena: Fate of chlorophenols and their derivatives in sawmill soil and pulp mill recipient environments. (52 pp.) 1995
57. Rantio, Tiina: Chlorohydrocarbons in pulp mill effluents and their fate in the environment. (89 pp.) 1997
58. Ratilainen, Jari: Covalent and non-covalent interactions in molecular recognition. (37 pp.) 1997
59. Kolehmainen, Erkki (Ed.): XIX National NMR Symposium, June 4-6, 1997, Abstracts. (89 pp.) 1997
60. Matilainen, Rose: Development of methods for fertilizer analysis by inductively coupled plasma atomic emission spectrometry. (41 pp.) 1997
61. Koistinen, Jari (Ed.): Spring Meeting on the Division of Synthetic Chemistry, May 15-16, 1997, Program and Abstracts. (36 pp.) 1997
62. Lappalainen, Kari: Monomeric and cyclic bile acid derivatives: syntheses, NMR spectroscopy and molecular recognition properties. (50 pp.) 1997
63. Laitinen, Eira: Molecular dynamics of cyanine dyes and phthalimides in solution: picosecond laser studies. (62 pp.) 1997
64. Eloranta, Jussi: Experimental and theoretical studies on some

quinone and quinol radicals. (40 pp.) 1997

65. Oksanen, Jari: Spectroscopic characterization of some monomeric and aggregated chlorophylls. (43 pp.) 1998
66. Häkkänen, Heikki: Development of a method based on laser-induced plasma spectrometry for rapid spatial analysis of material distributions in paper coatings. (60 pp.) 1998
67. Virtapohja, Janne: Fate of chelating agents used in the pulp and paper industries. (58 pp.) 1998
68. Airola, Karri: X-ray structural studies of supramolecular and organic compounds. (39 pp.) 1998
69. Hyötyläinen, Juha: Transport of lignin–type compounds in the receiving waters of pulp mills. (40 pp.) 1999
70. Ristolainen, Matti: Analysis of the organic material dissolved during totally chlorine-free bleaching. (40 pp.) 1999
71. Eklin, Tero: Development of analytical procedures with industrial samples for atomic emission and atomic absorption spectrometry. (43 pp.) 1999
72. Välisaari, Jouni: Hygiene properties of resol-type phenolic resin laminates. (129 pp.) 1999
73. Hu, Jiwei: Persistent polyhalogenated diphenyl ethers: model compounds syntheses, characterization and molecular orbital studies. (59 pp.) 1999
74. Malkavaara, Petteri: Chemometric adaptations in wood processing chemistry. (56 pp.) 2000
75. Kujala Elena, Laihia Katri, Nieminen Kari (Eds.): NBC 2000, Symposium on Nuclear, Biological and Chemical Threats in the 21st Century. (299 pp.) 2000
76. Rantalainen, Anna-Lea: Semipermeable membrane devices in monitoring persistent organic pollutants in the environment. (58 pp.) 2000
77. Lahtinen, Manu: *In situ* X-ray powder diffraction studies of Pt/C, CuCl/C and Cu_2O/C catalysts at elevated temperatures in various reaction conditions. (92 pp.) 2000
78. Tamminen, Jari: Syntheses, empirical and theoretical characterization, and metal cation complexation of bile acid-based monomers and open/closed dimers. (54 pp.) 2000
79. Vatanen, Virpi: Experimental studies by EPR and theoretical studies by DFT calculations of α-amino-9,10-anthraquinone radical anions and cations in solution. (37 pp.) 2000
80. Kotilainen, Risto: Chemical changes in wood during heating at 150-260 °C. (57 pp.) 2000
81. Nissinen, Maija: X-ray structural studies on weak, non-covalent interactions in supramolecular compounds. (69 pp.) 2001
82. Wegelius, Elina: X-ray structural studies on self-assembled hydrogen-bonded networks and metallosupramolecular complexes. (84 pp.) 2001
83. Paasivirta, Jaakko (Ed.): CEOEC'2001, Fifth Finnish-Russian Seminar: Chemistry and Ecology of Organo-Element Compounds. (163 pp.) 2001
84. Kiljunen, Toni: Theoretical studies on spectroscopy and

atomic dynamics in rare gas solids. (56 pp.) 2001

85. Du, Jin: Derivatives of dextran: synthesis and applications in oncology. (48 pp.) 2001
86. Koivisto, Jari: Structural analysis of selected polychlorinated persistent organic pollutants (POPs) and related compounds. (88 pp.) 2001
87. Feng, Zhinan: Alkaline pulping of non-wood feedstocks and characterization of black liquors. (54 pp.) 2001
88. Halonen, Markku: Lahon havupuun käyttö sulfaattiprosessin raaka-aineena sekä havupuun lahontorjunta. (90 pp.) 2002
89. Falábu, Dezsö: Synthesis, conformational analysis and complexation studies of resorcarene derivatives. (212 pp.) 2001
90. Lehtovuori, Pekka: EMR spectroscopic studies on radicals of ubiquinones Q-*n*, vitamin K_3 and vitamine E in liquid solution. (40 pp.) 2002
91. Perkkalainen, Paula: Polymorphism of sugar alcohols and effect of grinding on thermal behavior on binary sugar alcohol mixtures. (53 pp.) 2002
92. Ihalainen, Janne: Spectroscopic studies on light-harvesting complexes of green plants and purple bacteria. (42 pp.) 2002
93. Kunttu, Henrik, Kiljunen, Toni (Eds.): 4th International Conference on Low Temperature Chemistry. (159 pp.) 2002
94. Väisänen, Ari: Development of methods for toxic element analysis in samples with environmental concern by ICP-AES and ETAAS. (54 pp.) 2002
95. Luostarinen, Minna: Synthesis and characterisation of novel resorcarene derivatives. (200 pp.) 2002
96. Louhelainen, Jarmo: Changes in the chemical composition and physical properties of wood and nonwood black liquors during heating. (68 pp.) 2003
97. Lahtinen, Tanja: Concave hydrocarbon cyclophane π-prismands. (65 pp.) 2003
98. Laihia, Katri (Ed.): NBC 2003, Symposium on Nuclear, Biological and Chemical Threats – A Crisis Management Challenge. (245 pp.) 2003
99. Oasmaa, Anja: Fuel oil quality properties of wood-based pyrolysis liquids. (32 pp.) 2003
100. Virtanen, Elina: Syntheses, structural characterisation, and cation/anion recognition properties of nano-sized bile acid-based host molecules and their precursors. (123 pp.) 2003
101. Nättinen, Kalle: Synthesis and X-ray structural studies of organic and metallo-organic supramolecular systems. (79 pp.) 2003
102. Lampiselkä, Jarkko: Demonstraatio lukion kemian opetuksessa. (285 pp.) 2003
103. Kallioinen, Jani: Photoinduced dynamics of $Ru(dcbpy)_2(NCS)_2$ – in solution and on nanocrystalline titanium dioxide thin films. (47 pp.) 2004
104. Valkonen, Arto (Ed.): VII Synthetic Chemistry Meeting and XXVI Finnish NMR Symposium. (103 pp.) 2004

105. Vaskonen, Kari: Spectroscopic studies on atoms and small molecules isolated in low temperature rare gas matrices. (65 pp.) 2004
106. Lehtovuori, Viivi: Ultrafast light induced dissociation of $Ru(dcbpy)(CO)_2I_2$ in solution. (49 pp.) 2004
107. Saarenketo, Pauli: Structural studies of metal complexing Schiff bases, Schiff base derived *N*-glycosides and cyclophane π-prismands. (95 pp.) 2004
108. Paasivirta, Jaakko (Ed.): CEOEC'2004, Sixth Finnish-Russian Seminar: Chemistry and Ecology of Organo-Element Compounds. (147 pp.) 2004
109. Suontamo, Tuula: Development of a test method for evaluating the cleaning efficiency of hard-surface cleaning agents. (96 pp.) 2004
110. Güneş, Minna: Studies of thiocyanates of silver for nonlinear optics. (48 pp.) 2004
111. Ropponen, Jarmo: Aliphatic polyester dendrimers and dendrons. (81 pp.) 2004
112. Vu, Mân Thi Hong: Alkaline pulping and the subsequent elemental chlorine-free bleaching of bamboo (*Bambusa procera*). (69 pp.) 2004
113. Mansikkamäki, Heidi: Self-assembly of resorcinarenes. (77 pp.) 2006
114. Tuononen, Heikki M.: EPR spectroscopic and quantum chemical studies of some inorganic main group radicals. (79 pp.) 2005
115. Kaski, Saara: Development of methods and applications of laser-induced plasma spectroscopy in vacuum ultraviolet. (44 pp.) 2005
116. Mäkinen, Riika-Mari: Synthesis, crystal structure and thermal decomposition of certain metal thiocyanates and organic thiocyanates. (119 pp.) 2006
117. Ahokas, Jussi: Spectroscopic studies of atoms and small molecules isolated in rare gas solids: photodissociation and thermal reactions. (53 pp.) 2006
118. Busi, Sara: Synthesis, characterization and thermal properties of new quaternary ammonium compounds: new materials for electrolytes, ionic liquids and complexation studies. (102 pp.) 2006
119. Mäntykoski, Keijo: PCBs in processes, products and environment of paper mills using wastepaper as their raw material. (73 pp.) 2006
120. Laamanen, Pirkko-Leena: Simultaneous determination of industrially and environmentally relevant aminopolycarboxylic and hydroxycarboxylic acids by capillary zone electrophoresis. (54 pp.) 2007
121. Salmela, Maria: Description of oxygen-alkali delignification of kraft pulp using analysis of dissolved material. (71 pp.) 2007
122. Lehtovaara, Lauri: Theoretical studies of atomic scale impurities in superfluid ^{4}He. (87 pp.) 2007
123. Rautiainen, J. Mikko: Quantum chemical calculations of structures, bonding, and spectroscopic properties of some sulphur and selenium iodine cations. (71 pp.) 2007
124. Nummelin, Sami: Synthesis, characterization, structural and

retrostructural analysis of self-assembling pore forming dendrimers. (286 pp.) 2008

125. Sopo, Harri: Uranyl(VI) ion complexes of some organic aminobisphenolate ligands: syntheses, structures and extraction studies. (57 pp.) 2008
126. Valkonen, Arto: Structural characteristics and properties of substituted cholanoates and *N*-substituted cholanamides. (80 pp.) 2008
127. Lähde, Anna: Production and surface modification of pharmaceutical nano- and microparticles with the aerosol flow reactor. (43 pp.) 2008
128. Beyeh, Ngong Kodiah: Resorcinarenes and their derivatives: synthesis, characterization and complexation in gas phase and in solution. (75 pp.) 2008
129. Välisaari, Jouni, Lundell, Jan (Eds.): Kemian opetuksen päivät 2008: uusia oppimisympäristöjä ja ongelmalähtöistä opetusta. (118 pp.) 2008
130. Myllyperkiö, Pasi: Ultrafast electron transfer from potential organic and metal containing solar cell sensitizers. (69 pp.) 2009
131. Käkölä, Jaana: Fast chromatographic methods for determining aliphatic carboxylic acids in black liquors. (82 pp.) 2009
132. Koivukorpi, Juha: Bile acid-arene conjugates: from photoswitchability to cancer cell detection. (67 pp.) 2009
133. Tuuttila, Tero: Functional dendritic polyester compounds: synthesis and characterization of small bifunctional dendrimers and dyes. (74 pp.) 2009
134. Salorinne, Kirsi: Tetramethoxy resorcinarene based cation and anion receptors: synthesis, characterization and binding properties. (79 pp.) 2009
135. Rautiainen, Riikka: The use of first-thinning Scots pine (*Pinus sylvestris*) as fiber raw material for the kraft pulp and paper industry. (73 pp.) 2010
136. Ilander, Laura: Uranyl salophens: synthesis and use as ditopic receptors. (199 pp.) 2010
137. Kiviniemi, Tiina: Vibrational dynamics of iodine molecule and its complexes in solid krypton - Towards coherent control of bimolecular reactions? (73 pp.) 2010
138. Ikonen, Satu: Synthesis, characterization and structural properties of various covalent and non-covalent bile acid derivatives of N/O-heterocycles and their precursors. (105 pp.) 2010
139. Siitonen, Anni: Spectroscopic studies of semiconducting single-walled carbon nanotubes. (56 pp.) 2010
140. Raatikainen, Kari: Synthesis and structural studies of piperazine cyclophanes – Supramolecular systems through Halogen and Hydrogen bonding and metal ion coordination. (69 pp.) 2010
141. Leivo, Kimmo: Gelation and gel properties of two- and three-component Pyrene based low molecular weight organogelators. (116 pp.) 2011
142. Martiskainen, Jari: Electronic energy transfer in light-harvesting complexes isolated from *Spinacia oleracea* and from three

photosynthetic green bacteria *Chloroflexus aurantiacus*, *Chlorobium tepidum*, and *Prosthecochloris aestuarii*. (55 pp.) 2011

143. Wichmann, Oula: Syntheses, characterization and structural properties of [O,N,O,X´] aminobisphenolate metal complexes. (101 pp.) 2011
144. Ilander, Aki: Development of ultrasound-assisted digestion methods for the determination of toxic element concentrations in ash samples by ICP-OES. (58 pp.) 2011
145. The Combined XII Spring Meeting of the Division of Synthetic Chemistry and XXXIII Finnish NMR Symposium. Book of Abstracts. (90 pp.) 2011
146. Valto, Piia: Development of fast analysis methods for extractives in papermaking process waters. (73 pp.) 2011
147. Andersin, Jenni: Catalytic activity of palladium-based nanostructures in the conversion of simple olefinic hydro- and chlorohydrocarbons from first principles. (78 pp.) 2011
148. Aumanen, Jukka: Photophysical properties of dansylated poly(propylene amine) dendrimers. (55 pp.) 2011
149. Kärnä, Minna: Ether-functionalized quaternary ammonium ionic liquids – synthesis, characterization and physicochemical properties. (76 pp.) 2011
150. Jurček, Ondřej: Steroid conjugates for applications in pharmacology and biology. (57 pp.) 2011
151. Nauha, Elisa: Crystalline forms of selected Agrochemical actives: design and synthesis of cocrystals. (77 pp.) 2012
152. Ahkola, Heidi: Passive sampling in monitoring of nonylphenol ethoxylates and nonylphenol in aquatic environments. (92 pp.) 2012
153. Helttunen, Kaisa: Exploring the self-assembly of resorcinarenes: from molecular level interactions to mesoscopic structures. (78 pp.) 2012
154. Linnanto, Juha: Light excitation transfer in photosynthesis revealed by quantum chemical calculations and exiton theory. (179 pp.) 2012
155. Roiko-Jokela, Veikko: Digital imaging and infrared measurements of soil adhesion and cleanability of semihard and hard surfaces. (122 pp.) 2012
156. Noponen, Virpi: Amides of bile acids and biologically important small molecules: properties and applications. (85 pp.) 2012
157. Hulkko, Eero: Spectroscopic signatures as a probe of structure and dynamics in condensed-phase systems – studies of iodine and gold ranging from isolated molecules to nanoclusters. (69 pp.) 2012
158. Lappi, Hanna: Production of Hydrocarbon-rich biofuels from extractives-derived materials. (95 pp.) 2012
159. Nykänen, Lauri: Computational studies of Carbon chemistry on transition metal surfaces. (76 pp.) 2012
160. Ahonen, Kari: Solid state studies of pharmaceutically important molecules and their derivatives. (65 pp.) 2012

161. Pakkanen, Hannu: Characterization of organic material dissolved during alkaline pulping of wood and non-wood feedstocks. (76 pp.) 2012
162. Moilanen, Jani: Theoretical and experimental studies of some main group compounds: from closed shell interactions to singlet diradicals and stable radicals. (80 pp.) 2012
163. Himanen, Jatta: Stereoselective synthesis of Oligosaccharides by *De Novo* Saccharide welding. (133 pp.) 2012
164. Bunzen, Hana: Steroidal derivatives of nitrogen containing compounds as potential gelators. (76 pp.) 2013
165. Seppälä, Petri: Structural diversity of copper(II) amino alcohol complexes. Syntheses, structural and magnetic properties of bidentate amino alcohol copper(II) complexes. (67 pp.) 2013
166. Lindgren, Johan: Computational investigations on rotational and vibrational spectroscopies of some diatomics in solid environment. (77 pp.) 2013
167. Giri, Chandan: Sub-component self-assembly of linear and non-linear diamines and diacylhydrazines, formulpyridine and transition metal cations. (145 pp.) 2013
168. Riisiö, Antti: Synthesis, Characterization and Properties of Cu(II)-, Mo(VI)- and U(VI) Complexes With Diaminotetraphenolate Ligands. (51 pp.) 2013
169. Kiljunen, Toni (Ed.): Chemistry and Physics at Low Temperatures. Book of Abstracts. (103 pp.) 2013
170. Hänninen, Mikko: Experimental and Computational Studies of Transition Metal Complexes with Polydentate Amino- and Aminophenolate Ligands: Synthesis, Structure, Reactivity and Magnetic Properties. (66 pp.) 2013
171. Antila, Liisa: Spectroscopic studies of electron transfer reactions at the photoactive electrode of dye-sensitized solar cells. (53 pp.) 2013
172. Kemppainen, Eeva: Mukaiyama-Michael reactions with α-substituted acroleins – a useful tool for the synthesis of the pectenotoxins and other natural product targets. (190 pp.) 2013
173. Virtanen, Suvi: Structural Studies of Dielectric Polymer Nanocomposites. (49 pp.) 2013
174. Yliniemelä-Sipari, Sanna: Understanding The Structural Requirements for Optimal Hydrogen Bond Catalyzed Enolization – A Biomimetic Approach.(160 pp.) 2013
175. Leskinen, Mikko V: Remote β-functionalization of β'-keto esters. (105 pp.) 2014
176. 12th European Conference on Research in Chemistry Education (ECRICE2014). Book of Abstracts. (166 pp.) 2014
177. Peuronen, Anssi: N-Monoalkylated DABCO-Based N-Donors as Versatile Building Blocks in Crystal Engineering and Supramolecular Chemistry. (54 pp.) 2014
178. Perämäki, Siiri: Method development for determination and recovery of rare earth elements from industrial fly ash. (88 pp.) 2014

179. Chernyshev, Alexander, N.: Nitrogen-containing ligands and their platinum(IV) and gold(III) complexes: investigation and basicity and nucleophilicity, luminescence, and aurophilic interactions. (64 pp.) 2014
180. Lehto, Joni: Advanced Biorefinery Concepts Integrated to Chemical Pulping. (142 pp.) 2015
181. Tero, Tiia-Riikka: Tetramethoxy resorcinarenes as platforms for fluorescent and halogen bonding systems. (61 pp.) 2015
182. Löfman, Miika: Bile acid amides as components of microcrystalline organogels. (62 pp.) 2015
183. Selin, Jukka: Adsorption of softwood-derived organic material onto various fillers during papermaking. (169 pp.) 2015
184. Piisola, Antti: Challenges in the stereoselective synthesis of allylic alcohols. (210 pp.) 2015
185. Bonakdarzadeh, Pia: Supramolecular coordination polyhedra based on achiral and chiral pyridyl ligands: design, preparation, and characterization. (65 pp.) 2015
186. Vasko, Petra: Synthesis, characterization, and reactivity of heavier group 13 and 14 metallylenes and metalloid clusters: small molecule activation and more. (66 pp.) 2015
187. Topić, Filip: Structural Studies of Nano-sized Supramolecular Assemblies. (79 pp.) 2015
188. Mustalahti, Satu: Photodynamics Studies of Ligand-Protected Gold Nanoclusters by using Ultrafast Transient Infrared Spectroscopy. (58 pp.) 2015
189. Koivisto, Jaakko: Electronic and vibrational spectroscopic studies of gold-nanoclusters. (63 pp.) 2015
190. Suhonen, Aku: Solid state conformational behavior and interactions of series of aromatis oligoamide foldamers. (68 pp.) 2016
191. Soikkeli, Ville: Hydrometallurgical recovery and leaching studies for selected valuable metals from fly ash samples by ultrasound-assisted extraction followed by ICP-OES determination. (107 pp.) 2016
192. XXXVIII Finnish NMR Symposium. Book of Abstracts. (51 pp.) 2016
193. Mäkelä, Toni: Ion Pair Recognition by Ditopic Crown Ether Based bis-Urea and Uranyl Salophen Receptors. (75 pp.) 2016
194. Lindholm-Lehto, Petra: Occurrence of pharmaceuticals in municipal wastewater treatment plants and receiving surface waters in Central and Southern Finland. (98 pp.) 2016
195. Härkönen, Ville: Computational and Theoretical studies on Lattice Thermal conductivity and Thermal properties of Silicon Clathrates. (89 pp.) 2016
196. Tuokko, Sakari: Understanding selective reduction reactions with heterogeneous Pd and Pt: climbing out of the black box. (85 pp.) 2016
197. Nuora, Piia: Monitapaustutkimus LUMA-Toimintaan liittyvissä oppimisympäristöissä tapahtuvista kemian oppimiskokemuksista. (171 pp.) 2016

198. Kumar, Hemanathan: Novel Concepts on The Recovery of By-Products from Alkaline Pulping. (61 pp.) 2016
199. Arnedo-Sánchez, Leticia: Lanthanide and Transition Metal Complexes as Building Blocks for Supramolecular Functional Materials. (227 pp.) 2016
200. Gell, Lars: Theoretical Investigations of Ligand Protected Silver Nanoclusters. (134 pp.) 2016
201. Vaskuri, Juhani: Oppiennätyksistä opetussuunnitelman perusteisiin - lukion kemian kansallisen opetussuunnitelman kehittyminen Suomessa vuosina 1918-2016. (314 pp.) 2017
202. Lundell Jan, Kiljunen Toni (Eds.): 22nd Horizons in Hydrogen Bond Research. Book of Abstracts. 2017
203. Turunen, Lotta: Design and construction of halogen-bonded capsules and cages. (61 pp.) 2017
204. Hurmalainen, Juha: Experimental and computational studies of unconventional main group compounds: stable radicals and reactive intermediates. (88 pp.) 2017
205. Koivistoinen Juha: Non-linear interactions of femtosecond laser pulses with graphene: photo-oxidation, imaging and photodynamics. (68 pp.) 2017
206. Chen, Chengcong: Combustion behavior of black liquors: droplet swelling and influence of liquor composition. (39 pp.) 2017
207. Mansikkamäki, Akseli: Theoretical and Computational Studies of Magnetic Anisotropy and Exchange Coupling in Molecular Systems. (190 p. + included articles) 2018.
208. Tatikonda, Rajendhraprasad: Multivalent N-donor ligands for the construction of coordination polymers and coordination polymer gels. (62 pp.) 2018
209. Budhathoki, Roshan: Beneficiation, desilication and selective precipitation techniques for phosphorus refining from biomass derived fly ash. (64 pp.) 2018
210. Siitonen, Juha: Synthetic Studies on 1-azabicyclo[5.3.0]decane Alkaloids. (140 pp.) 2018
211. Ullah, Saleem: Advanced Biorefinery Concepts Related to Non-wood Feedstocks. (57 pp.) 2018
212. Ghalibaf, Maryam: Analytical Pyrolysis of Wood and Non-Wood Materials from Integrated Biorefinery Concepts. (106 pp.) 2018

DEPARTMENT OF CHEMISTRY, UNIVERSITY OF JYVÄSKYLÄ
DISSERTATIONS PUBLISHED IN THE JYU DISSERTATIONS RESEARCH SERIES

1. Bulatov, Evgeny: Synthetic and structural studies of covalent and non-covalent interactions of ligands and metal center in platinum(II) complexes containing 2,2′-dipyridylamine or oxime ligands. (58 pp.) 2019. JYU Dissertations 70.
2. Annala, Riia: Conformational Properties and Anion Complexes of Aromatic Oligoamide Foldamers. (80 pp.) 2019. JYU Dissertations 84.
3. Isoaho, Jukka Pekka: Dithionite Bleaching of Thermomechanical Pulp - Chemistry and Optimal Conditions. (73 pp.) 2019. JYU Dissertations 85.
4. Nygrén, Enni: Recovery of rubidium from power plant fly ash. (98 pp.) 2019. JYU Dissertations 136.
5. Kiesilä, Anniina: Supramolecular chemistry of anion-binding receptors based on concave macromolecules. (68 pp.) 2019. JYU Dissertations 137.
6. Sokolowska, Karolina: Study of water-soluble p-MBA-protected gold nanoclusters and their superstructures. (60 pp.) 2019. JYU Dissertations 167.
7. Lahtinen, Elmeri: Chemically Functional 3D Printing: Selective Laser Sintering of Customizable Metal Scavengers. (71 pp.) 2019. JYU Dissertations 175.
8. Larijani, Amir: Oxidative reactions of cellulose under alkaline conditions. (102 pp.) 2020. JYU Dissertations 217.
9. Kolari, Kalle: Metal-metal contacts in late transition metal polymers. (60 pp.) 2020. JYU Dissertations 220.
10. Kauppinen, Minttu: Multiscale computational investigation of catalytic properties of zirconia supported noble metals. (87 pp.) 2020. JYU Dissertations 231.
11. Ding, Xin: Halogen Bond in Crystal Engineering: Structural Studies on Crystals with Ruthenium Centered Complexes and 1-(4-Pyridyl)-4-thiopyridine Zwitterion as Halogen Bond Acceptors. (59 pp.) 2020. JYU Dissertations 323.
12. Neuvonen, Antti: Toward an Understanding of Hydrogen-Bonding Bifunctional Organocatalyst Conformations and Their Activity in Asymmetric Mannich Reactions. (77 pp.) 2020. JYU Dissertations 336.
13. Kortet, Sami: 2,5-Diarylpyrrolidines and Pyroglutamic-Acid-Derived 2-Diarylmethyl-5-Aryl-Pyrrolidines: Their Synthesis and Use in Asymmetric Synthesis. (221 pp.) 2020. JYU Dissertations 337.
14. Saarnio, Ville: Fluorescent probes, noble metal nanoparticles and their nanocomposites: detection of nucleic acids and other biological targets. (80 pp.) 2021. JYU Dissertations 361.
15. Chernysheva, Maria: σ-hole interactions: the effect of the donors and acceptors nature in selenoureas, thioureas, halogenated species, substituted benzenes, and their adducts. (72 pp.) 2021. JYU Dissertations 370.
16. Bulatova, Margarita: Noncovalent interactions as a tool for supramolecular self-assembly of metallopolymers. (62 pp.) 2021. JYU Dissertations 377.

17. Romppanen, Sari: Laser-spectroscopic studies of rare earth element- and lithium-bearing minerals and rocks. (66 pp.) 2021. JYU Dissertations 393.
18. Kukkonen, Esa: Nonlinear optical materials through weak interactions and their application in 3D printing. (58 pp.) 2021. JYU Dissertations 441.
19. Kuosmanen, Riikka: The Effect of Structure on the Gel Formation Ability and the Properties of Bile Acid Based Supramolecular Organogels. (68 pp.) 2021. JYU Dissertations 465.
20. Reuna, Sini: Development of a Method for Phosphorus Recovery from Wastewaters. (67 pp.) 2022. JYU Dissertations 486.
21. Taipale, Essi: Synthetic and Structural Studies on the Effect of Non-Covalent Interactions on N(*sp2*)-Heterocyclic Molecules. (67 pp.) 2022. JYU Dissertations 496.
22. Järvinen, Teemu: Molecular Dynamics View on Matrix Isolation. (143 pp.) 2022. JYU Dissertations 544.
23. Kumar, Parveen: Synthesis and Structural Studies on Halogen(I) Complexes. (160 pp.) 2022. JYU Dissertations 549.
24. Forsblom, Samu: Design and Construction of Metal-Organic Polyhedra. (212 pp.) 2022. JYU Dissertations 569.
25. Korpelin, Ville: Computational Studies of Catalytic Active Site Properties and Reactions at the Metal–Oxide Interface. (78 pp.) 2022. JYU Dissertations 578.
26. Vuori, Hannu: Extending Benson Group Increment Theory to Compounds of Phosphorus, Silicon, and Boron with Computational Chemistry. (59 pp.) 2022. JYU Dissertations 581.
27. Pallerla, Rajanish: Studies Towards Synthesis of Favipiravir & Humilisin E. (139 pp.) 2023. JYU Dissertations 611.
28. Taponen, Anni: Radical-Ion Salts based on Thiazyls and Tetracyanoquinodimethane: Hysteretic Magnetic Bistability in a Multicomponent System. (66 pp.) 2023. JYU Dissertations 613.
29. Aho, Noora: Molecular Dynamics Simulations of Acids and Bases in Biomolecular Environments. (78 pp.) 2023. JYU Dissertations 614.
30. Sabooni Asre Hazer, Maryam: Electronic and Optical Properties of Gold Clusters with Carbene Ligands using Density Functional Theory Calculations. (68 pp.) 2023. JYU Dissertations 650.
31. Kinnunen, Virva-Tuuli: Improving the Accuracy of Single Particle ICP-MS Analyses of Au and Ag Nanoparticles. (67 pp.) 2023. JYU Dissertations 689.
32. Kulomäki, Suvi: Preconcentration, Speciation, and Determination of Mercury in Natural Waters by Inductively Coupled Plasma Mass Spectrometry. (61 pp.) 2023. JYU Dissertations 725.
33. Schirmer, Johanna: Effects of Two-Photon Oxidation for the Development of Graphene-Bio Interfaces. (69 pp.) 2023. JYU Dissertations 726.
34. Halmemies, Eelis: Chemical Changes in the Industrial Extractive-Containing Sidestreams of Norway Spruce (*Picea abies*) during Storage. (84 pp.) 2024. JYU Dissertations 737.